NAVAL POSTGRADUATE SCHOOL
Monterey, California

THESIS

FINITE ELEMENT MODELING AND SIMULATION OF THERMOMECHANICAL PROCESSING OF PARTICLE REINFORCED METAL MATRIX COMPOSITES

by
Kendall Gennick

March, 1997

Thesis Advisor:	Young W. Kwon
Second Reader:	Terry R. McNelley

Approved for public release; distribution is unlimited.

REPORT DOCUMENTATION PAGE

Form Approved
OMB No. 0704-0188

1. AGENCY USE ONLY *(Leave blank)*	**2. REPORT DATE** March 1997	**3. REPORT TYPE AND DATES COVERED** Master's Thesis

4. TITLE AND SUBTITLE
FINITE ELEMENT MODELING AND SIMULATION OF THERMOMECHANICAL PROCESSING OF PARTICLE REINFORCED MMC'S

5. FUNDING NUMBERS

6. AUTHOR(S)
Gennick, Kendall

7. PERFORMING ORGANIZATION NAME(S) AND ADDRESS(ES)
Naval Postgraduate School
Monterey, CA 93943-5000

8. PERFORMING ORGANIZATION REPORT NUMBER

9. SPONSORING / MONITORING AGENCY NAME(S) AND ADDRESS(ES)
U.S. Army Research Lab/Army Research Office
P.O. Box 12211
Reasearch Triangle Park, NC 27709-2211
Attn: Dr. Wilbur Simmons

10. SPONSORING / MONITORING AGENCY REPORT NUMBER

11. SUPPLEMENTARY NOTES
The views expressed in this thesis are those of the author and do not reflect the official policy or position of the Department of Defense or the U.S. Government.

12a. DISTRIBUTION / AVAILABILITY STATEMENT
Approved for public release; distribution unlimited.

12b. DISTRIBUTION CODE

ABSTRACT *(maximum 200 words)*

During the consolidation phase, reinforcement particles of Metal Matrix Composites (MMC's) tend to be non uniformly distributed. The result is that the material properties of the composite materials are not as good as those originally desired. Through large amounts of straining, homogeneity can be achieved. Finite element models of MMC's undergoing different thermomechanical processes (TMP's) to true strains of approximately 1.2 were generated. The models consist of particle clusters within the particle-depleted matrix. The particle clusters were modeled by either a smeared model in which the particles refine the grains in the cluster, or a discrete model of the particles within clusters. The smeared and discrete models qualitatively agreed with each other. The results suggest that the best TMP to reach a state of reinforcement particle homogeneity was a hot worked, low strain rate TMP.

14. SUBJECT TERMS
Metal Matrix Composites, Particle Reinforcement, Thermomechanical Processing, Finite Element Modeling, Particle Homogenization.

15. NUMBER OF PAGES
144

16. PRICE CODE

17. SECURITY CLASSIFICATION OF REPORT Unclassified	**18. SECURITY CLASSIFICATION OF THIS PAGE** Unclassified	**19. SECURITY CLASSIFI- CATION OF ABSTRACT** Unclassified	**20. LIMITATION OF ABSTRACT** UL

NSN 7540-01-280-5500

Standard Form 298 (Rev. 2-89)
Prescribed by ANSI Std. 239-18

FINITE ELEMENT MODELING AND SIMULATION OF THERMOMECHANICAL PROCESSING OF PARTICLE REINFORCED METAL MATRIX COMPOSITES

Kendall Gennick
Lieutenant, United States Navy
B.S., Auburn University, 1989

Submitted in partial fulfillment of the
requirements for the degree of

MASTER OF SCIENCE IN MECHANICAL ENGINEERING

from the

NAVAL POSTGRADUATE SCHOOL
March 1997

ABSTRACT

During the consolidation phase, reinforcement particles of Metal Matrix Composites (MMC's) tend to be non uniformly distributed. The result is that the material properties of the composite materials are not as good as those originally desired. Through large amounts of straining, homogeneity can be achieved. Finite element models of MMC's undergoing different thermomechanical processes (TMP's) to true strains of approximately 1.2 were generated. The models consist of particle clusters within the particle-depleted matrix. The particle clusters were modeled by either a smeared model in which the particles refine the grains in the cluster, or a discrete model of the particles within clusters. The smeared and discrete models qualitatively agreed with each other. The results suggest that the best TMP to reach a state of reinforcement particle homogeneity was a hot worked, low strain rate TMP.

TABLE OF CONTENTS

I. INTRODUCTION

Composite materials have been used for centuries. Straw in bricks and bulls hair in plaster were used to increase the strength and durability of ancient structures. In more recent years reinforced concrete was one example of a composite material which was a major breakthrough in building technology (Caddell, R. M., 1980; and Parton , V. Z., and Kudryautsev, B. A., 1993).

A modern definition of a composite would be “the combination of a reinforcement material (such as a particle or fiber) in a matrix or binder material” (Strong, A.B., 1989). A more refined definition of a composite includes: 1) The material must be man made. 2) It must be a combination of at least two chemically distinct materials with a distinct interface separating the constituents. 3) The constituent materials forming the composite must be combined three dimensionally. 4) It should be created to obtain properties that would not otherwise be achieved by any of the individual constituents (Taya, M., and Arsenault, R. J., 1989). Under this definition the first modern application of a composite material was a glass reinforced phenolic-nylon fishing pole in 1945. The first production application of Metal Matrix Composites (MMC’s) was boron/aluminum tubes in 1974 as components of the space shuttle. Over the past few decades the manufacture and use of composites have exploded as engineers and consumers have kept looking for stronger, lighter, and more compatible materials. Examples of the application of these improved composite materials include automobile engines, turbine engine components, and aerospace structural components in which the material must operate effectively in harsh environments, and higher strength to weight ratios are critical. The research into new composite materials as well as manufacturing techniques has been of major interest and will continue to be so in the future as engineers strive to design better and more durable systems.

Particle-reinforced metal matrix composites (MMC's) consist of relatively small, hard particles embedded within a softer metal matrix. The reinforcement particle volume fraction may range from 5% to 40 %. Particle sizes are typically one micron or greater. The nature and function of the particles can vary widely, resulting in significantly different material properties. Particulate composites differ from flake and fiber reinforced types, and the additive constituent is usually random in distribution. Because of this, particulate composites are usually assumed to be isotropic (Schwartz, M. M., 1992). Although particle reinforced MMC's exhibit higher strength, stiffness and wear resistance, their use has been limited due to relatively low ductility and fracture toughness.

In order to achieve the improved mechanical properties and an acceptable fracture toughness desired in a particulate MMC, the particles must be dispersed uniformly and homogeneously throughout the matrix material. The production of a MMC consists of two major steps: the initial consolidation of the material, followed by the forming of the material into a useful shape. The fabrication, using either casting methods or powder metallurgy techniques, generally does not result in a uniform dispersal of the particles in the matrix (Taya, M., and Arsenault, R. J., 1989). Therefore, regardless of the consolidation/fabrication technique, the reinforcing particles of MMC's tend to be non-uniformly distributed. As a result, the material properties of such composite materials are poor. Because of this the materials may be subjected to large amounts of straining in the forming process in an effort to achieve a uniform and homogeneous microstructure. McNelley and Ballou (1995) performed an experimental investigation of the mechanisms by which this particle redistribution was taking place in a 6061 AL-AL_2O_3 MMC. Their study examined the role of temperature during the deformation process and the experimental results indicated that the particle distribution became more uniform using a hot thermomechanical process (TMP) as compared to using a cold TMP.

The purpose of this study was to model, using the Finite Element Method (FEM), the hot and cold TMP's of particle-reinforced MMC's. From the FEM models, a qualitative analysis was performed to determine the effects of temperature as well as strain rate in determining the ability of a cluster of particles, or the particles themselves, to move within the matrix and thus achieve a state of homogeneity while undergoing large strains. A qualitative evaluation was performed of the stresses and strains achieved within the matrix while undergoing the TMP's. The objective was to then determine, from a qualitative viewpoint, what condition of TMP's would result in, as close as possible, the homogeneous particle redistribution to achieve the desired mechanical properties of a particle-reinforced MMC.

II. BACKGROUND

A. THEORY OF CONSTITUTIVE EQUATIONS

The theory of plasticity is concerned with the study of stresses and strains in plastically deformed materials such as metals. The theory is used to develop constitutive laws relating stresses to strains in plastically deformed solids (Hill, R., 1956). These constitutive laws may then be used to model large deformations of the solid material while it is either subjected to cold-working or hot-working. In the present discussion of the constitutive laws only isotropic material is considered.

1. Strain Hardening Plasticity

Plasticity of a cold material occurs when the applied stress acting on the material exceeds its yield strength (i.e. $\sigma > \sigma_0$; where σ = applied stress and σ_0 = yield strength). Once this occurs, plastic flow begins. Below in Figure 1 is a plot of stress vs. strain depicting the behavior of a material that is plastically deformed. The solid line from A to C shows the loading of the material to an applied stress above yield strength with subsequent unloading along the dashed line from C to D. The subsequent behavior of the material following this process is such that the yield strength will increase to the value of the maximum applied stress during this process, and the elastic modulus of the material will remain constant. This phenomena is known as strain hardening.

There are two commonly used general theories which predict initiation of plastic flow, Tresca's flow criterion and von Mises' flow criterion.

Stress vs. Strain

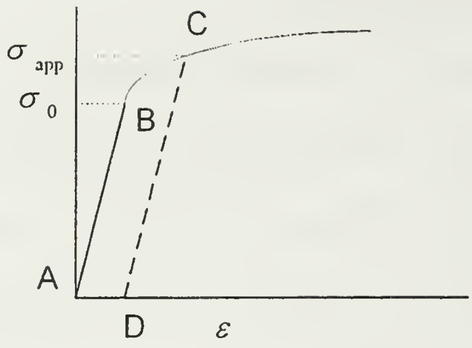

Figure 1: Stress vs. Strain behavior for a material which is plastically deformed. σ_{app} = applied stress and σ_0 = yield stress.

Tresca's flow criterion is based on the maximum shear stress being greater than the shear yield or flow strength of the material. Specifically,

$$\tau_{max} = \tau_0 \tag{2.1}$$

where τ_0 = shear yield stress, and the maximum shear stress is expressed as

$$\tau_{max} = (\sigma_1 - \sigma_3)/2 \tag{2.2}$$

Therefore, Eq. (2.1) can be rewritten as

$$\sigma_1 - \sigma_3 = \sigma_0 \tag{2.3}$$

where $\sigma_1 \geq \sigma_2 \geq \sigma_3$, and $\sigma_1, \sigma_2,$ and σ_3 are the principal stresses and

$$\tau_0 = \sigma_0/2 \tag{2.4}$$

Plastic flow occurs when $\tau_{max} > \tau_0$. For a biaxial state of stress (i.e. one of the principal stresses are zero, σ_3 in this case) the following plot in Figure 2 is generated. This is a two dimensional plot of the yield locus. The area inside the yield locus represents the principal stress combinations in which no yielding occurs, while stress combinations outside the yield locus cause yielding and plastic flow begins. In three dimensions this plot look like a hexagonal prism with its central axis aligned 45^0 from each of the principal axes.

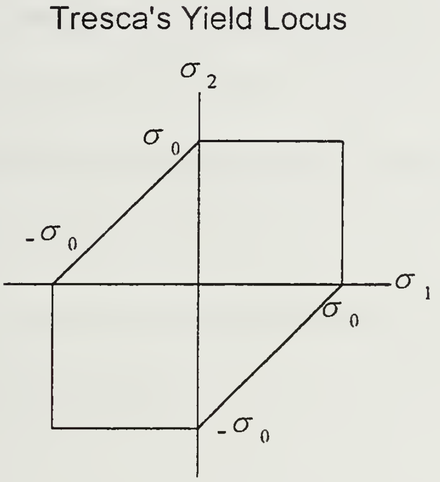

Figure 2: Tresca's Yield Locus.

The von Mises' flow criterion is based on distortion energy. Yielding begins when the elastic energy of distortion reaches a critical value. Hydrostatic pressure is assumed not to contribute to yielding because it only produces a dilatational strain energy (Hill, R., 1956). As a result, yielding begins where $\sigma_{eff} \geq \sigma_0$ where

$$\sigma_{eff} = (1/\sqrt{2})[(\sigma_1 - \sigma_2)^2 + (\sigma_2 - \sigma_3)^2 + (\sigma_3 - \sigma_1)^2]^{1/2}. \quad (2.5)$$

Again, for a biaxial stress state it can be shown that

$$\sigma_{eff} = (1/\sqrt{2})[\sigma_1^2 - \sigma_1\sigma_2 - \sigma_2^2]^{1/2} \quad (2.6)$$

and the yield locus for the von Mises' criterion is shown below in Figure 3. For three-dimensional principal stresses, the shape takes the form of a right circular cylinder with its central axis aligned 45^0 from all of the principal axes.

It should be noted here that for isotropic materials and isotropic strain hardening, the right circular cylinder will expand equally in three dimensions as σ_0 increases.

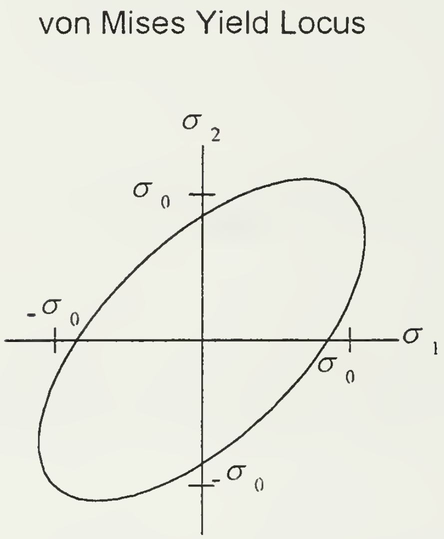

Figure 3: The von Mises Yield Locus.

In terms of the stress tensor, σ_{ij}, the following may be shown. First

$$\sigma_{ij} = \sigma'_{ij} + \delta_{ij}\sigma_m \tag{2.7}$$

where σ'_{ij} is the deviatoric stress, δ_{ij} is the Kroneker delta and σ_m is the hydrostatic stress component. Plastic flow is only dependent of the deviatoric stress component. For a state of uniaxial stress, equations 2.8 and 2.9 may be derived:

$$\sigma'_1 = -2\sigma'_2 = -2\sigma'_3 \tag{2.8}$$

$$\delta\varepsilon_1 = -2\,\delta\varepsilon_2 = -2\,\delta\varepsilon_3 \qquad (2.9)$$

Equation (2.9) assumes that no volume change occurs during the plastic deformation. Therefore the following equations hold true:

$$\delta\varepsilon_1/\delta\varepsilon_2 = -2 \qquad (2.10)$$

$$\delta\varepsilon_1/\delta\varepsilon_2 = \sigma'_1/\sigma'_2 \qquad (2.11)$$

$$\delta\varepsilon_1/\sigma'_1 = \delta\varepsilon_2/\sigma'_2 = \delta\varepsilon_3/\sigma'_3 \qquad (2.12)$$

Based on the preceding equations, it can be assumed that

$$\delta\varepsilon_{ij}/\sigma'_{ij} = \delta\lambda \qquad (2.13)$$

where $\delta\lambda$ is the scale factor of proportionality. This results in the Levy-Mises equation which is rewritten as

$$\delta\varepsilon_{ij} = \sigma'_{ij}\,\delta\lambda\,. \qquad (2.14)$$

The extension of the Levy-Mises equation to account for the elastic component of strain was performed by Prandtl and Reuss and takes the form,

$$\delta\varepsilon^{P}_{ij} = \sigma'_{ij}(3\,\delta\,\overline{\sigma})/(2\,\overline{\sigma}\ H') \qquad (2.15)$$

where $\overline{\sigma}$ is the effective von Mises stress and H' is the slope of the equivalent stress/plastic strain curve (Hill, R., 1956). However,

$$(\delta\,\overline{\sigma}/H') = \delta\,\overline{\varepsilon}_p \qquad (2.16)$$

where $\delta\,\overline{\varepsilon}_p$ is the equivalent plastic strain increment which in turn is defined as

$$\delta\,\overline{\varepsilon}_p = ((2/3)\,\delta\varepsilon^{p}_{ij}\,\delta\varepsilon^{p}_{ij})^{1/2}. \qquad (2.17)$$

Thus the Reuss-Prandtl equation becomes

$$\delta\varepsilon^{P}_{ij} = \sigma'_{ij}(3\,\delta\,\overline{\varepsilon}_p)/(2\,\overline{\sigma}). \qquad (2.18)$$

It is the Reuss-Prandtl equation which relates the incremental plastic strain to the deviatoric stress component, the instantaneous hardening rate and the effective von Mises stress. Equation (2.18) is the constitutive equation relating stress and strain which is used for the cold worked models in this work.

2. Creep

The behavior of the solid at elevated temperatures is governed by thermally activated processes. The strength of solids at high temperatures is strongly dependent on strain rate, $\dot{\varepsilon}$, and temperature. Strain hardening is reduced because recovery processes predominate and the strength of the material can be characterized according to its creep resistance. The two environmental factors influencing creep are temperature and stress (Sherby, O. D., and Burke, P. M., 1968).

Figure 4 shows the three stages of creep for a polycrystalline metallic solid. The first stage is known as primary creep; in this interval of strain the metal is hardening, and this is apparent in the decreasing creep rate. The second stage of creep, also known as secondary creep, is the stage in which the creep rate is constant. In this stage the substructure developed has a strong dependency on stress and temperature. The third stage, known as tertiary creep, is often associated with localized necking and void formation under tension. This stage leads to material failure, and is characterized by an increasing strain rate (Sherby, O. D., and Burke, P. M., 1968). As either temperature or stress increases, the slope and the strain rate of all three regions increases. The secondary stage of creep where the creep rate in constant is the area of interest for hot working.

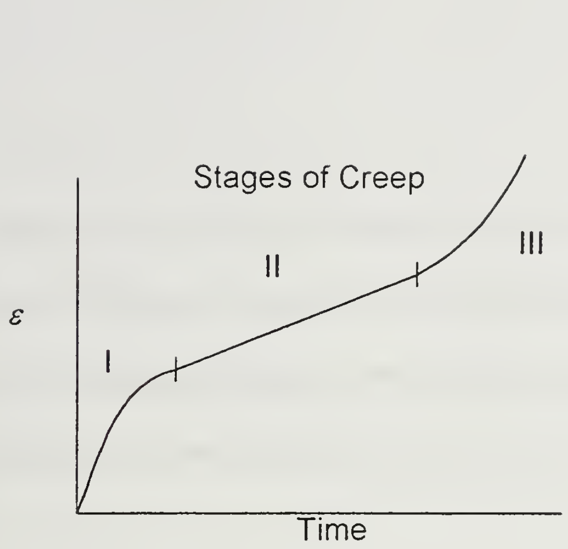

Figure 4: The three stages of creep shown as strain, ε, vs. time.

Creep is a thermally activated process. Above temperatures of $0.5T_m$, where T_m is the melting temperature of the material, the creep rate is dependent on dislocation climb. This is often referred to as dislocation creep. Because climb is a diffusion-controlled process the steady state creep rate tends to be proportional to the diffusion coefficient:

$$\dot{\varepsilon} = kDf(\sigma) \tag{2.19}$$

where

$$D = D_0 \exp(-Q/RT) \tag{2.20}$$

is the diffusion coefficient, T = absolute temperature, R = universal gas constant, Q = activation energy for creep, and D_0 and k are constants. This indicates a direct relationship between $\dot{\varepsilon}$ and D. Because of this direct relationship it can be shown

$$\dot{\varepsilon} = K_i f(\sigma) \tag{2.21}$$

where $K_i = kD_0$

or

$$\dot{\varepsilon} = K_i \sigma^n. \tag{2.22}$$

At low stresses creep is believed not to be due to dislocation climb but due to stress directed atom migration. Here, the stress will bias the direction of vacancy diffusion within grains and they will elongate in the direction of the applied tensile stress; this is often referred to as diffusional creep or as the Nabarro-Herring creep mechanism as illustrated below in Figure 5.

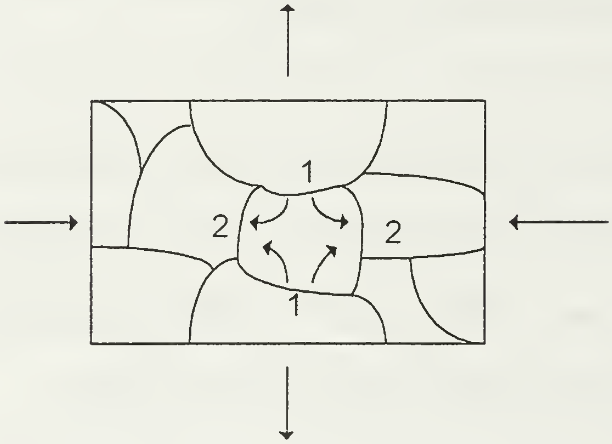

Figure 5: Schematic of the Nabarro-Herring diffusional creep model. "The vacancy concentration in region 1 is higher than the vacancy concentration in region 2 for the central grain illustrated. Vacancies will therefore flow in the direction shown by the arrows, or, which is the same, atoms will flow in the opposite direction leading to elongation of the grain in the tensile direction of the applied stress" (Sherby, O. D., and Burke, P. M., 1968).

The type of creep relation given by Nabarro-Herring can be written as

$$\dot{\varepsilon} = K_1 \sigma^1 \tag{2.23}$$

and is thus known as the linear law. At higher stresses the intermediate stress law is where dislocation climb or the non-conservative motion or jogs of screw dislocations is the mechanism of creep and expressed as

$$\dot{\varepsilon} = K_2 \sigma^5 \qquad (2.24)$$

for pure metals (Sherby, O. D., and Burke, P. M., 1968).

If creep is dependent on two thermally activated processes, i.e., dislocation creep and diffusional creep, each contributing independently to plastic flow, the fastest process is always rate controlling. This is shown below in Figure 6.

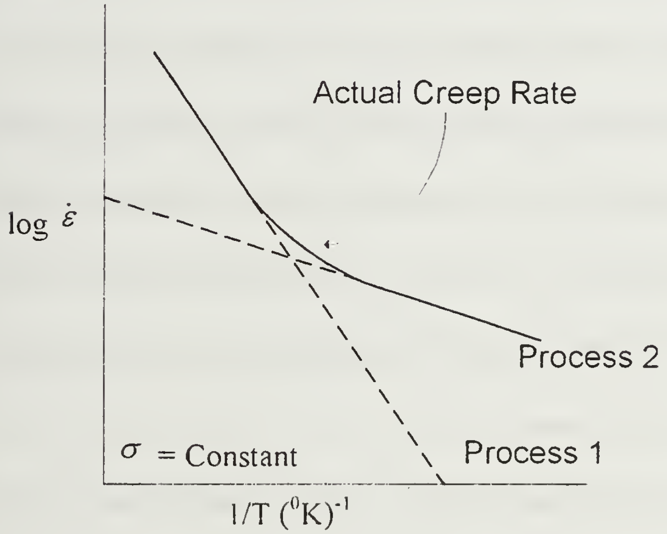

Figure 6: Schematic of two different processes of creep. “When two independent processes control creep, the fastest is rate controlling. If each process has a different activation energy the observed activation energy for creep will change with temperature, increasing with increasing temperature” (Sherby, O. D., Burke, and P. M., 1968).

Grain Boundary Sliding (GBS) is also a form of diffusional creep where the grains slide along the boundaries after diffusion of vacancies within the grains has occurred. Normally in the intermediate stress range it is not a dominant mechanism due to the relatively large grain sizes found in pure metal. GBS typically becomes the dominant mechanism of creep for grain sizes less than ten microns. For GBS the strain rate-stress relationship has been experimentally shown to be (Sherby, O. D., and Wadsworth, J., 1982)

$$\dot{\varepsilon} = K_3\sigma^2. \qquad (2.25)$$

Because of the high density of particles within the cluster regions of MMC's it is thought that Particle Stimulated Nucleation (PSN) of recrystallization within clusters of reinforcement particles will result in different elevated-temperature flow characteristics within these regions. These regions exhibit recrystallization in the early stages (0.1-0.25 true strain) of processing and thus behave as fine grained structures. Fine-grain metals may deform by grain boundary sliding (GBS) at elevated temperatures and are weaker than coarse grained metals. If GBS is the dominant deformation mechanism within clusters than they may deform at different rates when compared to the matrix. Such differences in flow behavior are analyzed here.

The constitutive laws thus developed for hot worked models are shown in equation (2.24), $\dot{\varepsilon} = K_2\sigma^5$, for the matrix material; and in equation (2.25), $\dot{\varepsilon} = K_3\sigma^2$, for the material within clusters if recrystallization has occurred.

B. FINITE ELEMENT METHOD (FEM)

The finite element code used to perform this work was LS-DYNA3D, a vectorized explicit three-dimensional finite element code for analyzing the large deformation dynamic response of inelastic solids. The code was developed by the Livermore Software Technology Corporation (LSTC) in Livermore, California (Hallquist, J. O., 1991). The FEM program is based on the Lagragian description of the body. The central difference technique is also utilized in the code for time integration. For further technical and theoretical information about the program the reader is referred to the theoretical manual (Hallquist, J. O., 1991). In the models eight-node hexahedron solid elements were used under plane strain conditions. The detailed description of the models, including the meshes and boundary conditions as well as the constitutive equations, is provided in subsequent chapters.

In the present model each cluster zone remains as a single entity even after large deformation. In other words, the model does not allow for breaking down of a single cluster into smaller clusters and for mixing within the surrounding matrix material. This mixing phenomenon certainly happens in actual deformation processing of composites and further experimental study is needed to gain better insight into the actual physical mechanisms occurring within MMC's during TMP. The subsequent study should improve the modeling technique to more closely describe the actual phenomena. For this purpose a Eulerian-Lagrangian technique of the FEM will likely be more suitable.

III. SMEARED PARTICLE CLUSTER MODELS OF METAL MATRIX COMPOSITES

A. DEVELOPMENT OF THE MODELS FOR COLD WORKING

A few assumptions were made in the development of the particle reinforced MMC models. In the initial consolidation of a particle reinforced MMC the reinforcement particles are assumed to be non-homogeneously distributed within the matrix material, there being local particle-rich areas interspersed with matrix-rich areas. This circumstance was simplified in the model; two separate homogeneous entities were assumed: one is the particle-rich area, modeled as a cluster, and the other is the matrix-rich area modeled as pure matrix material. The shape of the cluster regions was modeled as a cylindrical region, or a circular area in two-dimensional space. This can be seen in Figures 7 to 10 that show the different meshes prior to deformation.

An assumption made specifically for the cold deformation model was that the material behaved as an elastic-plastic material with isotropic strain hardening. The related theory of plasticity was discussed in Chapter II. Table 1 lists the material properties used for the cluster material and matrix material used in the cold rolled models. The cluster region is modeled as a homogeneous material with the effects of the increased fraction of reinforcement particles within the cluster being increased Young's modulus, E, and the strain hardening coefficient to 150% of their values compared to the pure matrix material. Such an increased modulus E, corresponds to a SiC or AL_2O_3 particle volume fraction of 0.25 within the clusters residing in an Al matrix. Because no particles are assumed to be present in the matrix, the modulus, E, is that of unreinforced Al. A similar proportional increase in strain hardening rate was assumed for the purpose of this analysis.

Table 1: Material properties of the matrix material and cluster material used in the cold worked models.

Material Properties of the matrix material and cluster material		
Material type	Matrix material	Cluster Material
Yield Stress	40 ksi	45 ksi
Young's Modulus, E	$10.4*10^6$ psi	$15.6*10^6$ psi
Strain Hardening Coeff.	100 ksi	150 ksi

B. DEVELOPMENT OF THE FEM MESHES

The overall geometry of the MMC model consists of a three dimensional block containing zones representing the clusters. There are four basic mesh geometry's shown below in Figures 7 to 10. The boundary conditions imposed on the models are as follows. The symmetry boundary condition is imposed on the left hand side of the model where the left hand nodes are constrained to allow motion in the vertical direction only. The model is also constrained on the front and the back surfaces to correspond to the plane strain condition. The bottom of the model is set on a stationary rigid body with no friction between the material and the rigid body. This allows the material to slide along the rigid body surface. The top of the model is also against a rigid body with no friction, but the top rigid body is in motion in the downward direction at a constant velocity. The right hand side of the model is free to move; however, when in contact with the top or bottom rigid body there is no friction between the rigid bodies and the model is therefore allowed to slide. In Figure 7 the model contains two particle clusters located side by side. Figure

8 shows two clusters in a vertical orientation with the same spacing as the previous model. In this and subsequent figures of the mesh, the two rigid bodies at the top and bottom of the block are not shown. Figure 9 shows six clusters in a square arrangement and Figure 10 shows these same six clusters with identical spacing but in a diamond arrangement.

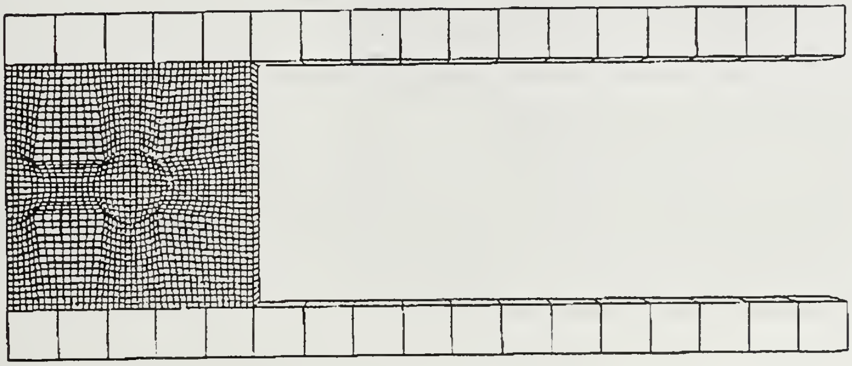

Figure 7: Mesh of two cluster regions oriented horizontally.

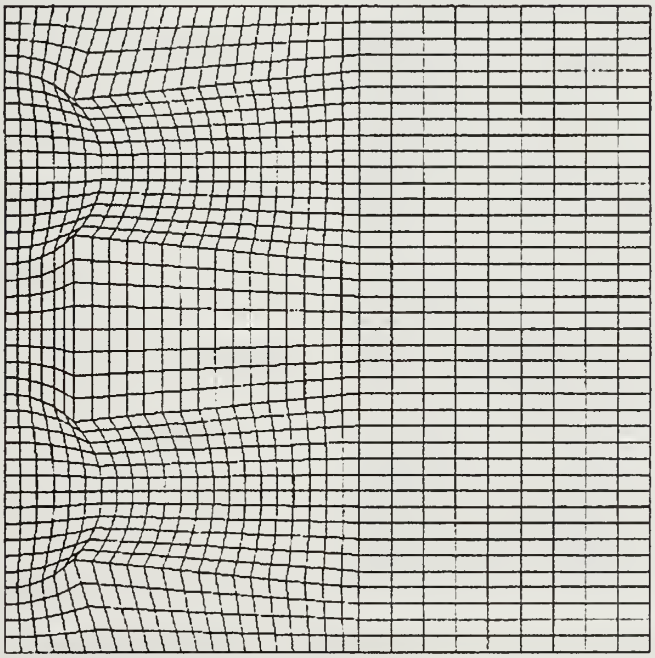

Figure 8: Mesh of two cluster regions oriented vertically.

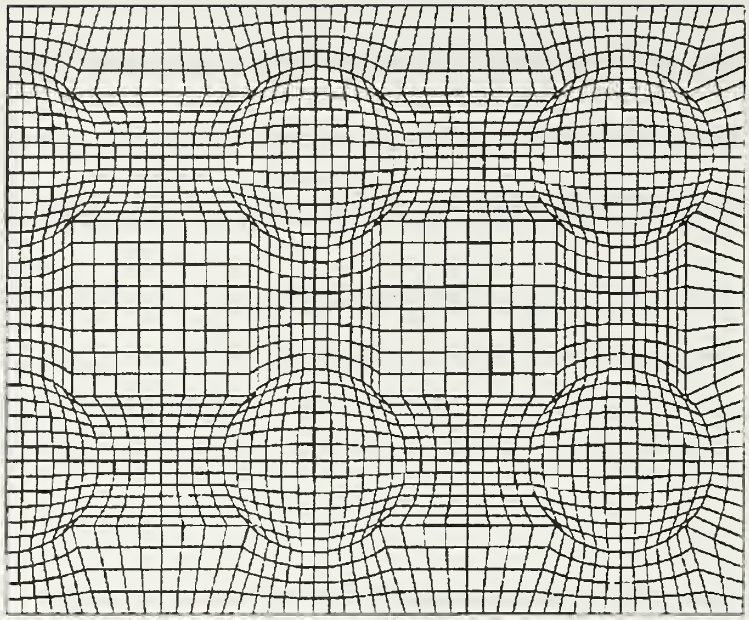

Figure 9: Mesh of six cluster regions in a repeating square arrangement.

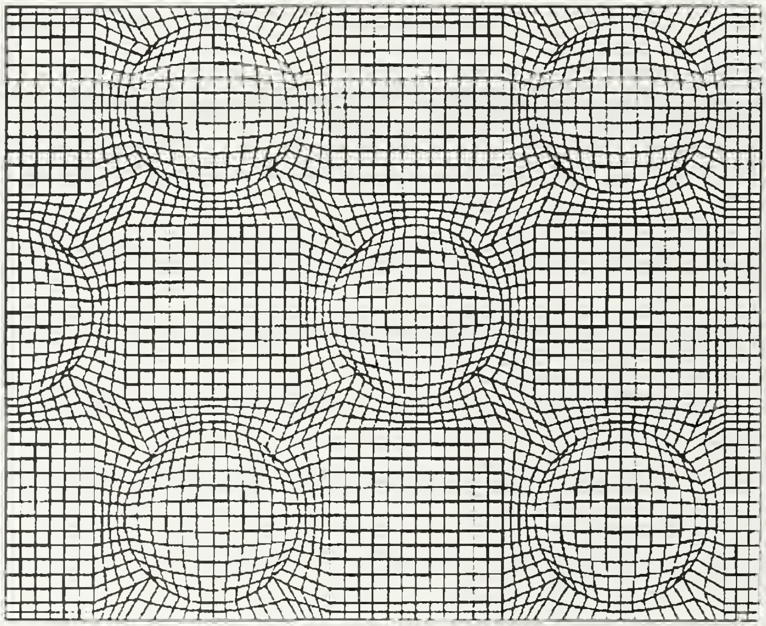

Figure 10: Mesh of six cluster regions oriented in a repeating diamond arrangement.

C. STRESS AND STRAIN RESULTS OF COLD WORKING

All models were subjected to a large deformation (corresponding to a natural strain of about 1.2). The fringe plots of effective von Misses stress and the fringe plots of effective plastic strain for all the cold worked models at a state of 1.20 true strain are shown in Appendix A; the exception is that the diamond shaped model is at a true strain of 1.13. The models of cold deformation indicate significantly higher stresses within the cluster regions and relatively lower strains as compared to the surrounding matrix material. Looking specifically at the diamond cluster arrangement, for example, in Figure 11 it can be seen that the stresses in the cluster region range up to 233 ksi while in the stresses in the matrix region are as low as 102 ksi.

This is expected behavior of all the models because the clusters have higher yield strength and stiffer modulus. Looking at the fringes of effective plastic strain, shown in Figure 12, it is noted that the higher strain regions in the range of up to 1.40 effective plastic strain are within the matrix material at the center of the diamond shaped cluster arrangement. The lowest effective plastic strains are experienced in the cluster regions themselves and range from 0.65 to 1.22.

D. DEVELOPMENT OF HOT WORKED MODELS

The models of hot deformation used the same meshes as the cold work models and were shown previously in Figures 7 to 10. This was done so that a direct qualitative comparison could be made between the two different TMP approaches. These models invoke the power law of viscoplasticity in the intermediate stress range of creep (Sherby, O. D., and Burke, P. M., 1968) and utilize the constitutive equation:

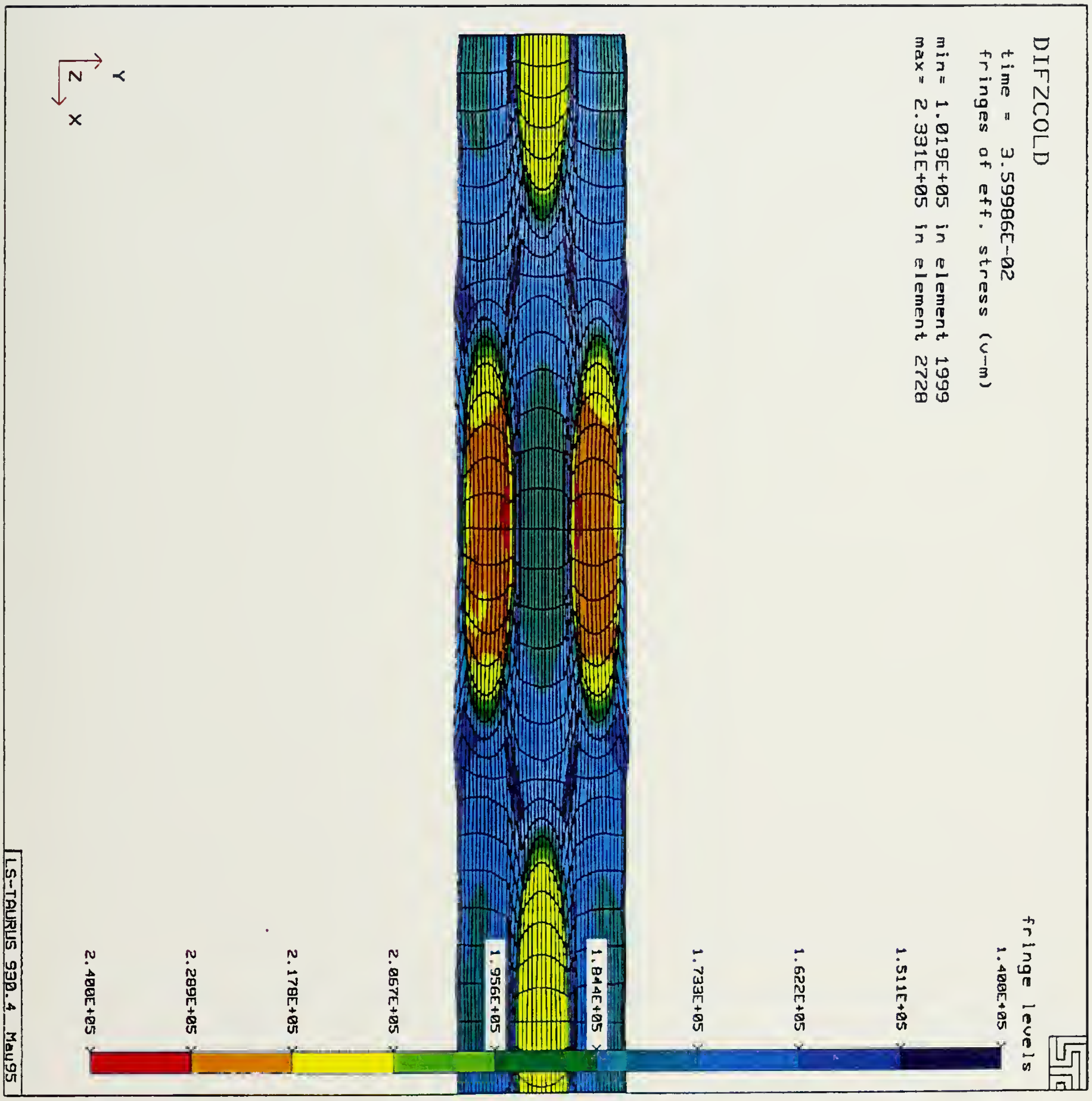

Figure 11: Fringe plot of effective von Mises stress for the diamond distribution model after cold working to a true strain of 1.13.

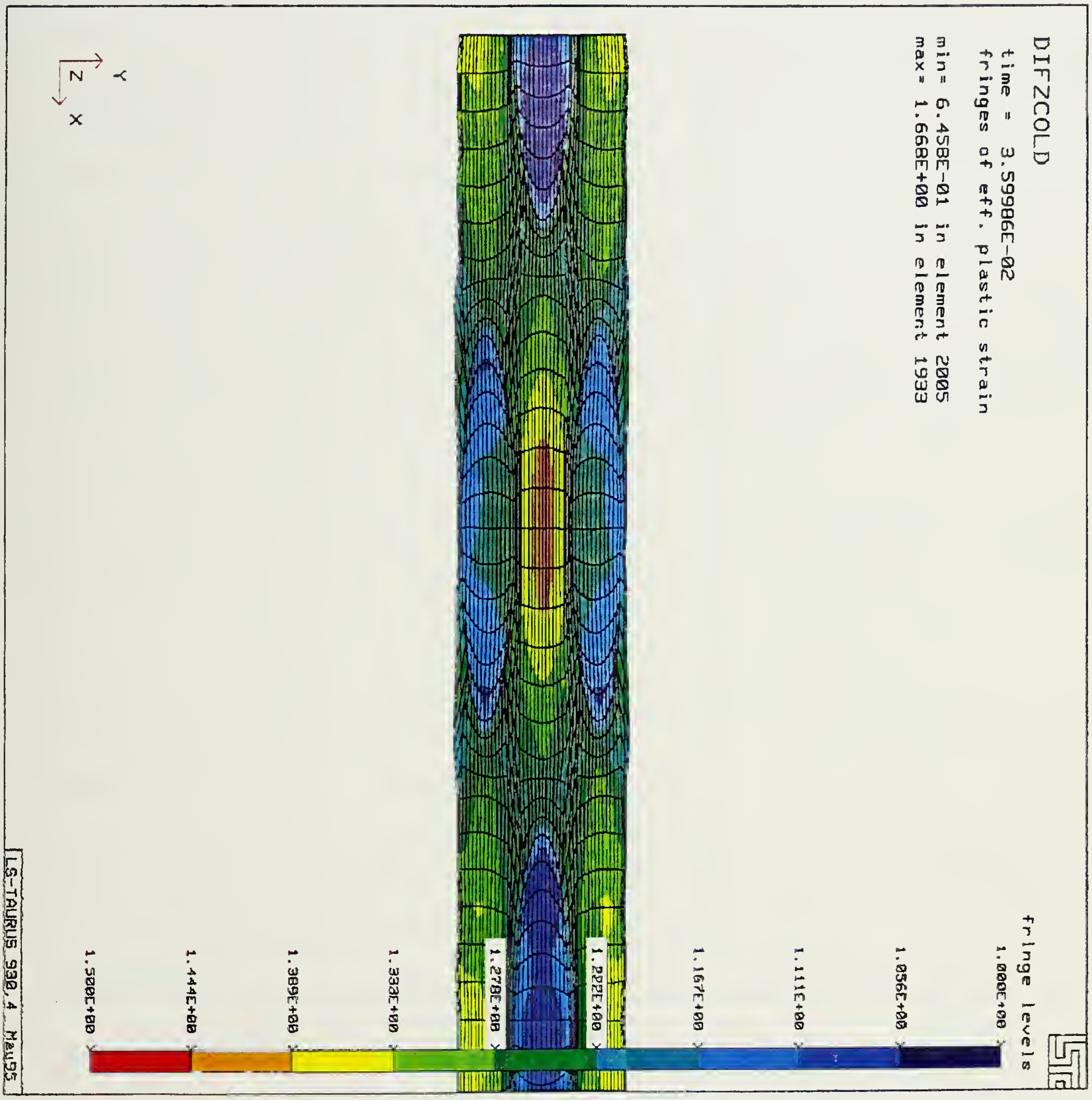

Figure 12: Fringe plot of effective plastic strain for the diamond distribution model after cold working to a true strain of 1.13.

$$\sigma = k\varepsilon^{m}\dot{\varepsilon}^{n}. \qquad (3.1)$$

In Eq. (3.1) m=0 and n and k vary depending on the location in the MMC.

The following additional assumptions are used in the high temperature modeling process. First, the temperature during the hot working is assumed to be above $0.5T_m$, where T_m is the melting temperature of the material. Next, it is assumed the matrix material behaves such that the mechanism for creep is dislocation climb and therefore n=5 in Eq. (3.1). This assumption was discussed earlier in Chapter II. In the cluster material grain boundary sliding (GBS) is assumed to be the mechanism of creep. Because of particle stimulated nucleation (PSN) of recrystallization within clusters after very small strains, it is assumed that grain boundary sliding (GBS) becomes the predominate deformation mechanism and therefore n=2 in Eq. (3.1) (Sherby, O. D., Wadsworth, J., 1982). Because the constitutive law is based on strain rates, the models were deformed using three different nominal strain rates. These strain rates include a high strain rate of 33.3 s^{-1}, an intermediate strain rate of 3.33 s^{-1}, and a low strain rate of 0.333 s^{-1}. To determine the k values to be used in the Eq. (3.1), plots of strain rate divided by the diffusion coefficient, D, vs. creep stress were used (Sherby, O. D., Wadsworth, J., 1982). The n=2 power law and the n=5 power law were assumed to intersect at the intermediate strain rate. This is illustrated below in Figure 13. Note that in Figure 13, the line with the steepest slope represents the dislocation climb creep mechanism while the other line represents the GBS mechanism. It was then determined from the graph that, at a nominal stress of 5000 psi and a nominal strain rate of 3.33 s^{-1}, that k = 3937 for the matrix material and k = 2732 for the cluster material. Note from Figure 13 that, if the strain rate

is high, the n=2 power law results in significantly higher stresses. In reality this does not occur because the n=5 power law will dominate (i.e. dislocation climb) the physical behavior. Therefore the 'k' value for the cluster material equals the 'k' value for the matrix material in the high strain rate model.

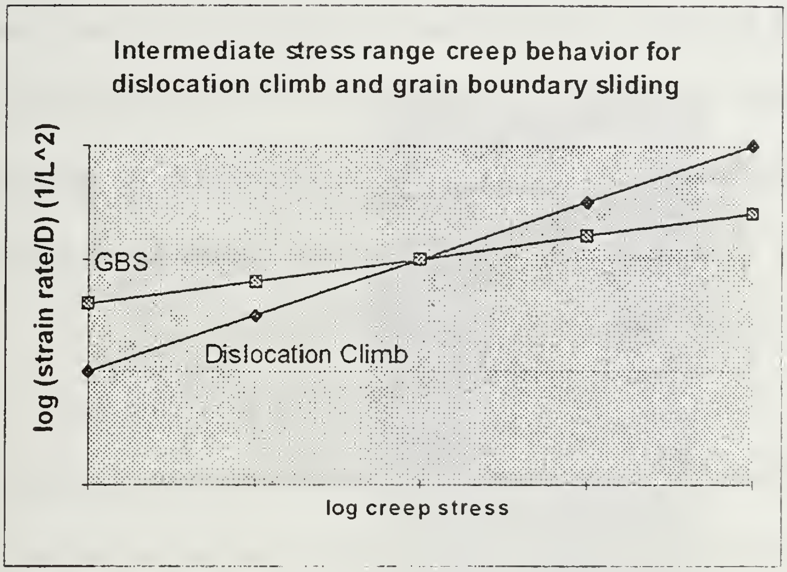

Figure 13: Log-Log plot of intermediate creep stress vs. (strain rate/D) where D = Diffusion Coefficient.

It may be argued that the Nabarro and Herring (NH) diffusional creep law, where n=1 in Eq. (3.1), is the mechanism by which creep would occur in the fine-grained clusters. This is not believed to be the case here; because NH creep is normally associated only with deformation near the melting temperature ($T > 0.9\ T_m$) and in the very lowest creep stress range (Sherby, O.D., and Burke, P.M., 1968). However, one model run using the square cluster arrangement was generated using the linear law, n=1 and k = 1501.5 in Eq.(3.1). The resulting cluster response was very similar to the results using the n=2 power law. Because of this, the low and intermediate strain rate models were all generated using the n=2 power law.

E. STRESS AND STRAIN RESULTS OF HOT WORKING

The fringe plots of effective von Misses stress and the fringe plots of effective plastic strain for all the hot deformation models at a state of approximately 1.20 true strain, with the exception of the diamond cluster arrangement which was deformed again to 1.13 true strain, are shown in Appendix B. It is noted that in the high strain-rate models no distinction between the cluster regions and the matrix material is evident as shown in Figures 14 and 15. This result is expected because the mechanism of creep is dislocation climb within both the clusters and the matrix.

In the intermediate strain rate analysis the higher stresses were observed to be within the cluster material. The effective plastic strains are also higher within the clusters (note Figures 16 and 17). In the earlier stages of hot working at the intermediate strain rate, the models do exhibit lower stresses within the clusters. Not until a value of 1.0 true strain is reached do the higher stresses in the cluster region become apparent. Near the end of the deformation process the strain rates are higher, because of the prescribed constant velocity of the rigid body, and the mechanism of creep within the cluster regions should change from GBS to dislocation climb. The computer code allows for the constitutive law to be expressed as a power function, i.e., $\dot{\varepsilon}_1 = K_1\sigma^2$ or $\dot{\varepsilon}_2 = K_2\sigma^5$, where in fact the form of the constitutive law when one has differing grain sizes should be

$$\dot{\varepsilon}_T = \dot{\varepsilon}_1 + \dot{\varepsilon}_2. \tag{3.2}$$

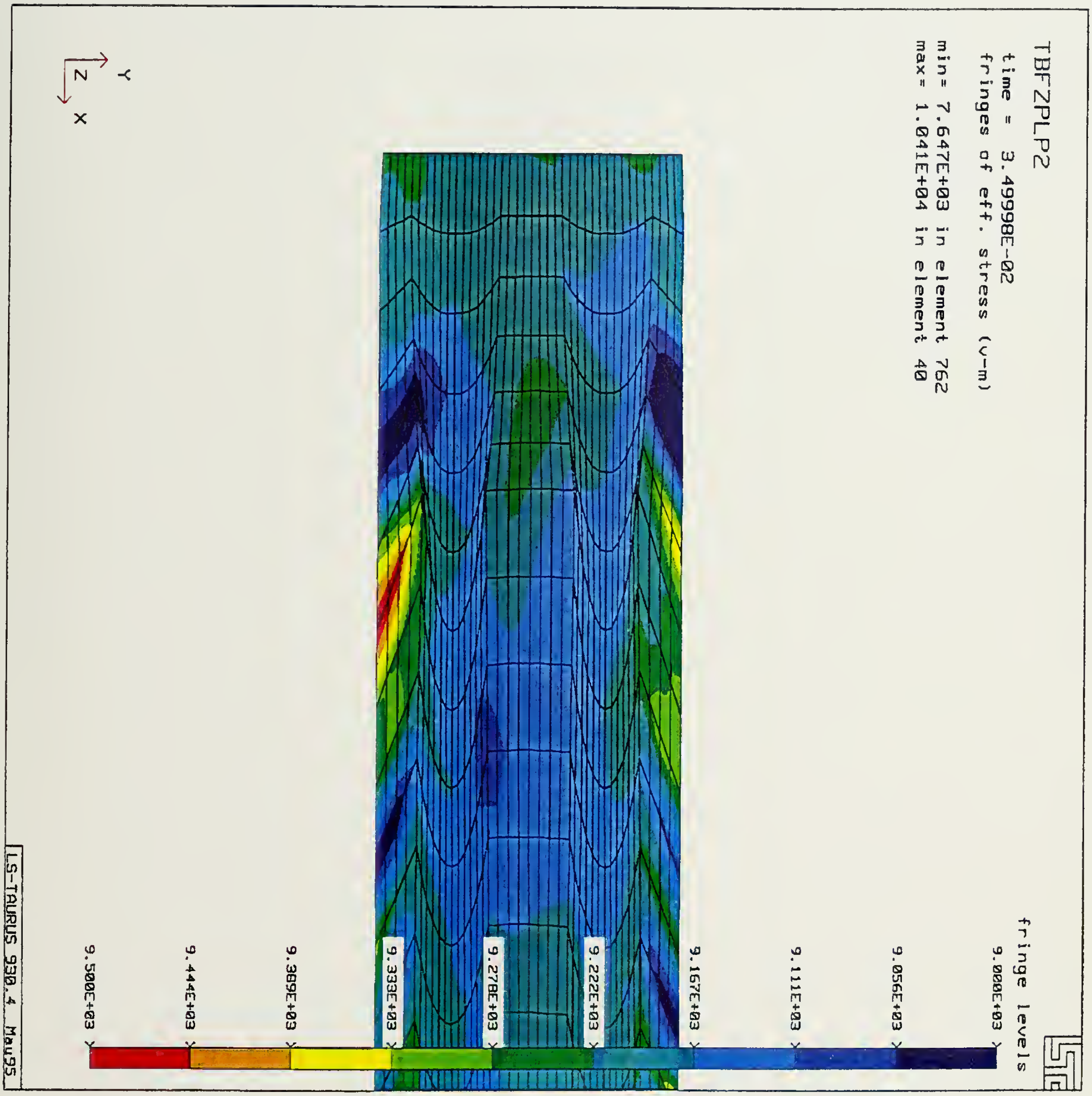

Figure 14: Fringe plot of effective von Mises stress for the two cluster vertical arranged model after hot working at a high strain rate to a true strain of 1.20.

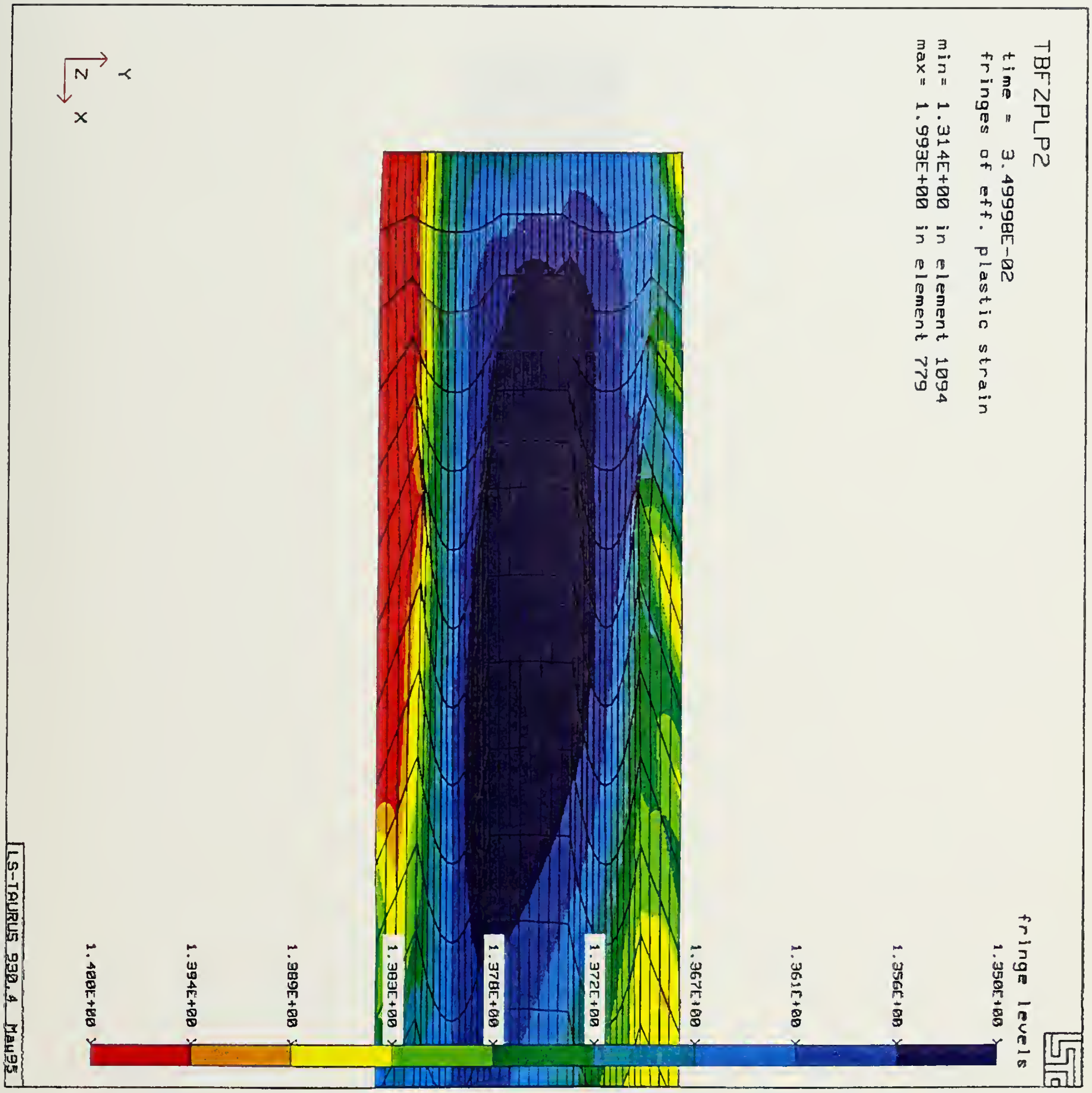

Figure 15: Fringe plot of effective plastic strain for the two cluster vertical arranged model after hot working at a high strain rate to a true strain of 1.20.

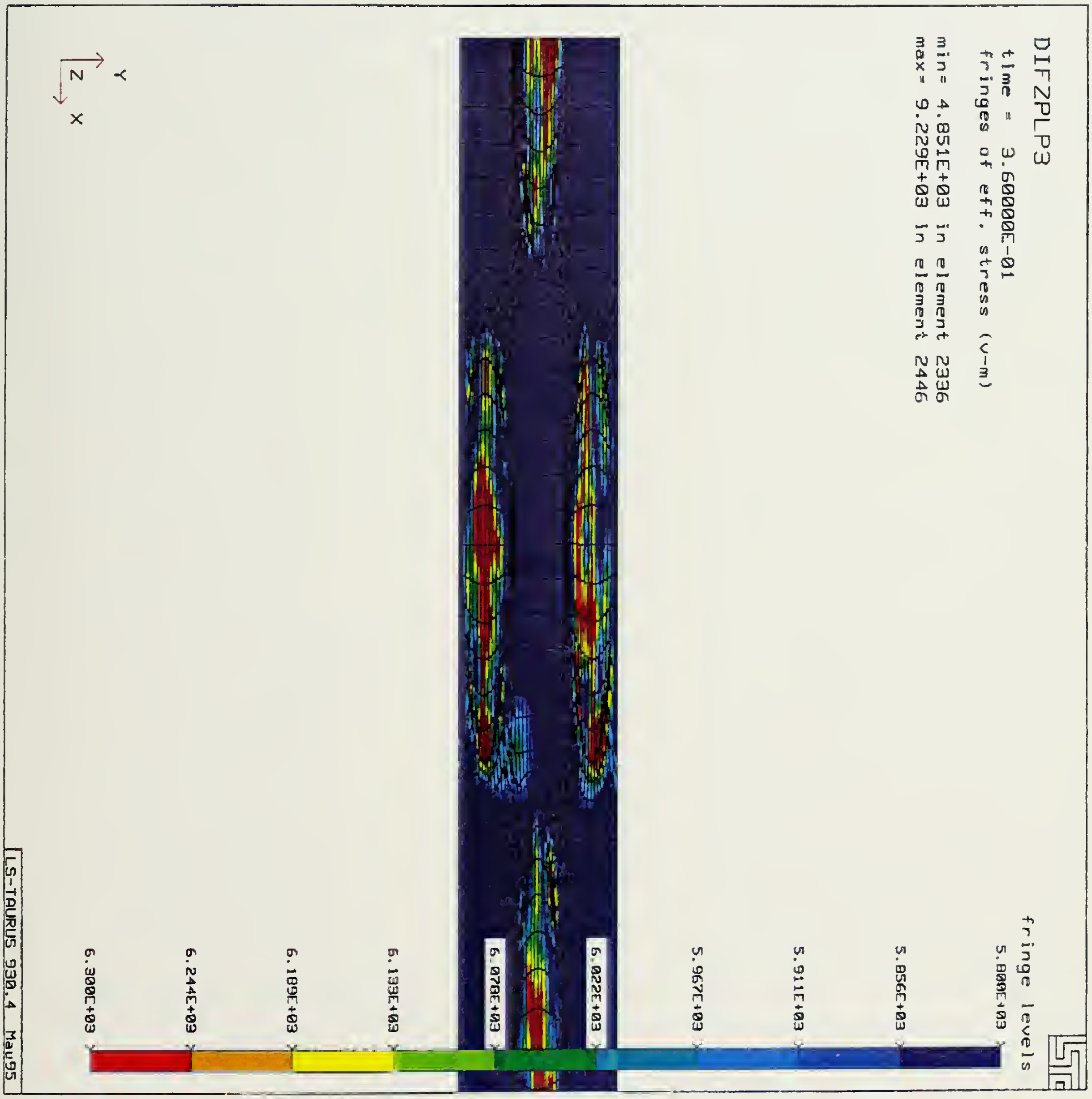

Figure 16: Fringe plot of effective von Mises stress for the diamond arranged model after hot working at an intermediate strain rate to a true strain of 1.13.

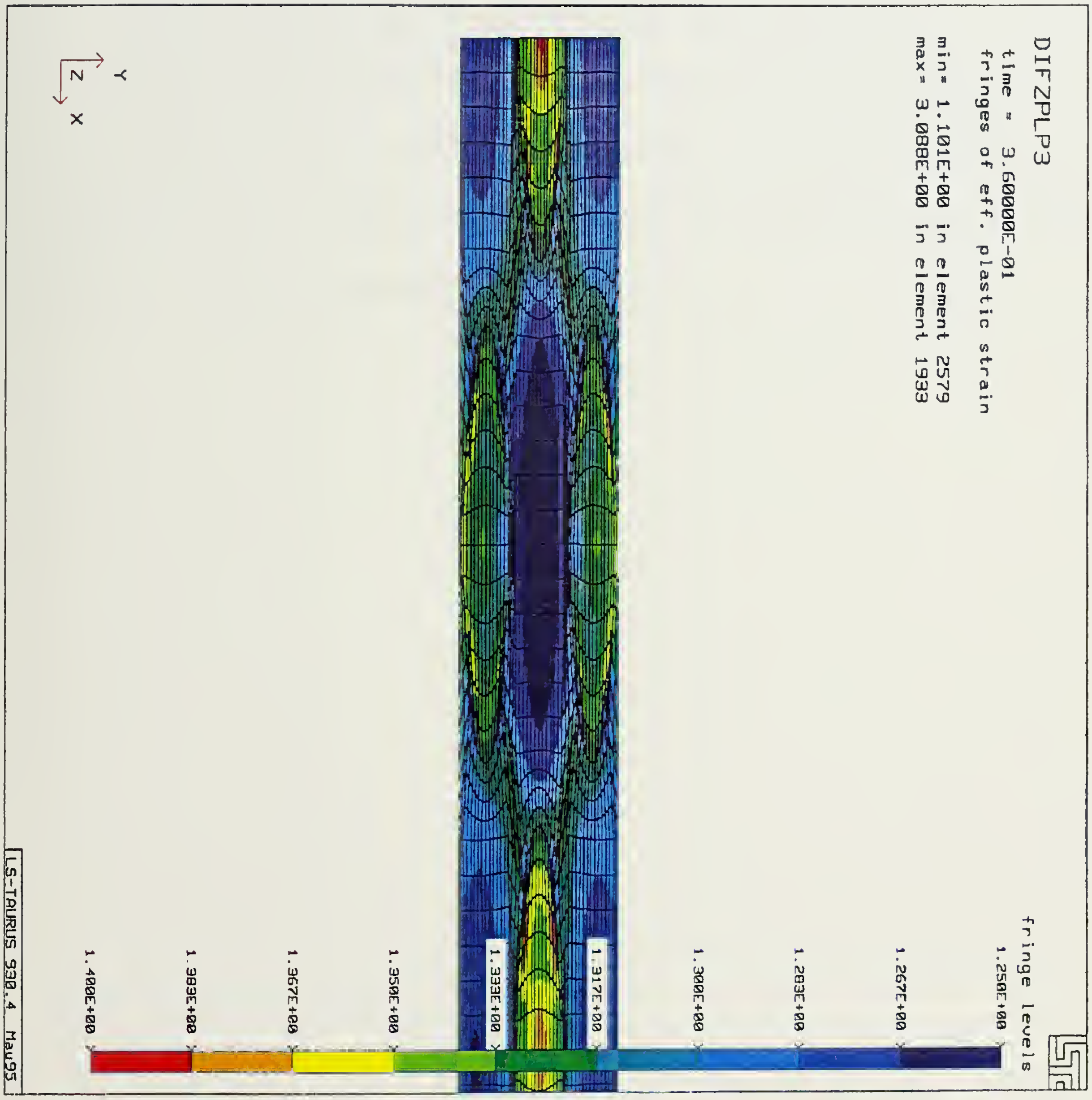

Figure 17: Fringe plot of effective plastic strain for the diamond arranged model after hot working at an intermediate strain rate to a true strain of 1.13.

This additive form of the rate law is not accepted by the current computer codes. It is at an intermediate strain-rate where this limitation will result in significant inaccuracies and cannot be ignored. This is one of the limitations of the current models and needs to be improved in future study.

The low strain rate models result definitively in lower stresses as well as higher effective plastic strains in the cluster material (note Figures 18 and 19). The one exception to this is that in the square model the strain in the cluster does not differ from the matrix material (see Figure 20). The comparison of the linear law and the n=2 power law models at the low strain rate is illustrated in Figures 20 to 23.

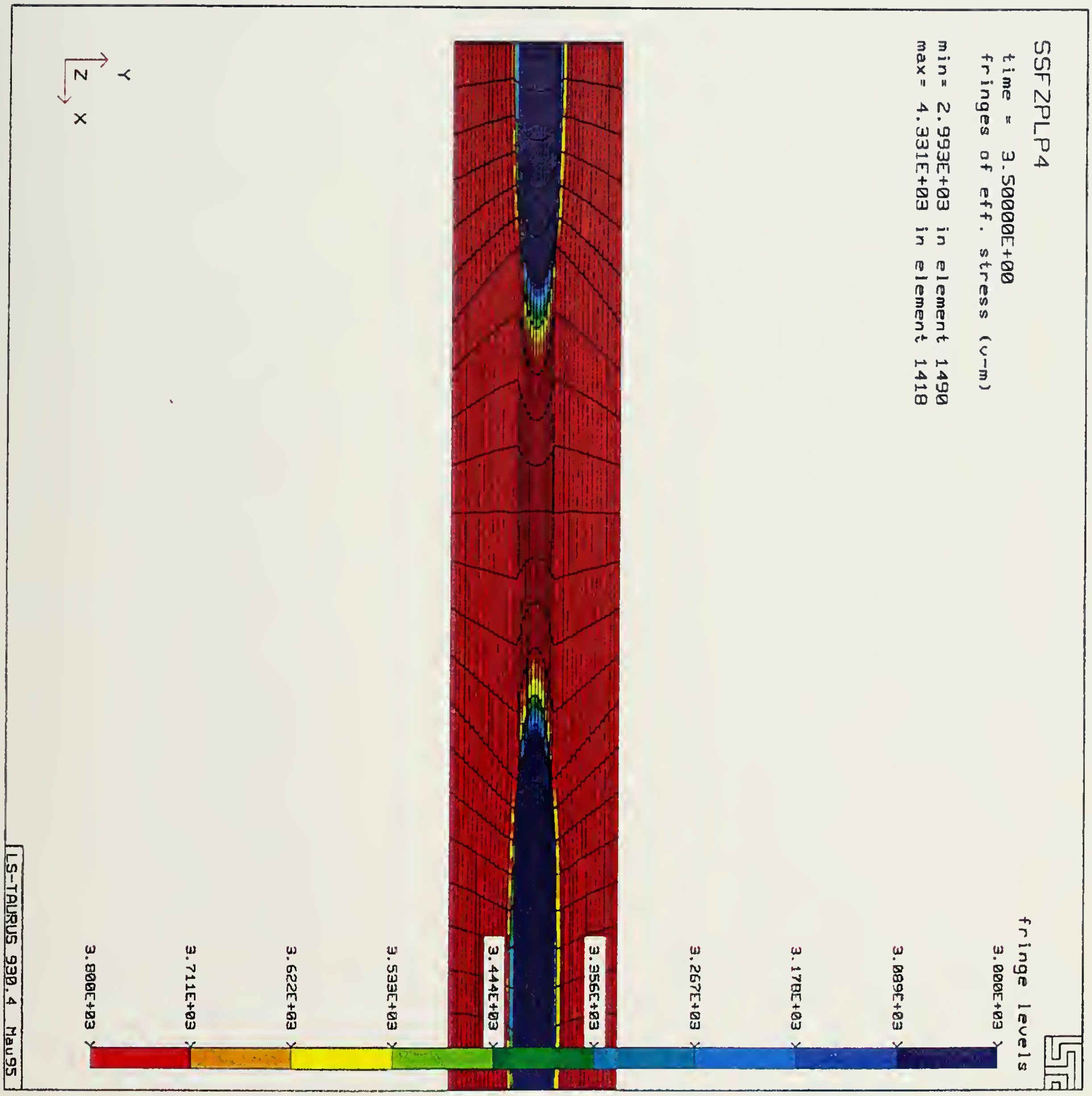

Figure 18: Fringe plot of effective von Mises stress for the two cluster horizontal model after hot working at a low strain rate to a true strain of 1.20.

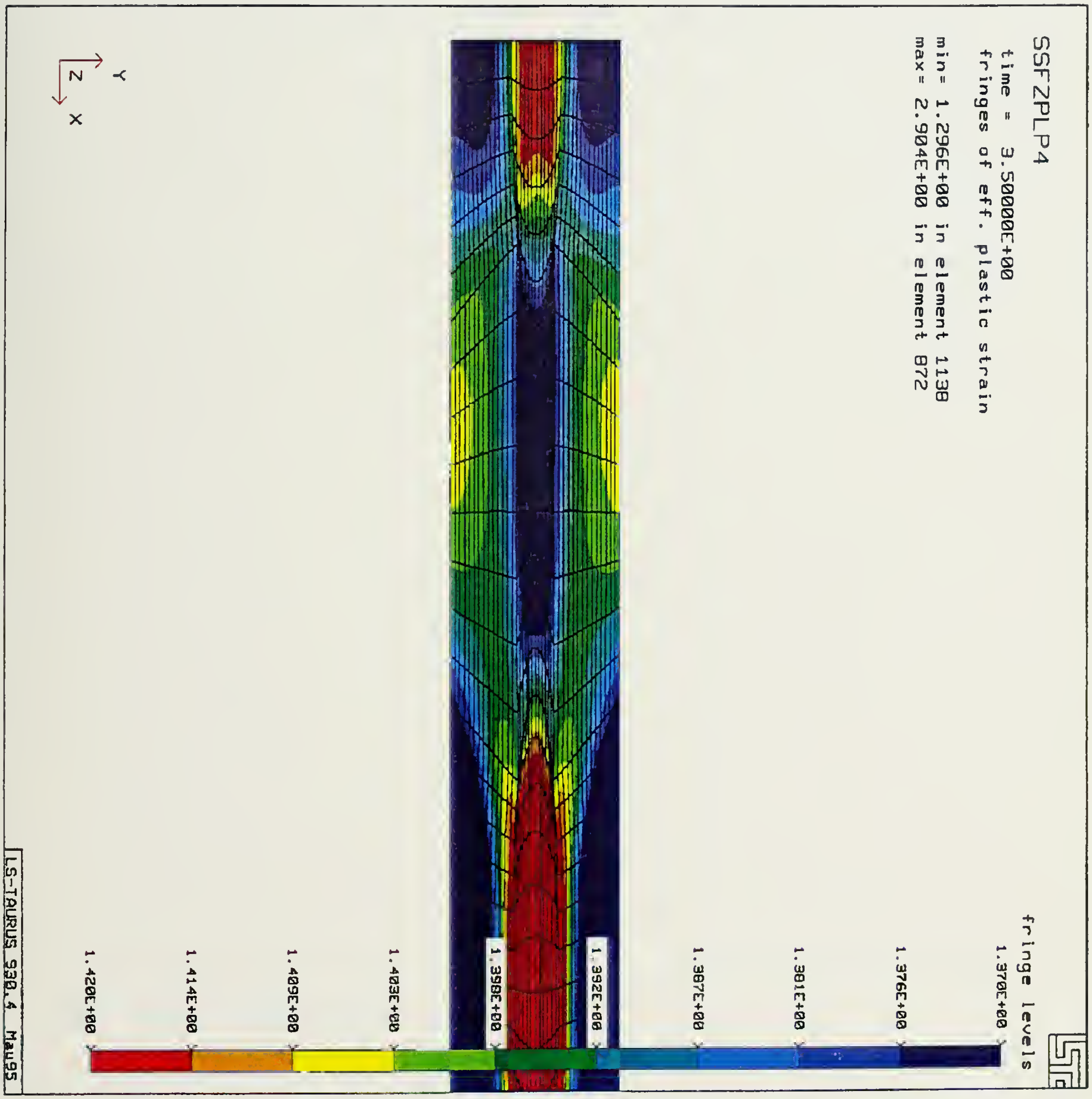

Figure 19: Fringe plot of effective plastic strain for the two cluster horizontal model after hot working at a low strain rate to a true strain of 1.20.

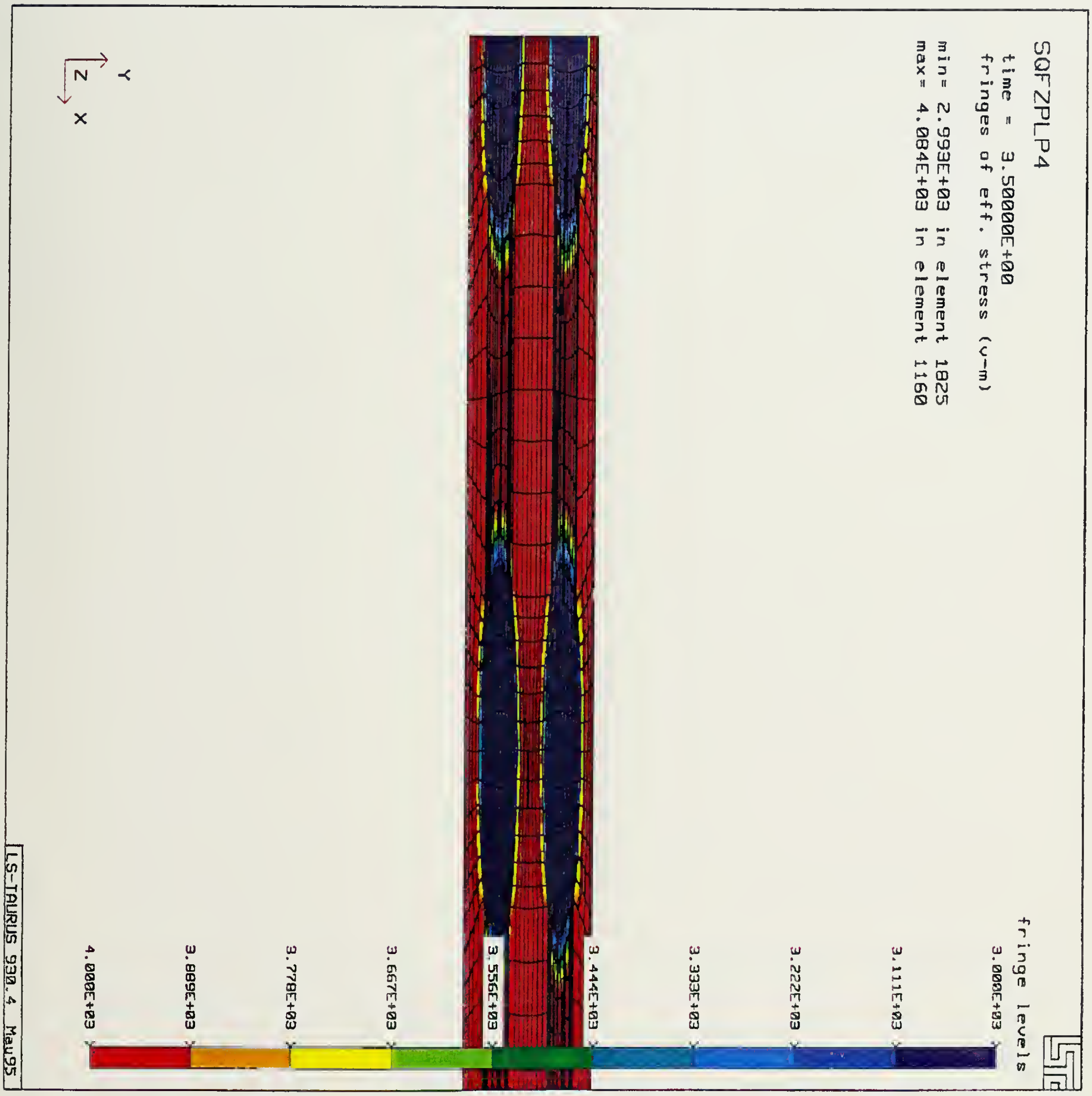

Figure 20: Fringe plot of effective von Mises stress for the square arranged model after hot working at a low strain rate to a true strain of 1.20.

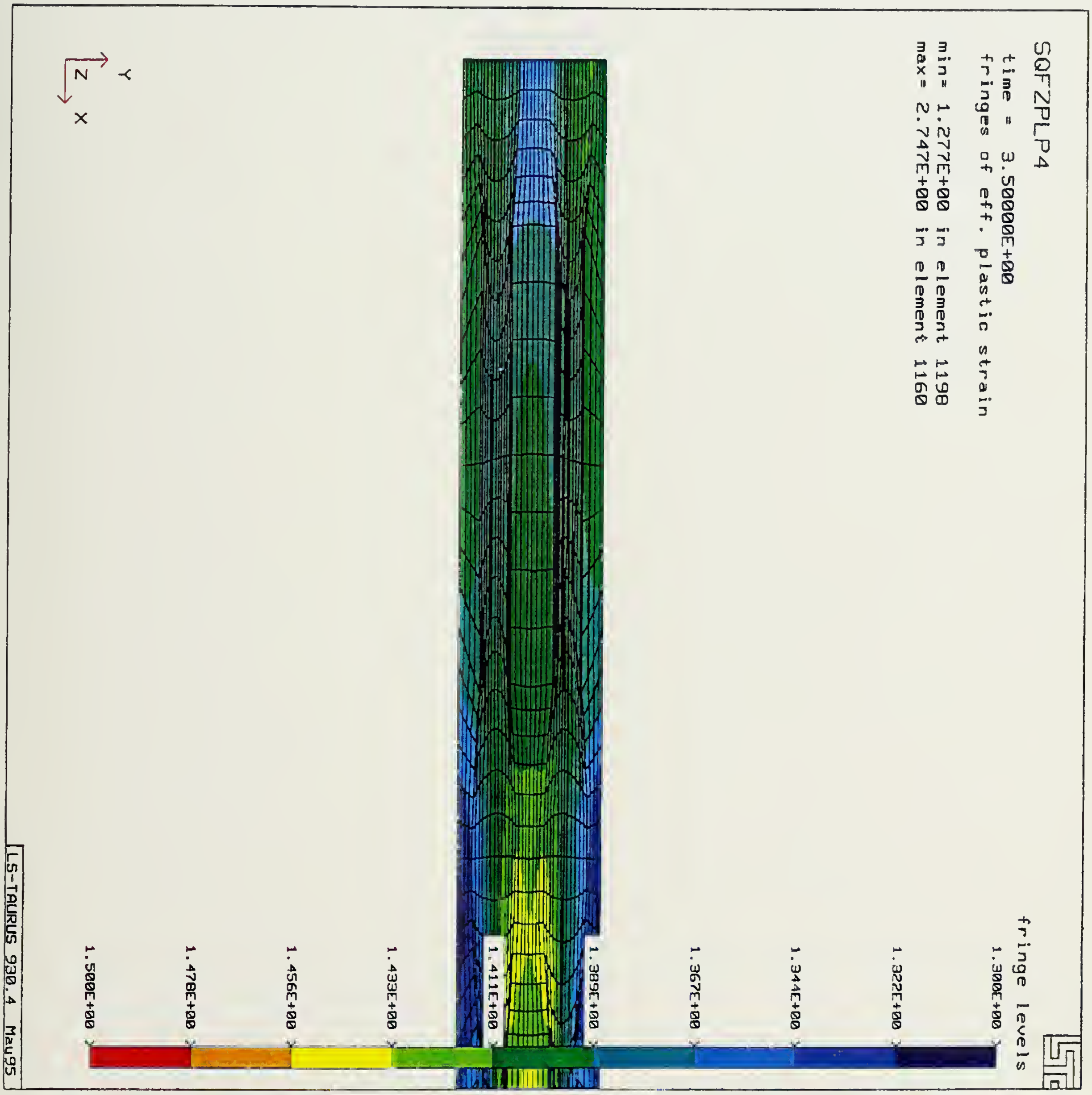

Figure 21: Fringe plot of effective plastic strain for the square arranged model after hot working at a low strain rate to a true strain of 1.20.

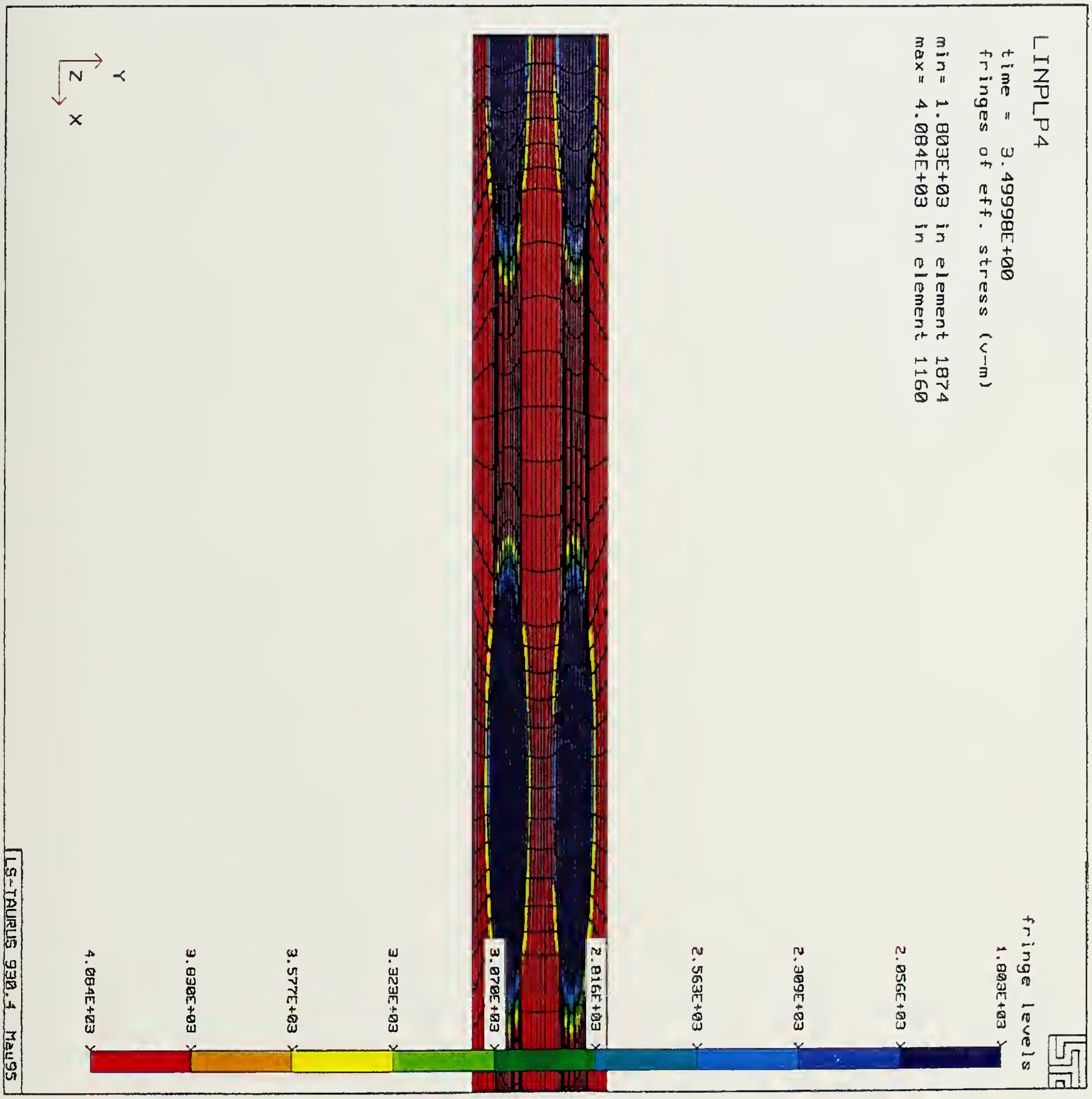

Figure 22: Fringe plot of effective von Mises stress for the square arranged model using the linear law assumption after hot working at a low strain rate to a true strain of 1.20.

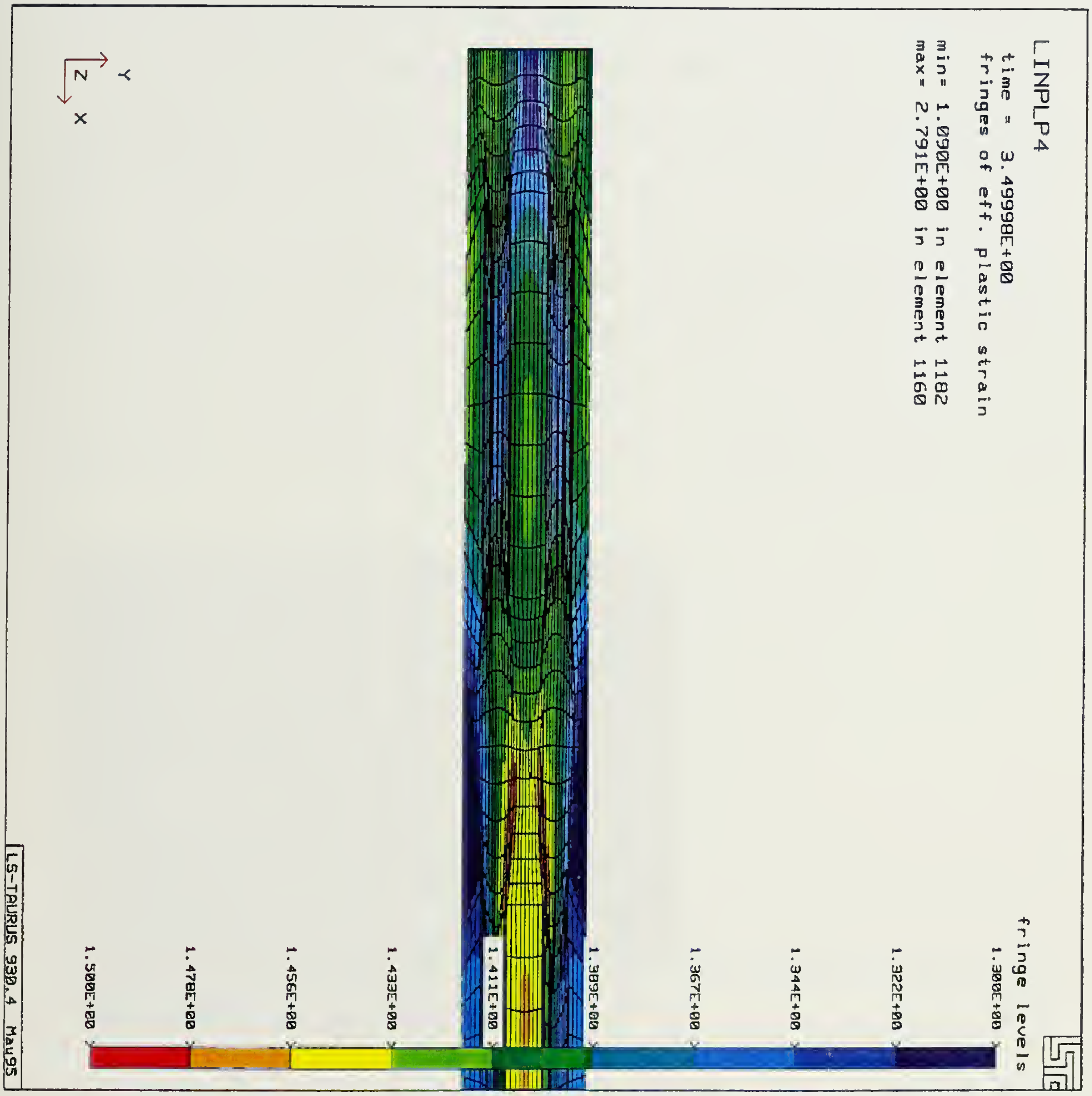

Figure 23: Fringe plot of effective plastic strain for the square arranged model using the linear law assumption after hot working at a low strain rate to a true strain of 1.20.

F. COMPARISON OF DEFORMATION DURING HOT WORKING AND COLD WORKING

Prior to discussing the results of the FEM analysis it is worthwhile to review microstructural analysis (McNelley, T. R. and Ballou, M. A., 1995) illustrating the different effects of cold working compared to hot working. In Figure 24 a non-uniform particle distribution is evident. Particle clusters and a region free of particles are seen in the as-cast 6061 AL-10 vol. pct. AL_2O_3 MMC. Figure 25 shows the same material after hot working to a true strain of 1.10. At this point a relatively homogeneous distribution of the particles throughout the matrix material has been achieved. Figure 26 shows the same material after hot working to a true strain of 0.51, followed subsequently by cold deformation to attain a total true strain of 1.20. Although the particles are better

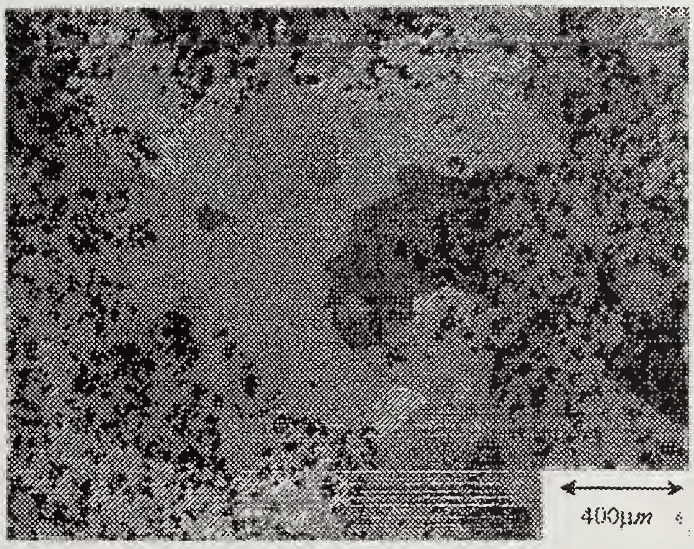

Figure 24: An optical micrograph of an as cast 6061 Al - 10 vol. pct. Al_2O_3 illustrating a non uniform particle distribution (McNelley, T.R. and Ballou, M. A., 1995).

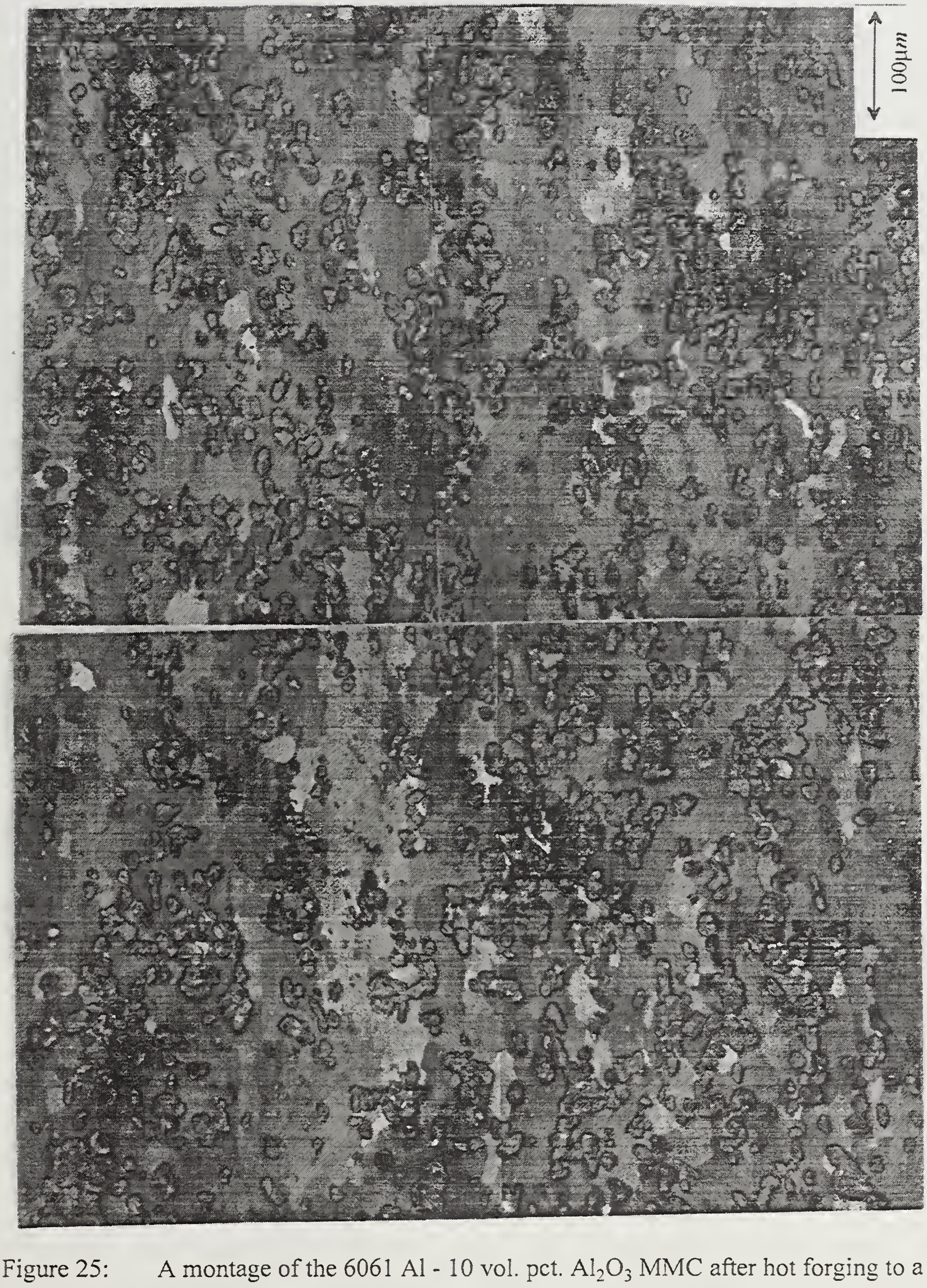

Figure 25: A montage of the 6061 Al - 10 vol. pct. Al_2O_3 MMC after hot forging to a true strain of 1.10 (McNelley, T.R. and Ballou, M. A., 1995).

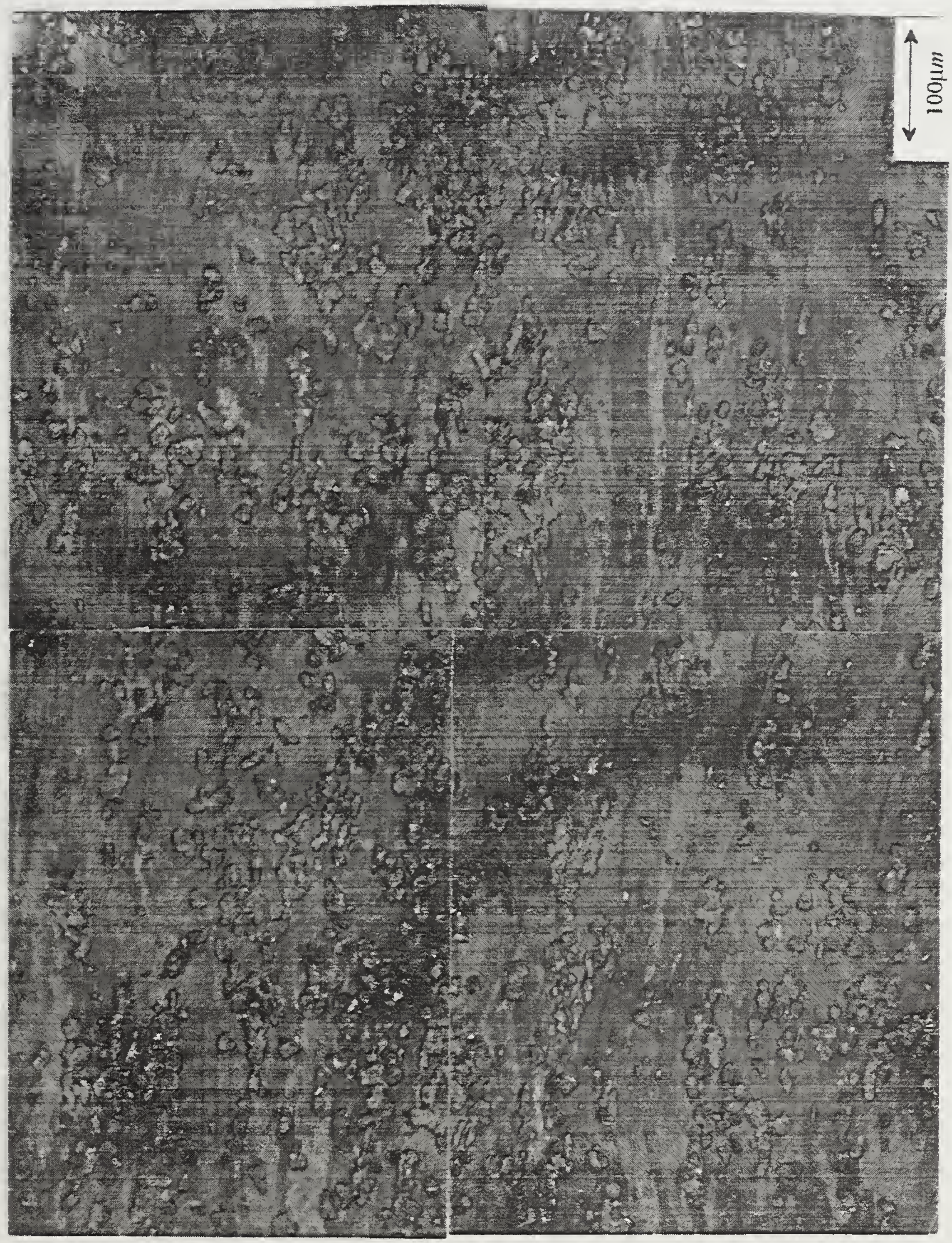

Figure 26: A montage of the 6061 Al - 10 vol. pct. Al_2O_3 MMC after hot forging to a true strain of 0.51 followed by addition cold deformation to a total strain of 1.20 (McNelley, T.R. and Ballou, M. A., 1995).

dispersed, compared to the as-cast material, they are still not as homogeneously distributed as the particles in Figure 25; instead, elongated stringers of particles are seen, representing the residual influence of clustering in the as-cast material.

From such microstructural data McNelley and Ballou (1995) concluded that particles were more effectively redistributed during hot deformation when compared to deformation at lower temperatures. It was also suggested that recrystallization, i.e. the formation of new, strain-free grains, maybe responsible for this effective particle redistribution. This phenomenon is evident in Figure 25, where refined grains are seen throughout; within clusters, such grains appear relatively refined in size.

In this attempt to simulate the effect of such microstructural refinement, the method used for determining the differences in particle to redistribute was to examine the cluster deformation by evaluating the height-to-width ratio prior to and after deformation, the amount of vertical compression of the cluster material in relation to the matrix material, and the horizontal displacement of the cluster centers during the deformation process. If the cluster is more readily deformed and more easily moved about within the matrix then it is likely that the particle distribution can also more readily be homogenized for such conditions.

Prior to deformation, all height-to-width ratios of the cluster regions are 1.0. Figures 27 to 30 show the height-to-width ratios for the clusters after deformation. Each figure applies to one mesh geometry, and the simulations of different TMP conditions differ within each figure. In Figures 27 to 29 the true strain is 1.28, while for Figure 30 the true strain is 1.13. Following is a description of the abbreviations used in Figures 27 to 36:

CW: The cold working process.

HW-high: The hot working process under a high strain rate.

HW-int: The hot working process under an intermediate strain rate.

HW-low: The hot working process under a low strain rate.

HWL-int: The hot working process using the linear law in the cluster material and an intermediate strain rate.

HWL-low: The hot working process using the linear law in the cluster material and a low strain rate.

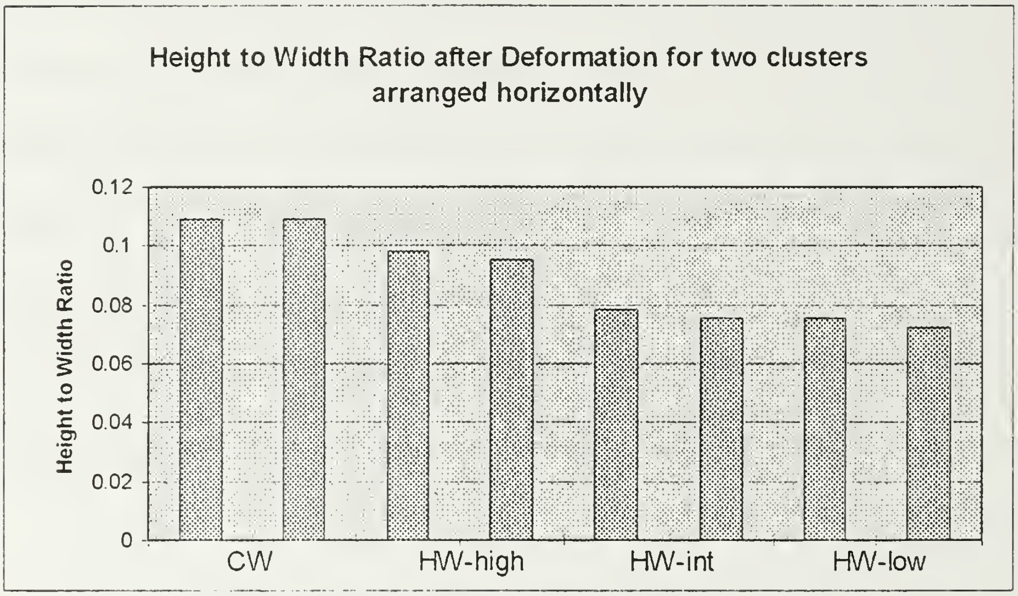

Figure 27: Height to Width ratios for the two clusters arranged horizontally.

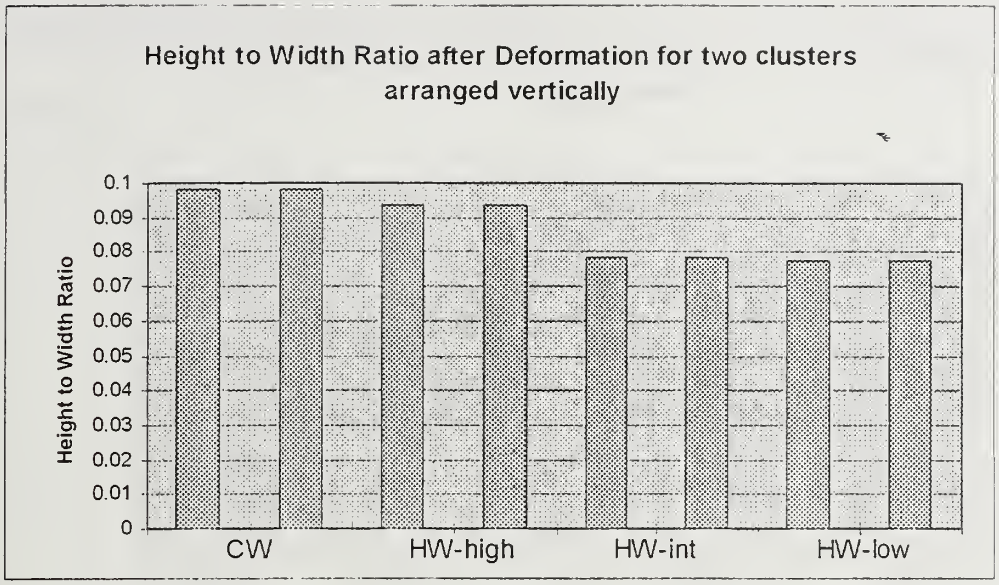

Figure 28: Height to Width ratios for the two clusters arranged vertically.

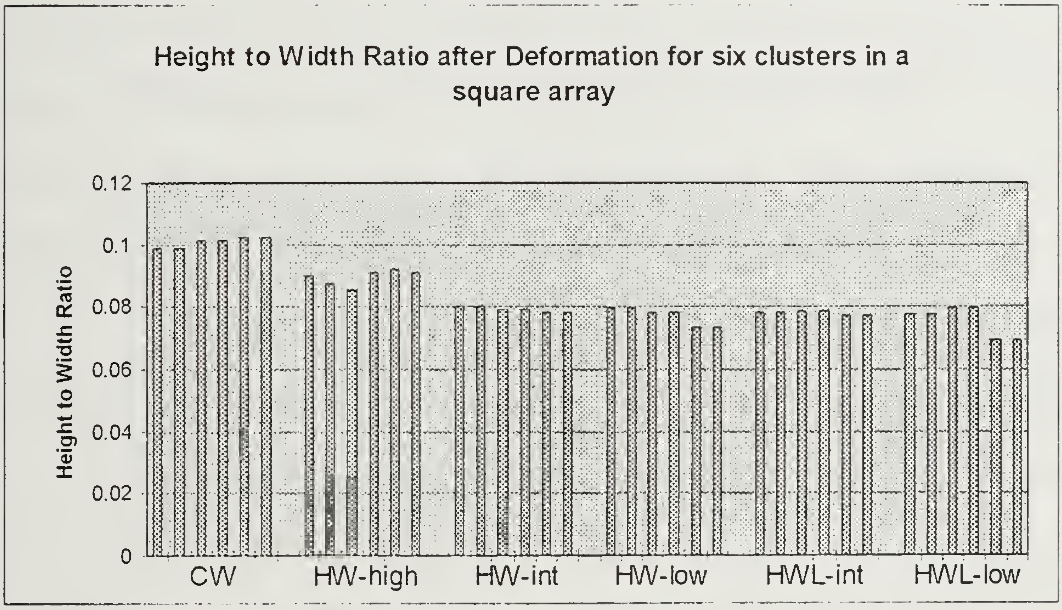

Figure 29: Height to Width ratios for the six clusters in a square array.

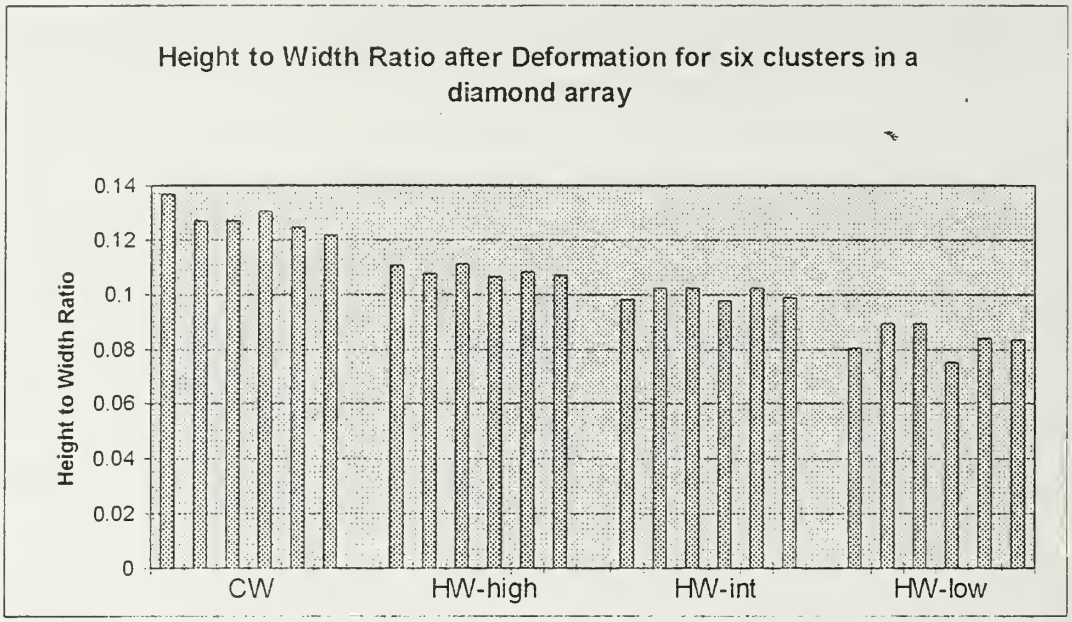

Figure 30: Height to Width ratios for the six clusters in a diamond array.

From Figures 27 to 30 the observation can be made that the ratios are definitely smaller for the hot working processes when compared to the cold working process, i.e., the clusters deform more readily during hot working. This would suggest that the MMC would more readily homogenize during hot working. Also, the ratios are also smaller for the low strain rate vs. the high strain rate analysis. This further suggests that the MMC would more readily homogenize using a low strain rate hot working process.

Next, a close examination of the vertical compression of the cluster region in relation to the matrix material was performed at the centerline of the block. This may provide insight into the relative deformability of the cluster and matrix regions. Two cluster models were used for this analysis: The vertical and horizontal arrangement of two clusters. The analysis are presented in terms of a percentage of cluster material in the vertical direction as compared to the height of the model. The results follow in Figure 31 and 32.

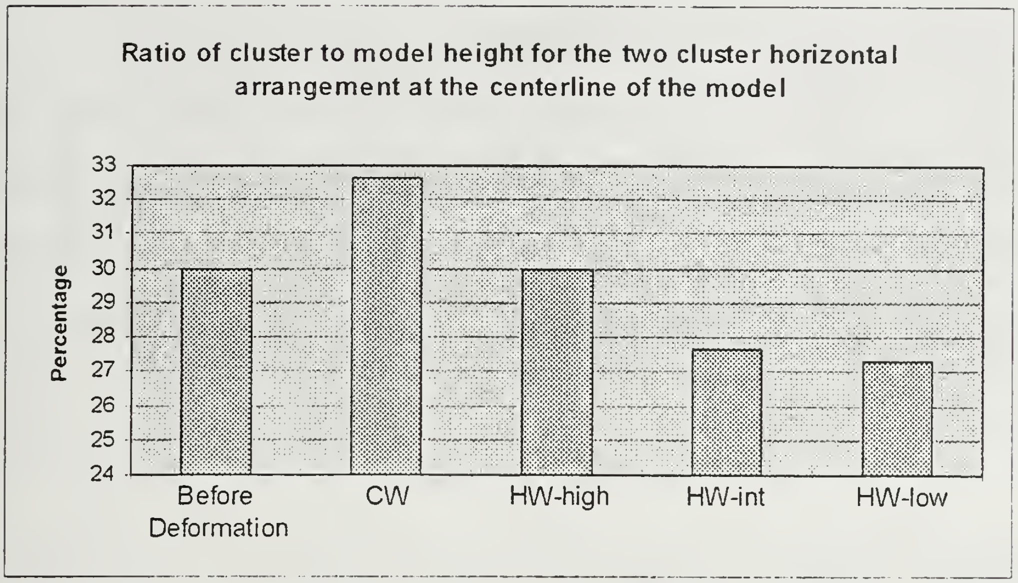

Figure 31: Ratio of cluster to model height at the cluster centers for the two cluster horizontal arrangement at a true strain of 1.28.

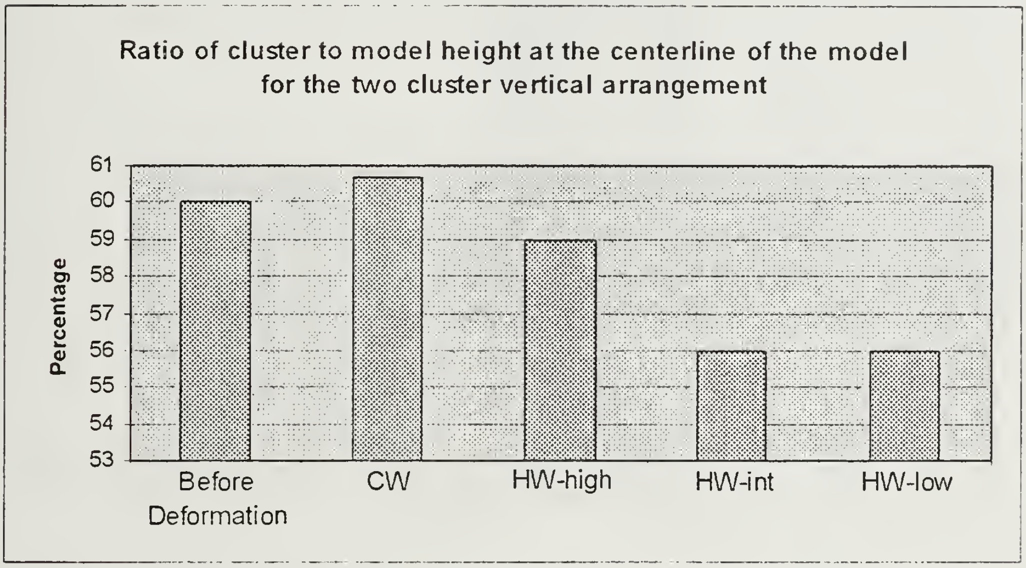

Figure 32: Ratio of cluster to model height at the cluster centers for the two cluster vertical arrangement at a true strain of 1.28.

Once again it can be seen from Figure 31 and 32 that the cluster is more readily deformed in the hot models vs. the cold model. Again this suggests that the MMC would more readily homogenize during the hot working process.

Now, the displacement of the cluster centers in the horizontal direction is compared in Figures 33 to 35. In Figures 33 and 34 true strain is 1.28, and for Figure 35 true strain is 1.13. The two cluster vertical arrangement is not shown since no horizontal displacement of the cluster center is allowed due to the symmetry boundary condition.

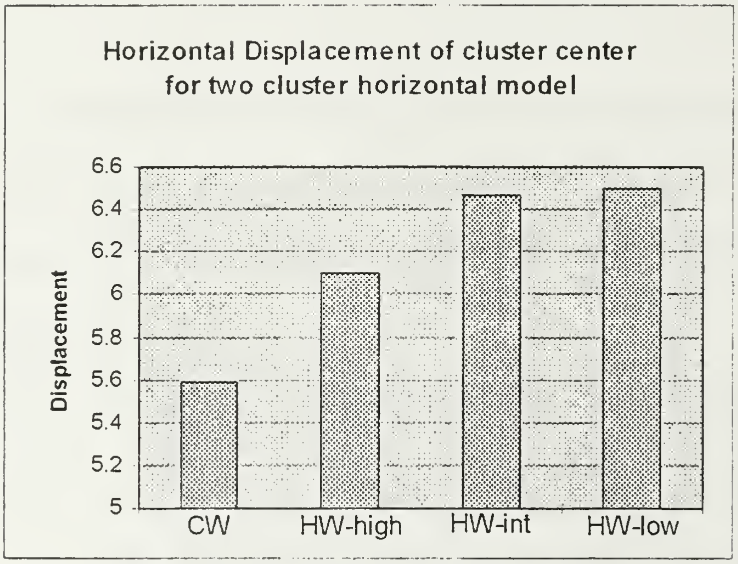

Figure 33: Horizontal displacement of the cluster center for the two-cluster horizontal arrangement at a true strain of 1.28.

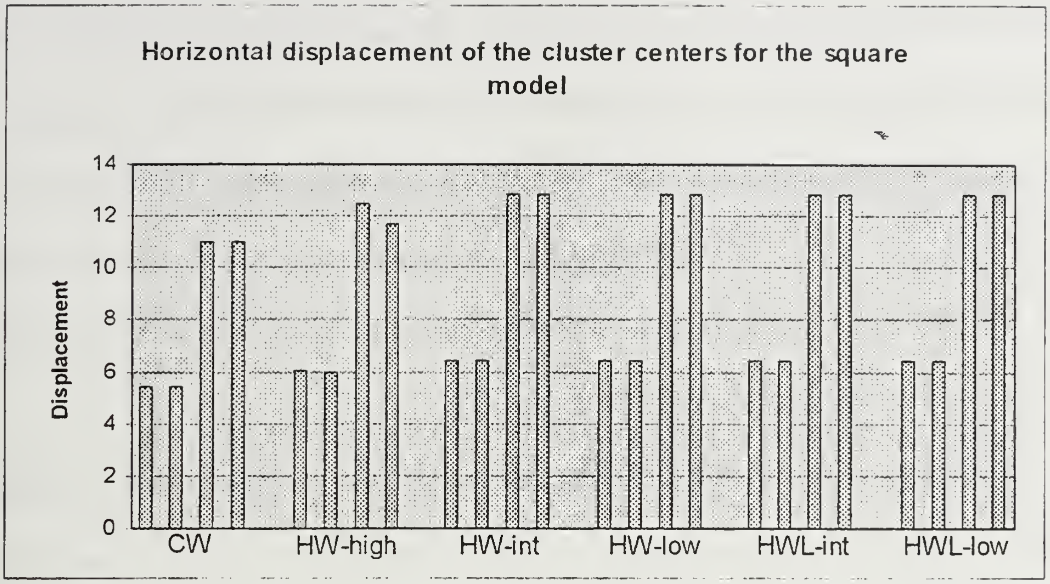

Figure 34: Horizontal displacement of the cluster centers for the square arrangement at a true strain of 1.28.

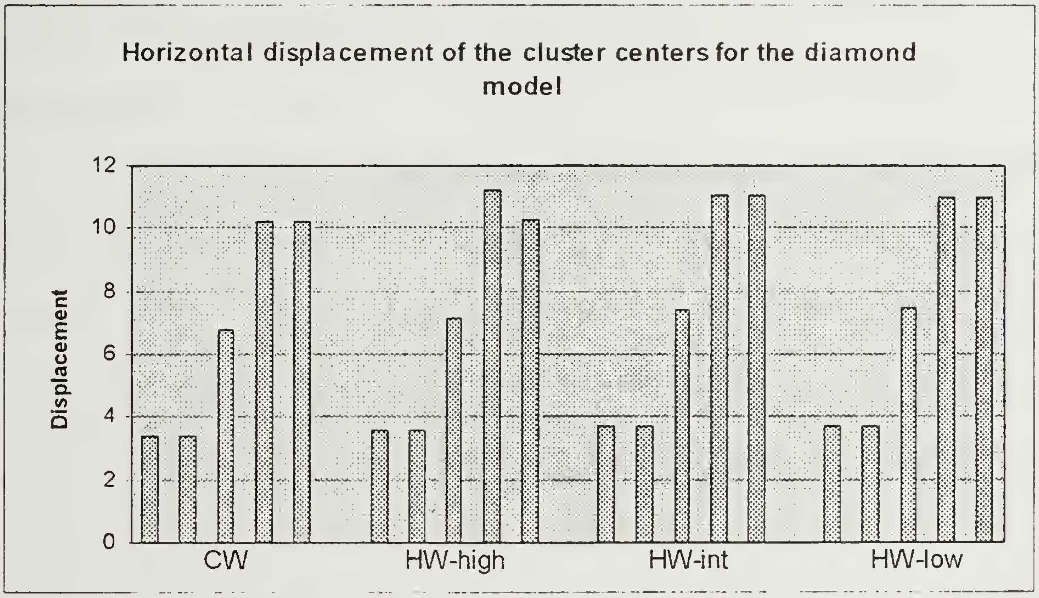

Figure 35: Horizontal displacement of the cluster centers for the diamond model at a true strain of 1.13.

In Figure 34 data for only four clusters are shown. This is because the two clusters at the left of the square model have no displacement in the horizontal direction. Figure 35 displays data for five clusters in the diamond array for the same reason. It can be seen in Figures 33 to 35 that the horizontal displacement is, once again, greater in the hot worked models and this again leads to the conclusion that the MMC would more readily homogenize during the hot working process.

All of the previously displayed results also indicate that the deformation associated with clusters increases as the strain rate is lowered during the hot worked process. There are significant difference between the high strain rate and the intermediate strain rate cases, while the differences between the intermediate and low strain rate models is evident but smaller. The conclusion is then made, based on the assumptions of this work, that the best TMP to follow to reach a homogeneous particle distribution in the least strain is a relatively low strain rate during a hot working process. A summary of all the results is illustrated in Figure 36 for the two-cluster horizontal array.

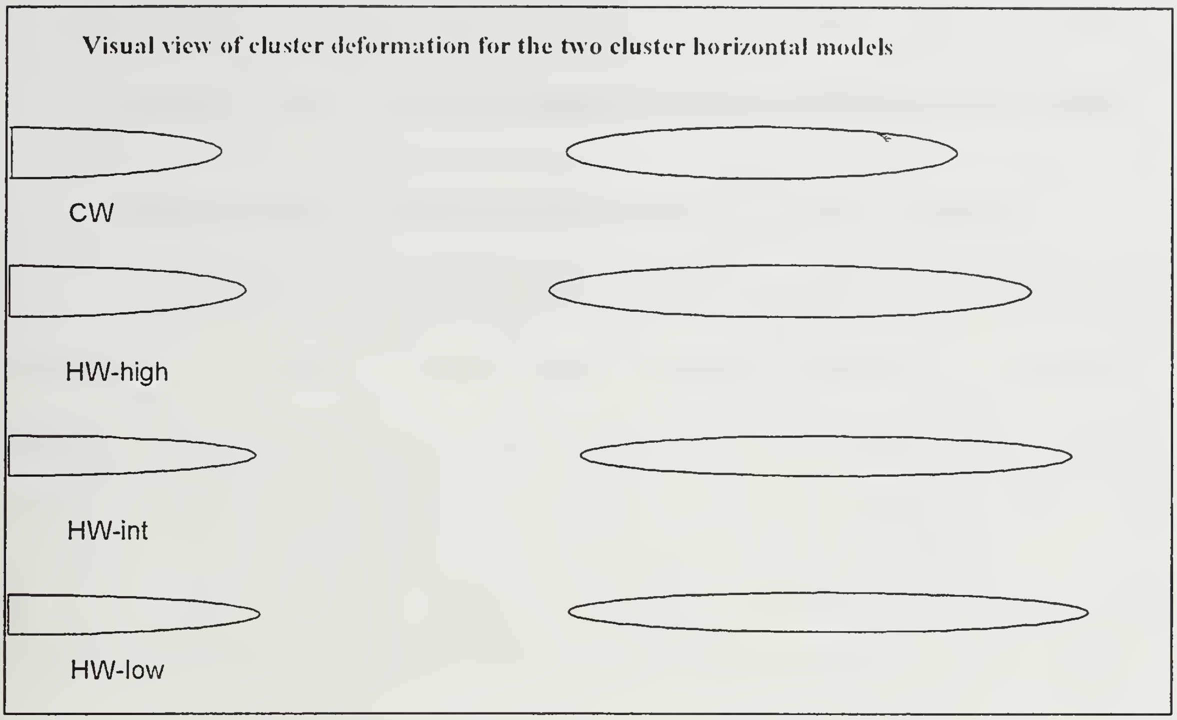

Figure 36: Visual view of the cluster deformation after hot and cold working to a true strain of 1.28 in the two cluster horizontal models.

One area of concern in this study was how the free boundary of the mesh affects the horizontal movement of the clusters. To answer this question the six-cluster diamond array mesh was modified by adding a large amount of matrix material to the right hand side of the mesh, thereby extending the mesh in the horizontal direction. This isolated the clusters from the free boundary effects. After deformation the horizontal displacement was compared to that of the diamond array without the mesh extension. It was found that the clusters did not displace at all during the first 0.02 of true strain as compared to the first 0.01 true strain in the non-extended mesh. However, once the clusters began to move, both meshes show the same horizontal displacement of the cluster centers.

Therefore, from a qualitative point of view, the free boundary has no effect on the horizontal displacement or cluster deformation.

IV. DISCRETE PARTICLE MODELS OF METAL MATRIX COMPOSITES

A. DEVELOPMENT OF DISCRETE MODELS AND FEM MESHES

The preceding analyses neglected the particles and assumed the only influence of the particles was on grain size, during elevated temperature deformation. This ignores the effect of the hard particles on stress states and the modulus of the composite. Therefore, individual reinforcement particles were modeled discretely in cluster regions of the mesh as shown in Figures 37 to 41. The particles are still in clusters within the matrix and furthermore arranged in the two-cluster, horizontal mesh arrangement shown in Figure 7.

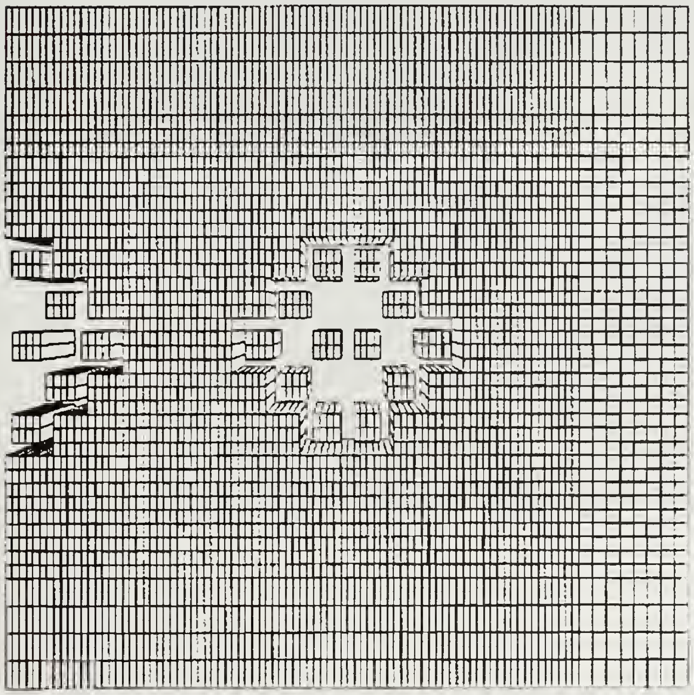

Figure 37: Mesh of individual particles in two cluster regions oriented in a horizontal arrangement. Local particle volume fraction is 25%. The empty space in the mesh is only for visual purposes so that the location of the particles can be see. This space in the model is filled with matrix material in the cold worked models and cluster material in the hot worked models.

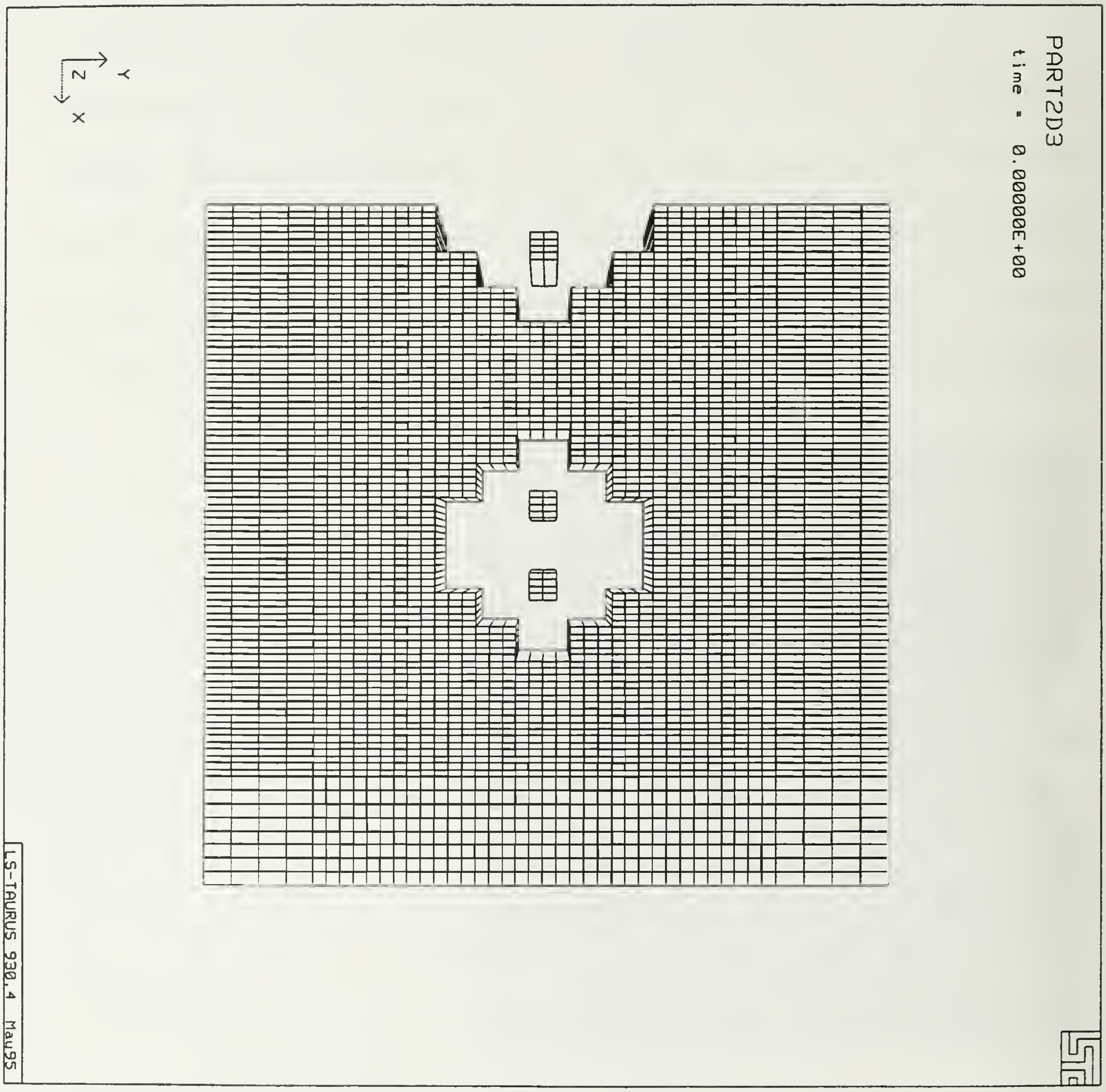

Figure 38: Mesh of discrete model for large particles with a local volume fraction of 4%.

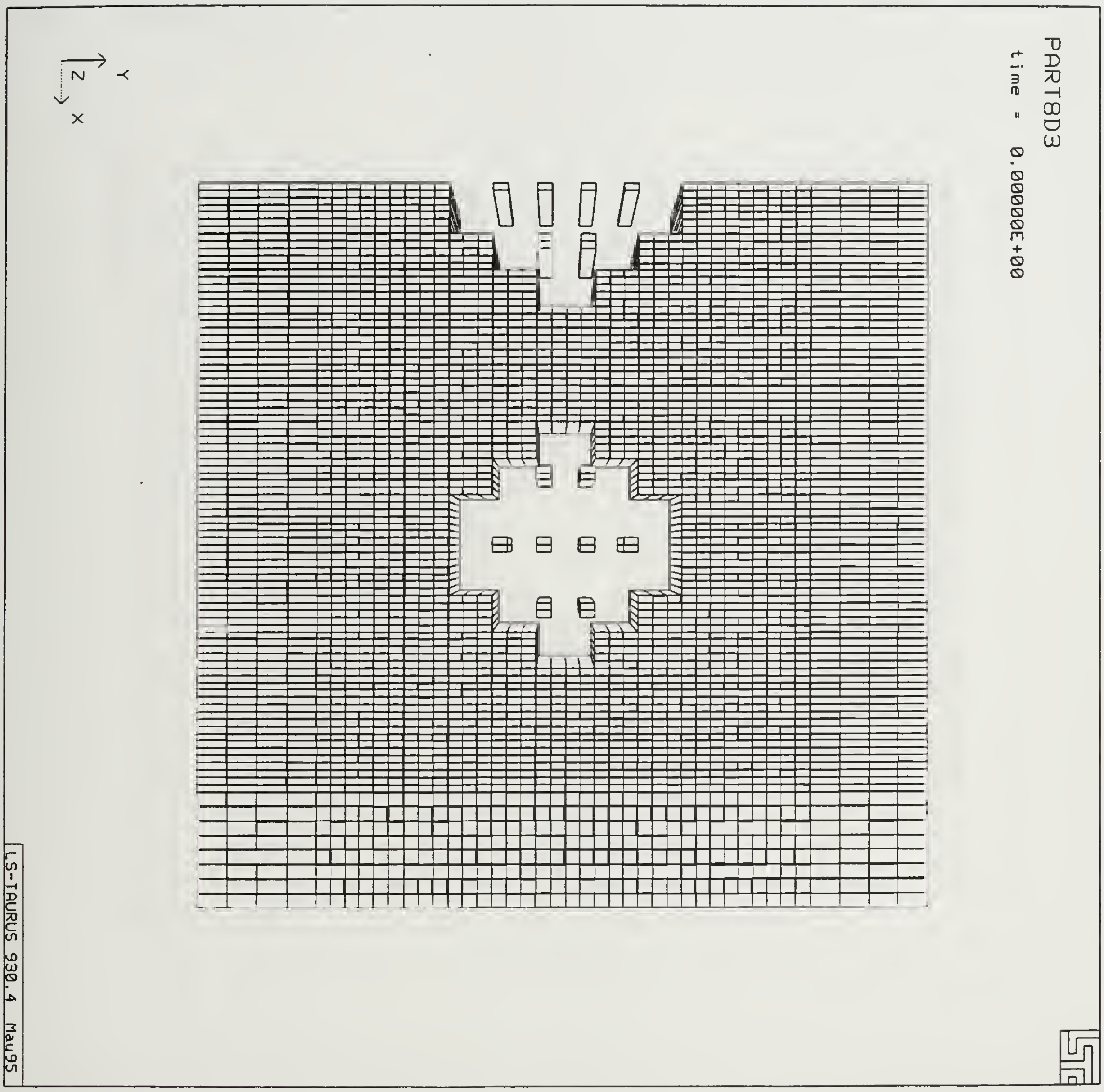

Figure 39: Mesh of discrete model for small particles with a local volume fraction of 4%.

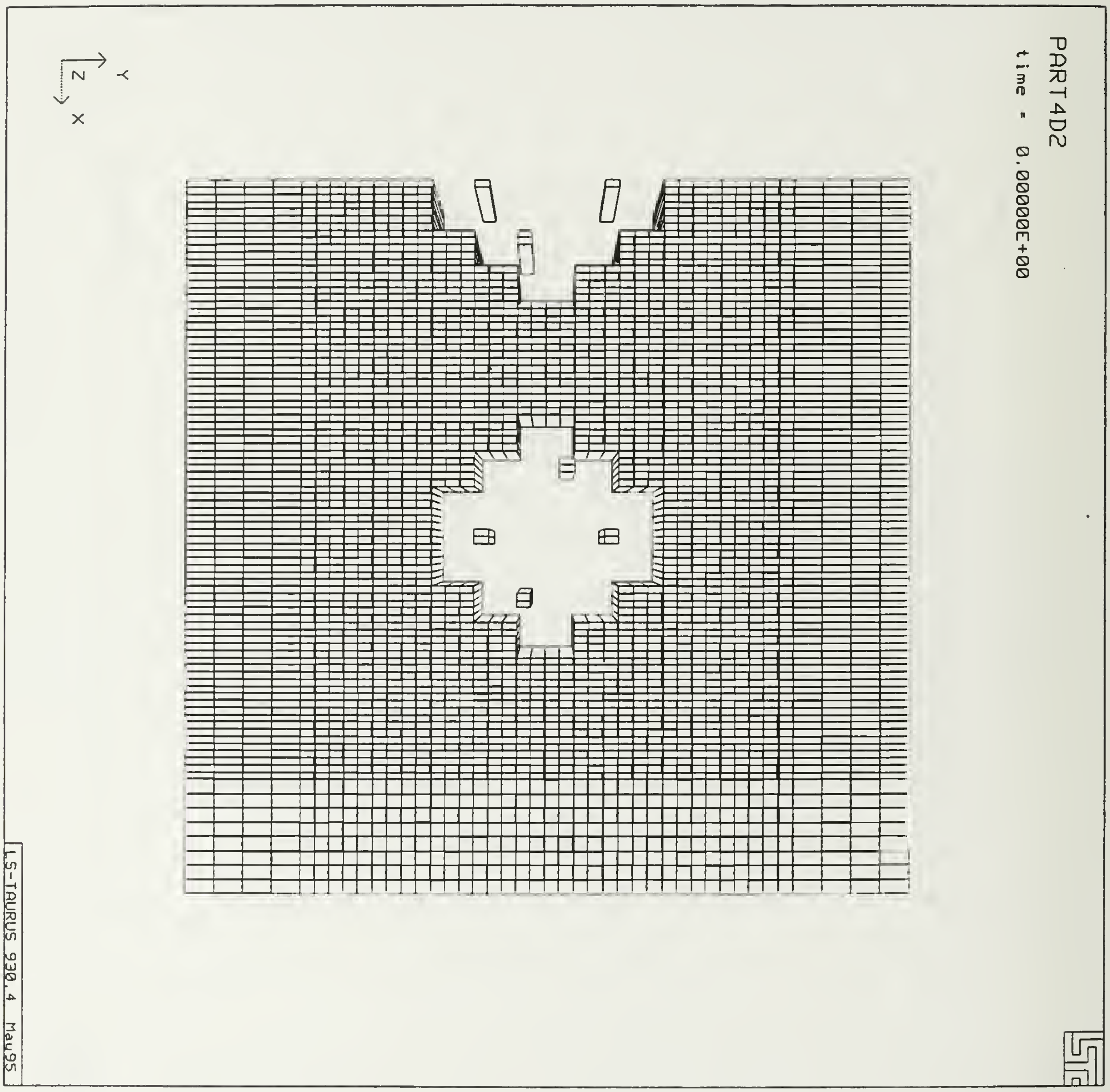

Figure 40: Mesh of discrete model for small particles with a local volume fraction of 2%.

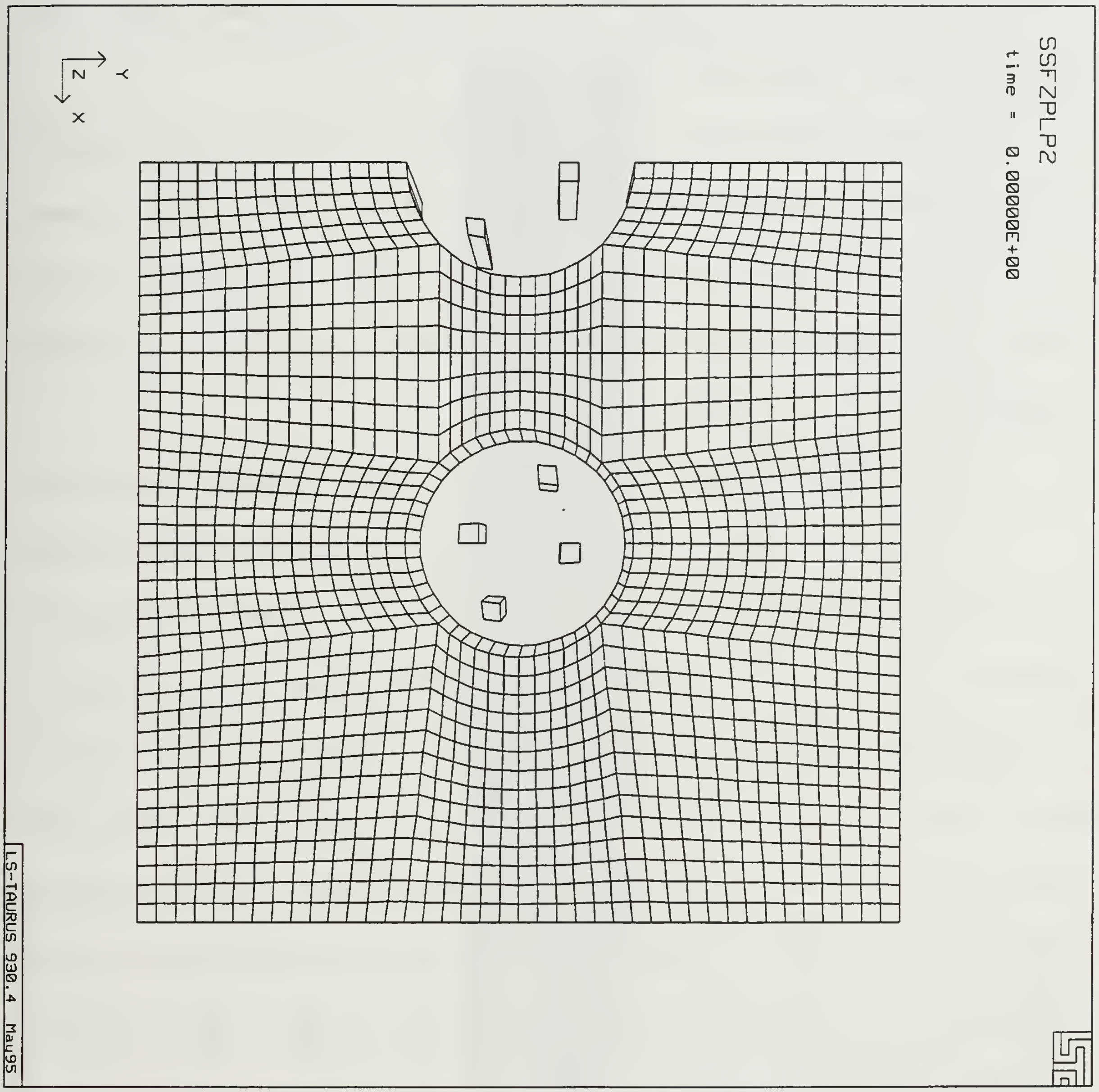

Figure 41: Mesh of discrete model for small particles with a local volume fraction of 2%. Note that this model has circular shaped cluster regions.

The empty space surrounding the particles in Figure 37 is for visualization purposes only. The space in the models is filled in with matrix material in the cold worked models and cluster material properties in the hot worked models. The local volume percentage of particles in Figure 37 is 25%. The particles were modeled as purely elastic material with Young's modulus, E, equal to $60*10^6$ psi.

The local volume fraction and size of reinforcement particles were also varied in the following manner. The reinforcement particle local volume fraction was reduced from 25 % to 4% using the same particle size as shown in Figure 38; the particle size was reduced to one-quarter the size shown in Figure 37 and modeled with a local volume fraction of 4% and 2% (note Figures 39 to 41).

B. STRESS AND STRAIN RESULTS OF THE DISCRETE MODELS

The fringe plots of effective von Mises stress and effective plastic strain are shown in Appendix C. The trend of the results for all discrete models is similar. The discrete particles sustain the highest stresses and the lowest effective strains. Figures 42 and 43, for the 25% particle volume fraction and large particle size, apply to the low strain-rate, hot-work model. The stresses in the particles reach 875 ksi while the stresses in the matrix are as low as 15 ksi. The particles do not deform plastically while the effective plastic strains in the matrix are as high 3.60. The highest strains are found between the particle clusters, and above and below the particle clusters. Figures 44 and 45 show the results of the intermediate strain-rate, hot-work model with a particle size one-quarter that shown in Figures 42 and 43 and a volume loading of 4%. The results are qualitatively similar to those of Figures 42 and 43.

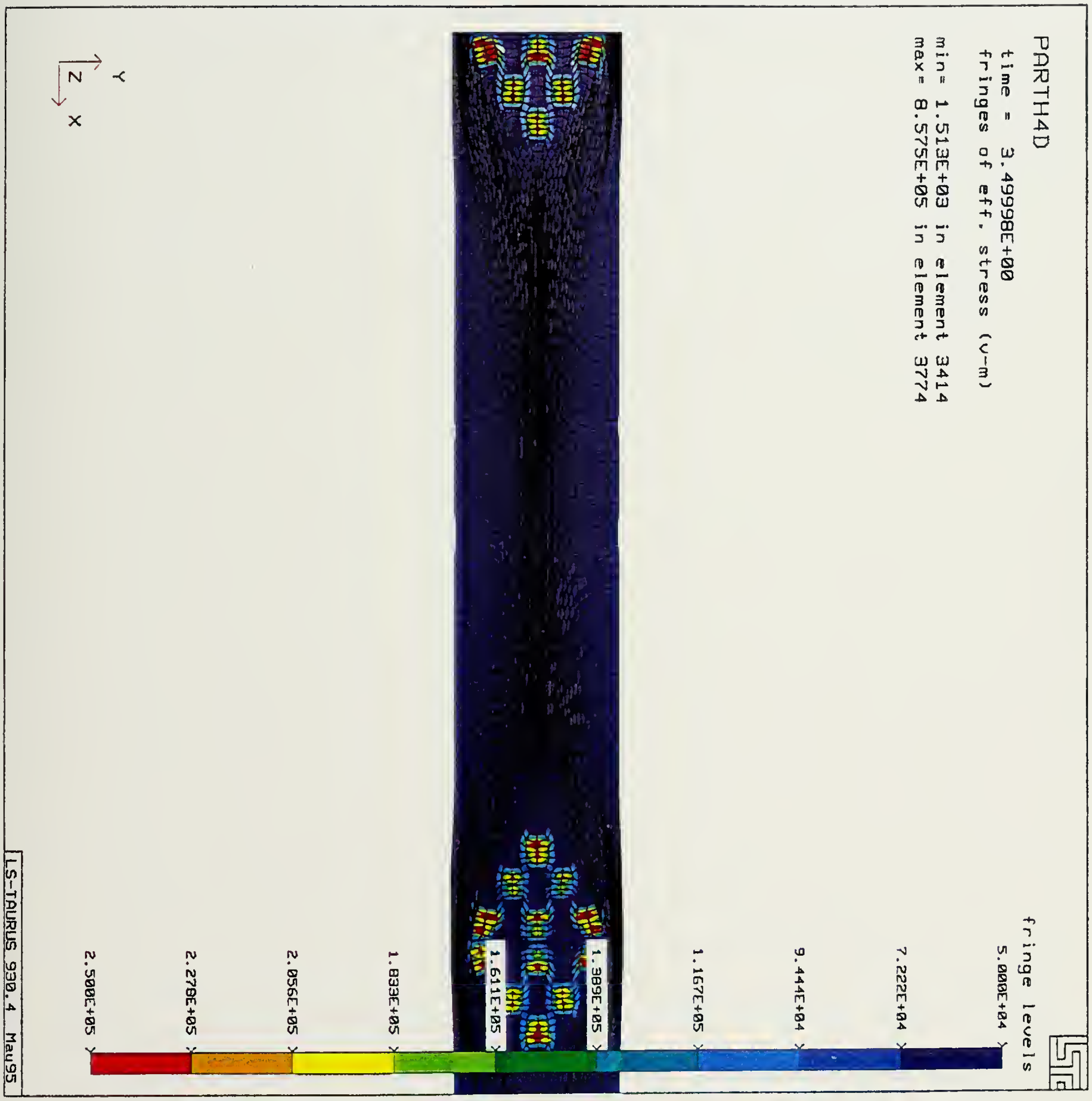

Figure 42: Fringe plot of effective von Mises stress for the discrete model after hot working at a low strain rate to a true strain of 1.20 with local particle volume fraction of 25%.

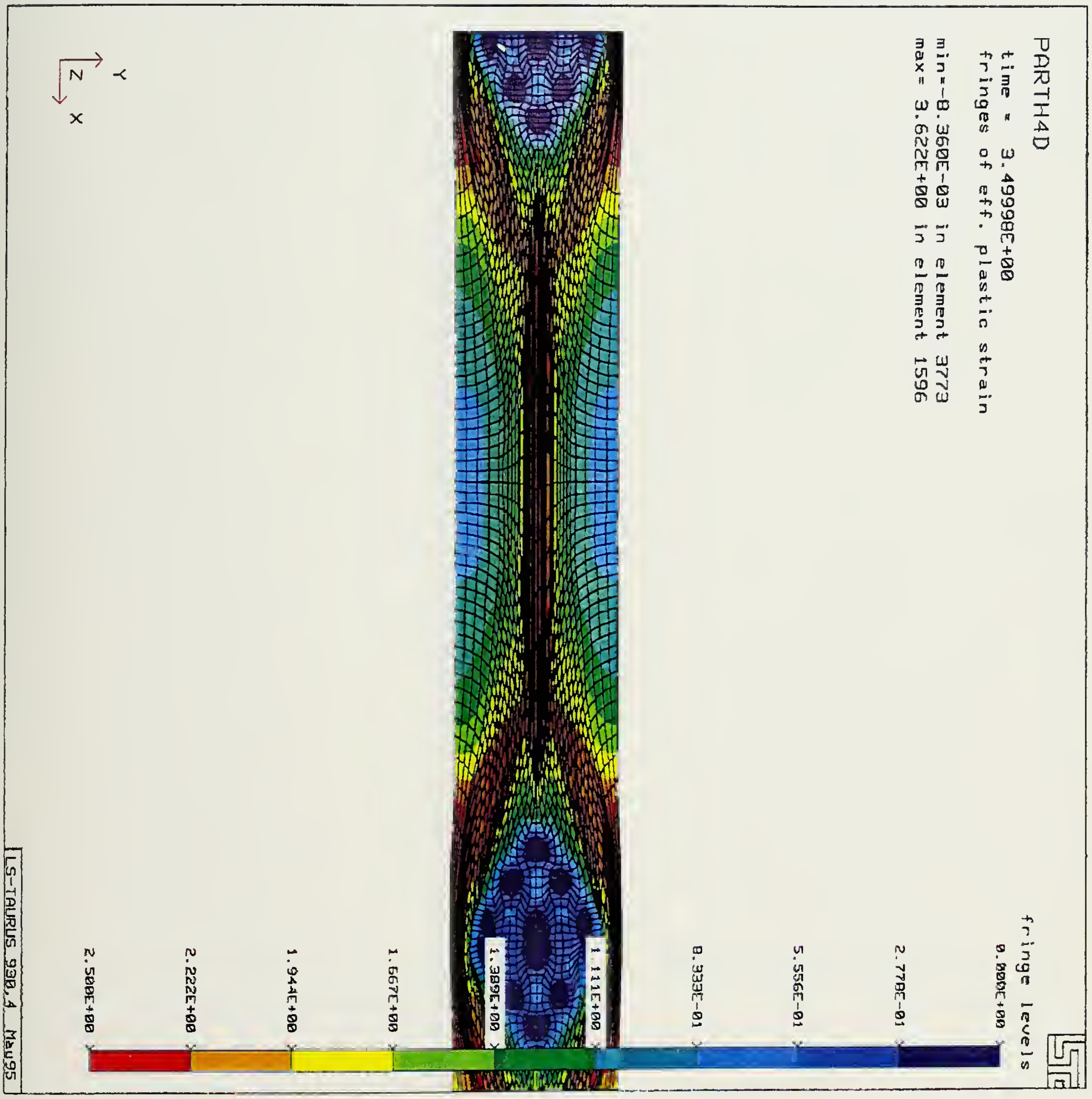

Figure 43: Fringe plot of effective plastic strain for the discrete model after hot working at a low strain rate to a true strain of 1.20 with local particle volume fraction of 25%.

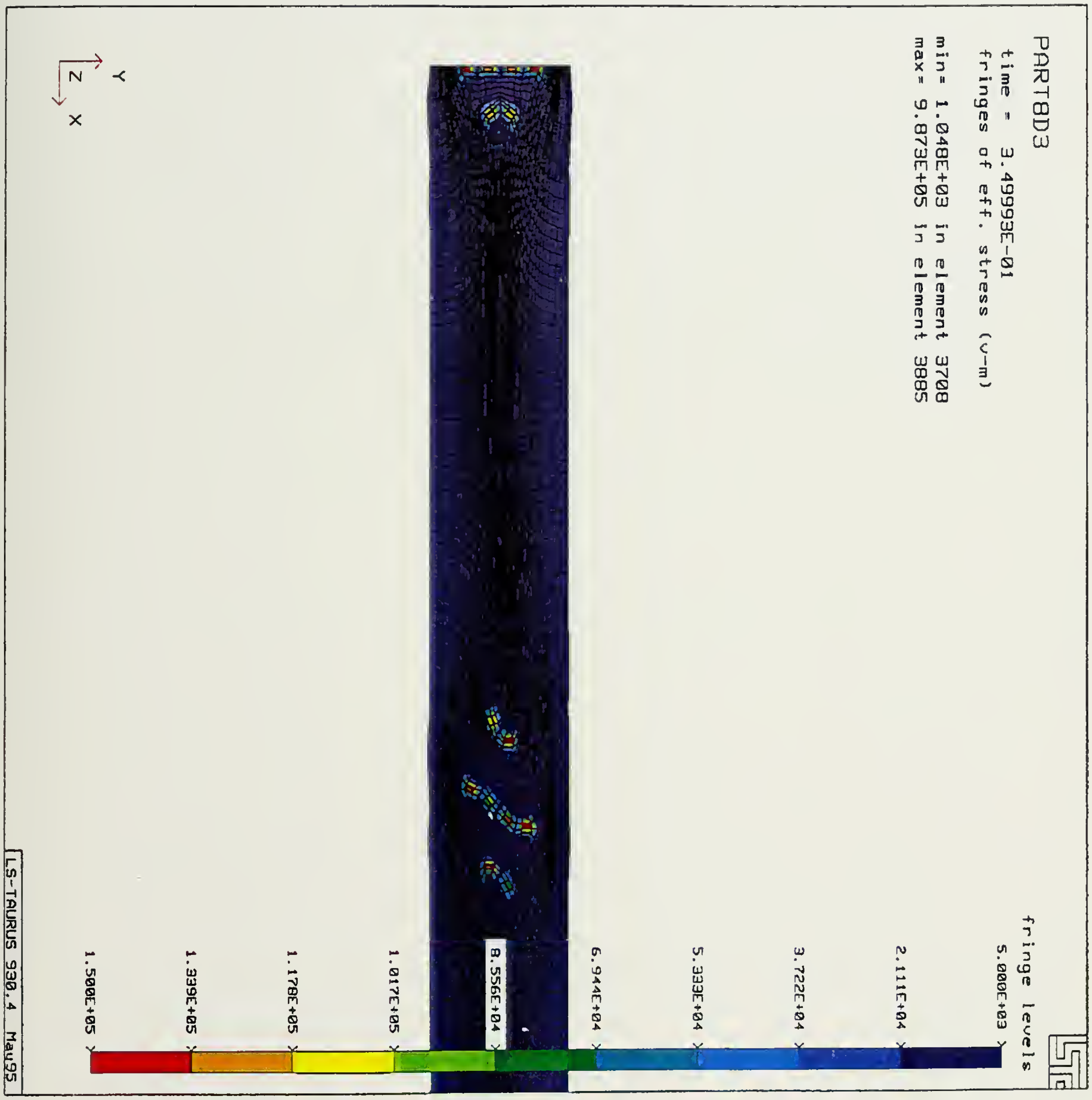

Figure 44: Fringe plot of effective von Mises stress for the discrete model after hot working at an intermediate strain rate to a true strain of 1.20 with local particle volume fraction of 4%.

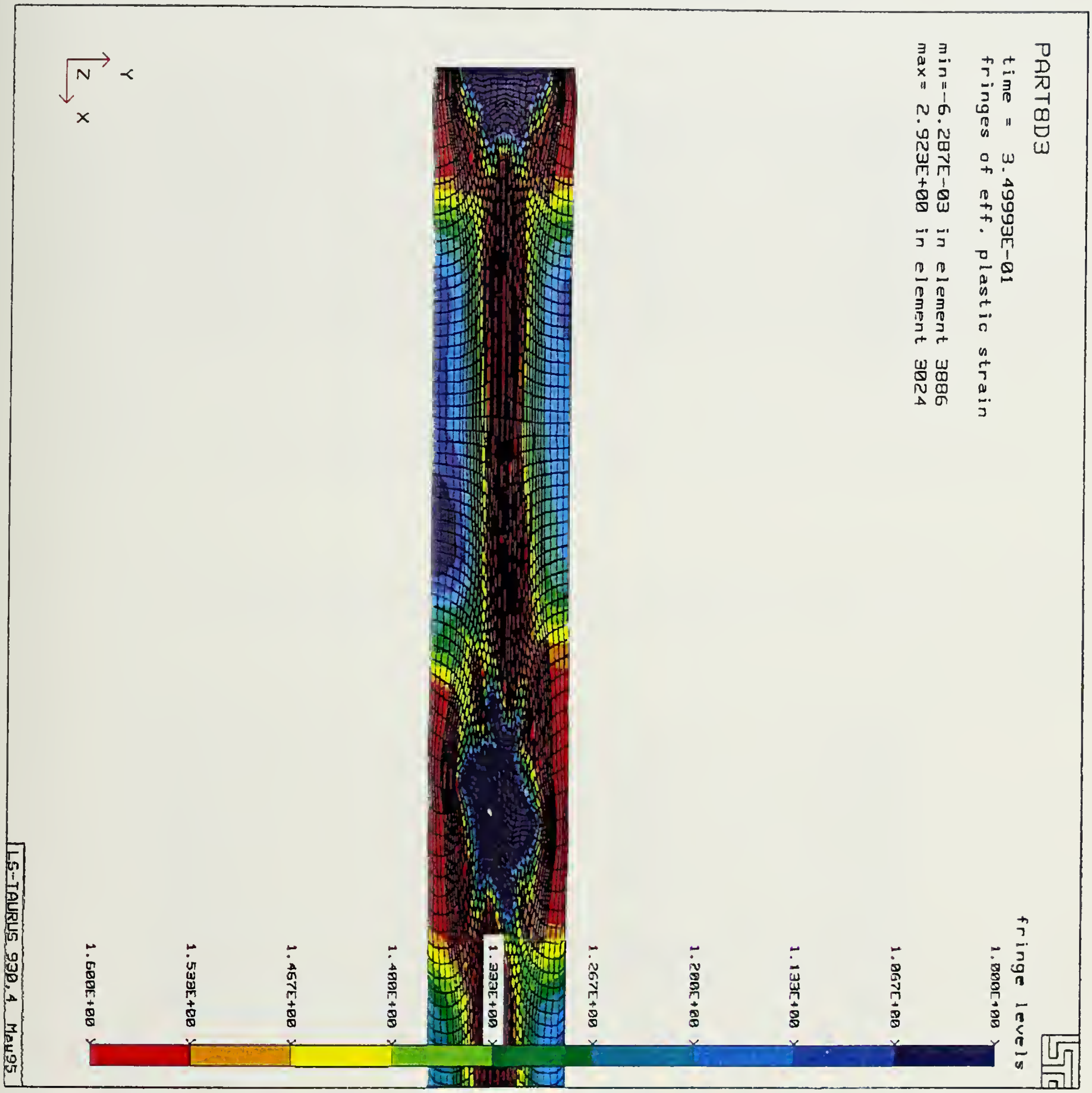

Figure 45: Fringe plot of effective plastic strain for the discrete model after hot working at an intermediate strain rate to a true strain of 1.20 with local particle volume fraction of 4%.

The horizontal displacement of the center of particles was measured for the different methods of TMP. These are shown in Figure 46 for the large particle size and 25 volume pct., and in Figure 47 for the small particle size and 2 volume pct.

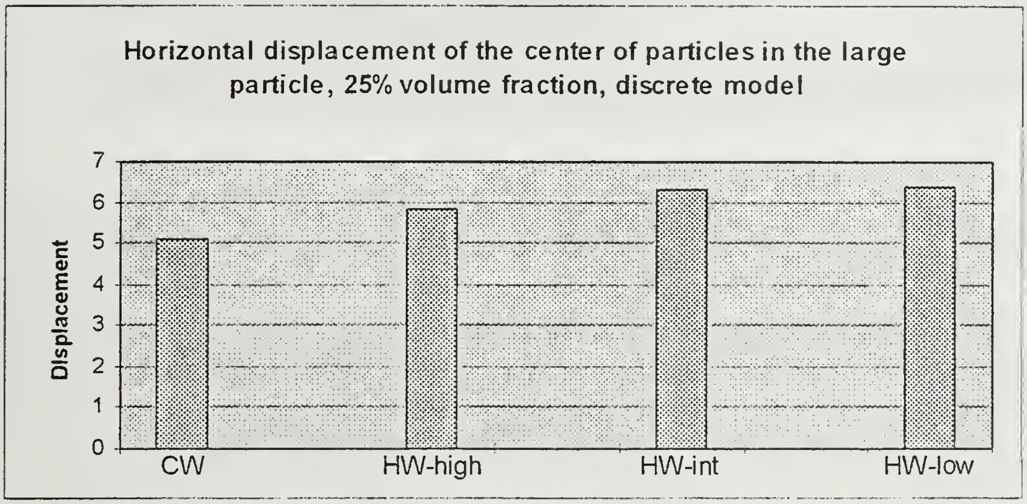

Figure 46: Horizontal displacement of the center of particles for the large particle, 25% volume fraction, discrete model.

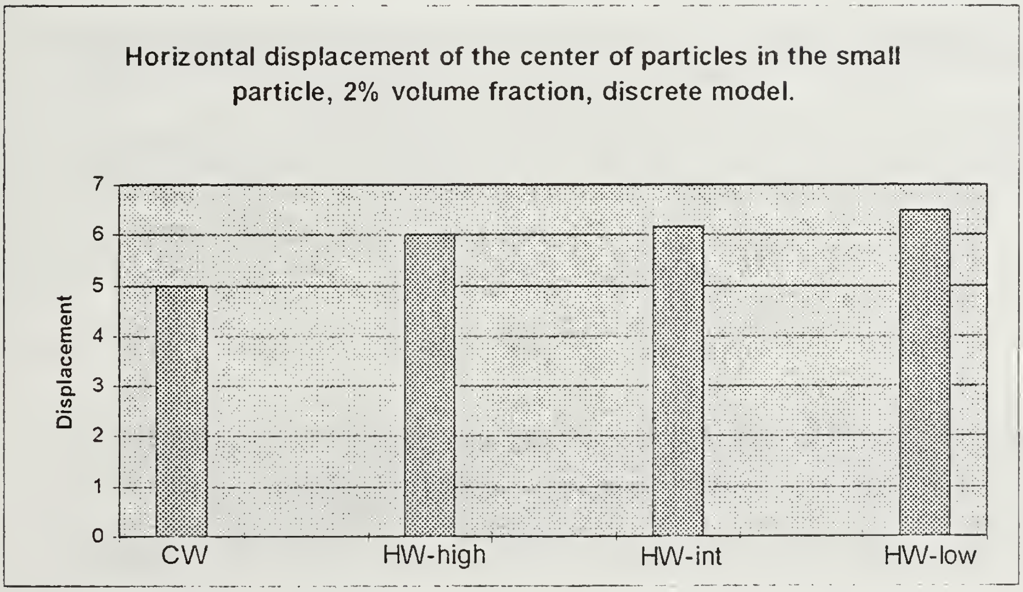

Figure 47: Horizontal displacement of the center of particles for the small particle, 2% volume fraction, discrete model.

Figure 48 shows the height-to-width ratios, after the different methods of TMP, of the cluster regions shown in Figure 41.

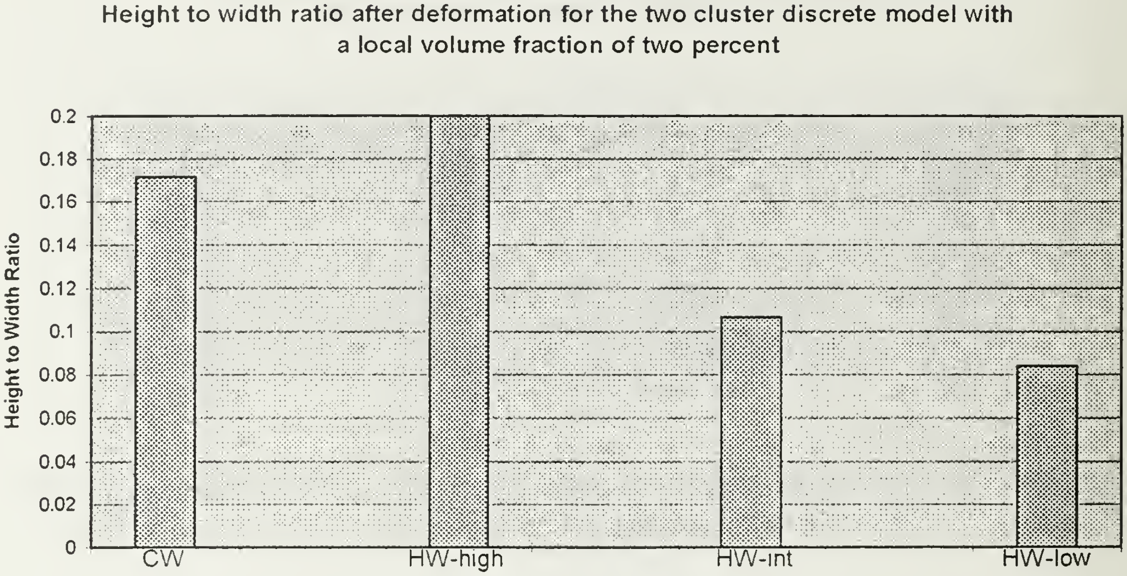

Figure 48: Height to width ratio after deformation of the small particle, 2% volume fraction, discrete model.

Again, Figures 46 to 48 support the observation that the particles will move more readily using a hot vs. cold TMP. Figure 49 depicts a visual view of the cluster region deformation and particle movement for the small particle, 2% local volume fraction discrete model under different TMP methods.

C. COMPARISON OF THE SMEARED VS. DISCRETE MODELS

The smeared and discrete models do not respond in the same manner. First, the cluster zones have slightly different shapes in both models: the smeared model used a circular shaped cluster zone while the discrete model used a straight line approximation

Visual view of cluster deformation in the small particle, 2% local volume fraction discrete model after different methods of TMP to a true strain of 1.20.

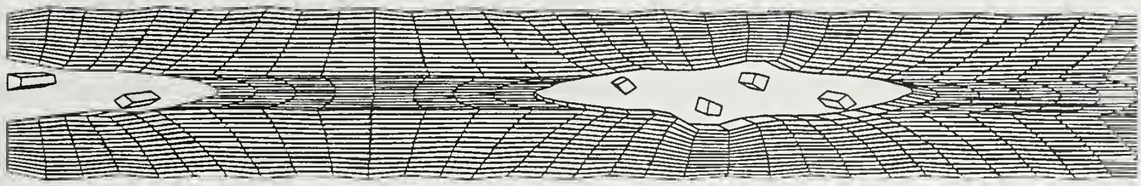

Cold worked

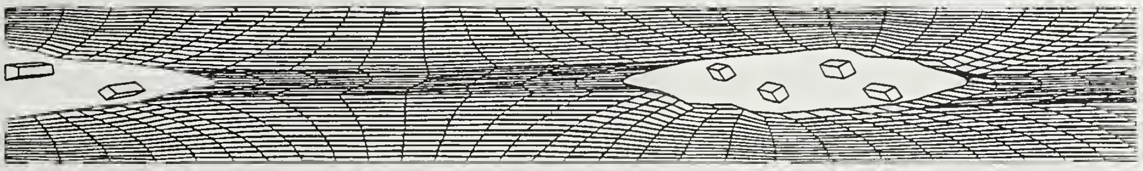

Hot worked, high strain rate

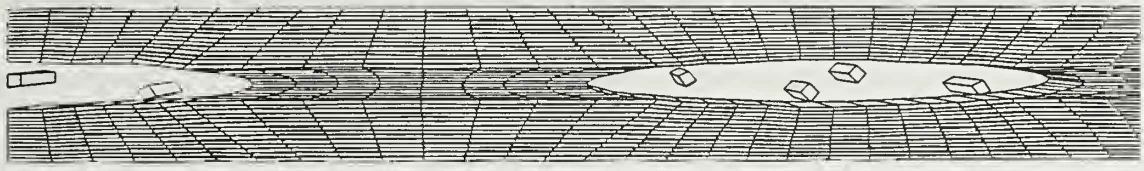

Hot worked, intermediate strain rate

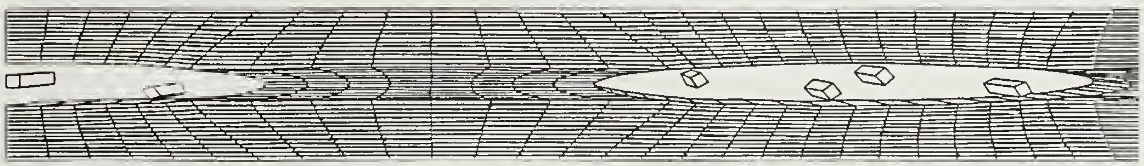

Hot worked, low strain rate

Figure 49: Visual view of cluster deformation in the small particle, 2% local volume fraction, discrete model with circular cluster regions after different methods of TMP to a true strain of 1.20.

for a circle of the same size, as shown in Figure 37. One exception to this is the mesh shown in Figure 41. In the cold worked models the material properties of the particles were smeared into the cluster regions of the smeared model but not in the discrete model. On the other hand, the stiffness of the particles was neglected in the cluster zone of the hot work, smeared models. In the discrete models the stiff particles were modeled in both the hot and cold worked models.

A qualitative comparison was made between the smeared and discrete models. When the horizontal displacement of the cluster center is compared as seen in Figures 33, 46 and 47, it is noted that both models show the same general trend of greater displacement for the hot work models vs. the cold work models. The general trend of more displacement for the low strain rate vs. the high strain rate hot worked model is also seen. In Figure 47, it is seen that the hot work, low strain-rate model provides the largest amount of relative movement among the discrete particles. Again, this indicates that the best TMP to reach homogeneity, in the least strain is the hot work, low strain-rate method for both the smeared and discrete models. This finding is also supported by Figure 49. In Figures 27 and 48, which show the height-to-width ratios of the cluster regions after deformation, it is seen that the results from the discrete model are similar to those of the cluster models. The exception is that the results of the hot work model at high strain rates is not consistent. This case requires further investigation. In the smeared models it was assumed that larger deformation of the cluster region would result in more homogeneity. This assumption was supported from the discrete models as seen in Figure 49. This figure shows that for larger deformation of the cluster zone, the particles are more fully dispersed. All of these comparisons give credibility to the work in Chapter III where the particle clusters are being modeled with smeared material properties. The smeared models are more efficient from a computational point of view and are considered a valid means of studying particle redistribution in a simplistic manner.

An observation is made that with a higher local particle volume fraction in the discrete models, particle redistribution does not as readily occur as compared to a lower local particle volume fraction. This is illustrated visually in Figure 50. This leads to the observation that, if the particle clusters in the consolidation process are tightly packed, particle homogeneity is harder to achieve. If the particle clusters are loosely packed, i.e., better mixing in the consolidation/fabrication technique, then particle homogeneity will more easily be reached. If the cluster zone has many particles, the particles will support the most load in the cluster zone and dominate the behavior of the cluster deformation. As a result the particle redistribution appears to be less likely. On the contrary, the matrix dominates the cluster zone behavior with a low local particle volume fraction.

Visual view of cluster deformation in the discrete models after hot working at an intermediate strain rate to a true strain of 1.20.

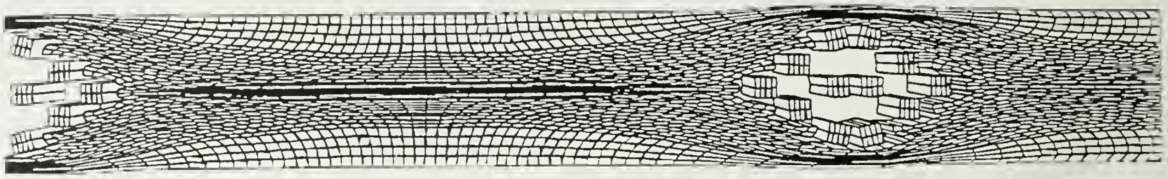

Large particle, 25% local volume fraction discrete model

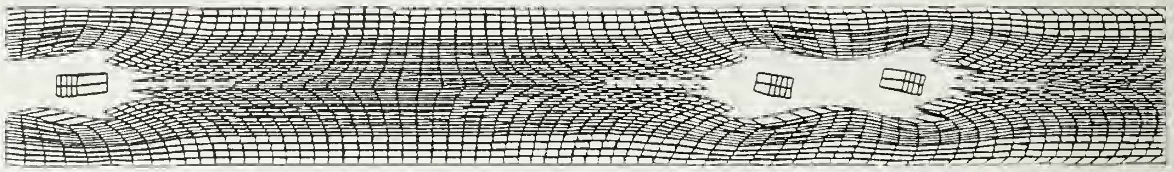

Large particle, 4% local volume fraction discrete model

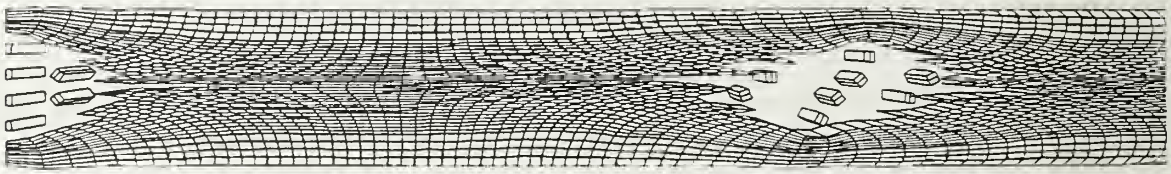

Small particle, 4% local volume fraction discrete model

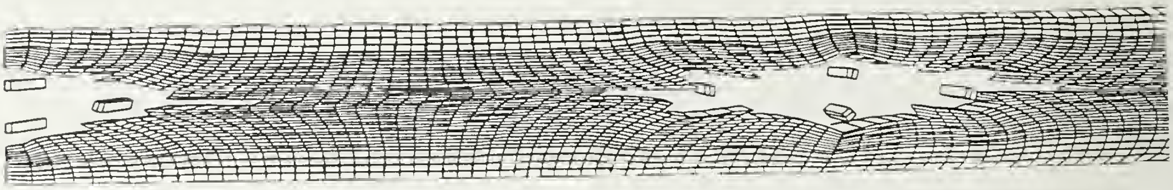

Small particle, 2% local volume fraction discrete model

Figure 50: Visual view of cluster deformation in the discrete models after hot working at an intermediate strain rate to a true strain of 1.20.

V. SUMMARY

A. CONCLUSIONS

The following conclusions are drawn from this work:

1. The current modeling methods, both smeared and discrete, used to model MMC deformation is an inexpensive and informative means of evaluating the matrix and cluster material behavior during the entire deformation process.

2. After cold working all the smeared models exhibited higher stresses and lower effective plastic strains within the cluster regions.

3. After hot and cold working all the discrete models exhibited higher stresses and lower effective plastic strains in and around the particles.

4. After hot working at the low strain rates, all the smeared models exhibit lower stresses and higher effective plastic strains within the cluster region as compared to the matrix region.

5. After hot working at the intermediate strain rates all the smeared models exhibit higher stresses and higher effective plastic strains within the cluster region as compared to the matrix region. These higher stresses in the cluster region only become apparent near the end of the deformation process and is a result of the fact that the true strain rate is higher near the end of the hot working process compared to the beginning of the hot working process.

6. After hot working at the high strain rates all the smeared models exhibit no distinction between the cluster regions and the matrix regions.

7. The results, using the linear law compared to the quadratic law, in the cluster regions of the smeared models after hot working at intermediate and low strain rates, are as follows. The difference in effective plastic strains between the linear and quadratic laws is very small for both strain rates. The linear law results in higher stresses within the cluster regions for the intermediate strain rate model and lower stresses for the low strain rate model, when compared to the quadratic law.

8. Internal stresses achieved in the cold worked models are an order of magnitude higher than those achieved during the hot worked models.

9. Internal stresses achieved in the hot worked, high strain rate models are twice the value as those found in the hot worked, low strain rate models.

10. Particle homogeneity within the matrix material is better achieved using a hot working process vs. a cold working process. This is supported by the deformability of the clusters in the smeared models as measured in terms of height to width ratios of the clusters after straining, the vertical compression of the cluster material compared to the matrix material after straining and the horizontal displacement of the cluster centers during the straining process. The relative particle movement in the discrete models also support this finding.

11. Particulate homogeneity within the matrix material is better achieved using a lower strain rate hot working process. This is supported by the same measures described in the previous conclusion.

B. RECOMMENDATIONS

The following recommendations are made for subsequent studies:

1. The current model does not allow breaking down of a single cluster into smaller clusters and mixing within the surrounding matrix material. A further experimental study is needed to gain more insight of the actual physical occurrence within MMC's during TMP. The subsequent study should improve the modeling technique to more closely describe the actual phenomena. For this description the Eulerian-Lagrangian technique of the FEM might be more suitable.

2. The current FEM package used does not allow for combining constitutive equations of a material region for different mechanisms of creep. During the deformation process, the mechanisms of creep can change based on current stresses or strain rates. It is suggested that in the further development of this study, additive constitutive laws need to be incorporated into the FEM program.

3. The discrete model needs to be further developed. Focus should be on the effects of initial particle distribution within the cluster regions including size, arrangement and local volume fraction, and the size or boundary of the cluster zones. Also the discrepancy between the smeared model and discrete model for the hot worked high strain rate case needs further investigation.

APPENDIX A: FRINGE PLOTS OF EFFECTIVE VON MISES STRESS AND EFFECTIVE PLASTIC STRAIN FOR ALL COLD WORKED SMEARED MODELS.

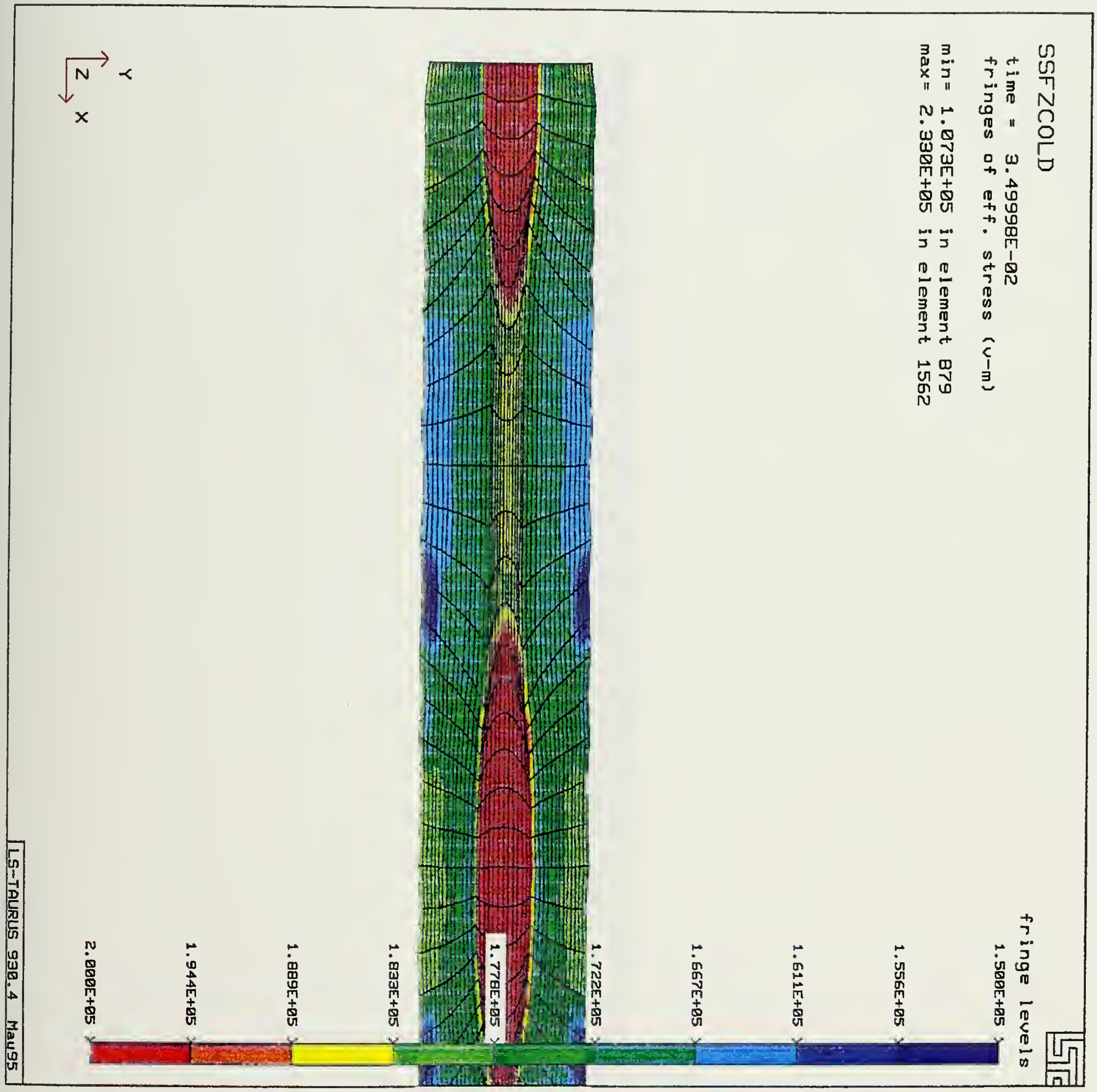

Figure A1: Fringe plot of Effective Von-Mises stress for the two cluster horizontal arrangement in the cold worked model at a true strain of 1.20.

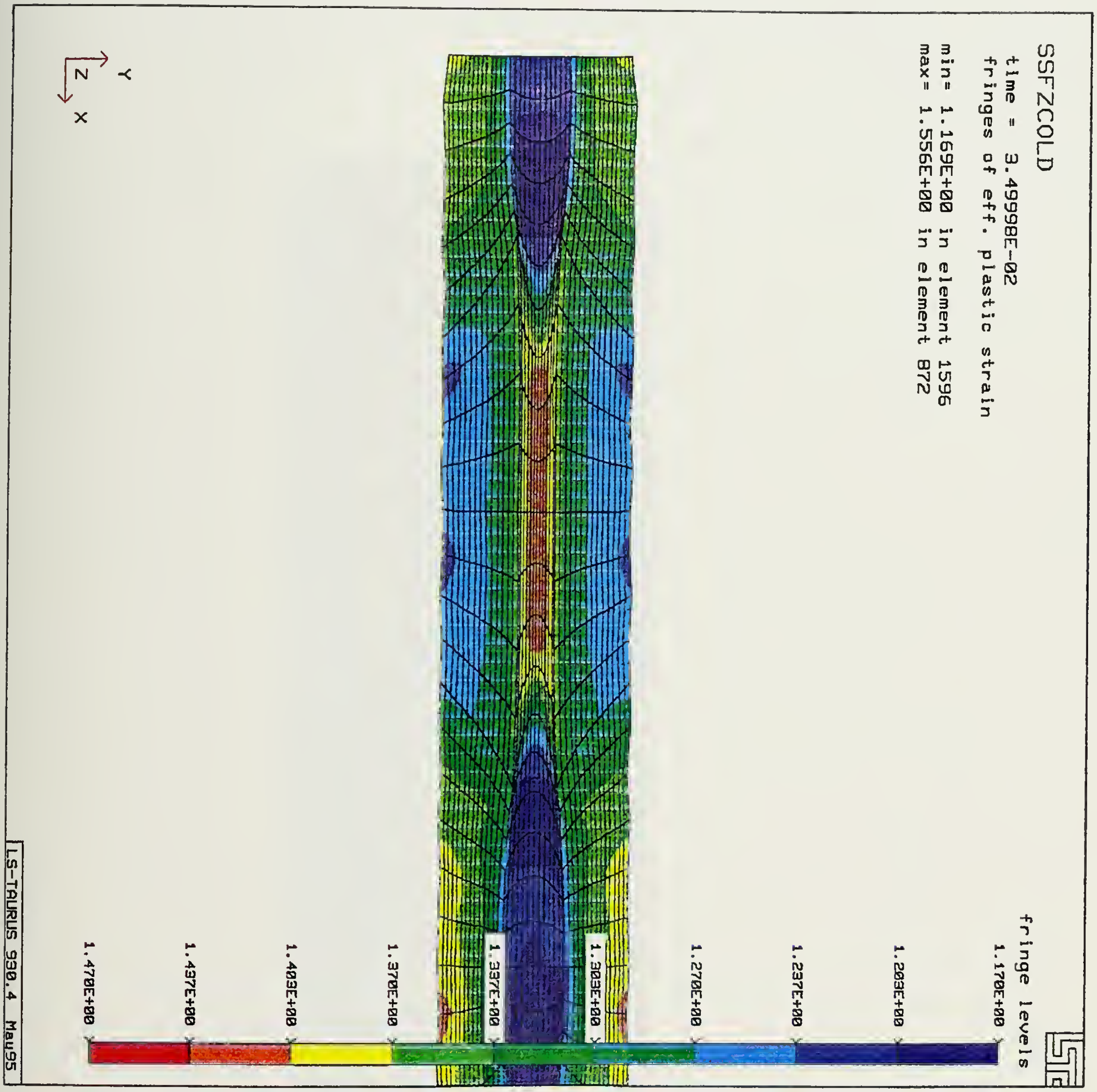

Figure A2: Fringe plot of Effective plastic strain for the two cluster horizontal arrangement in the cold worked model at a true strain of 1.20.

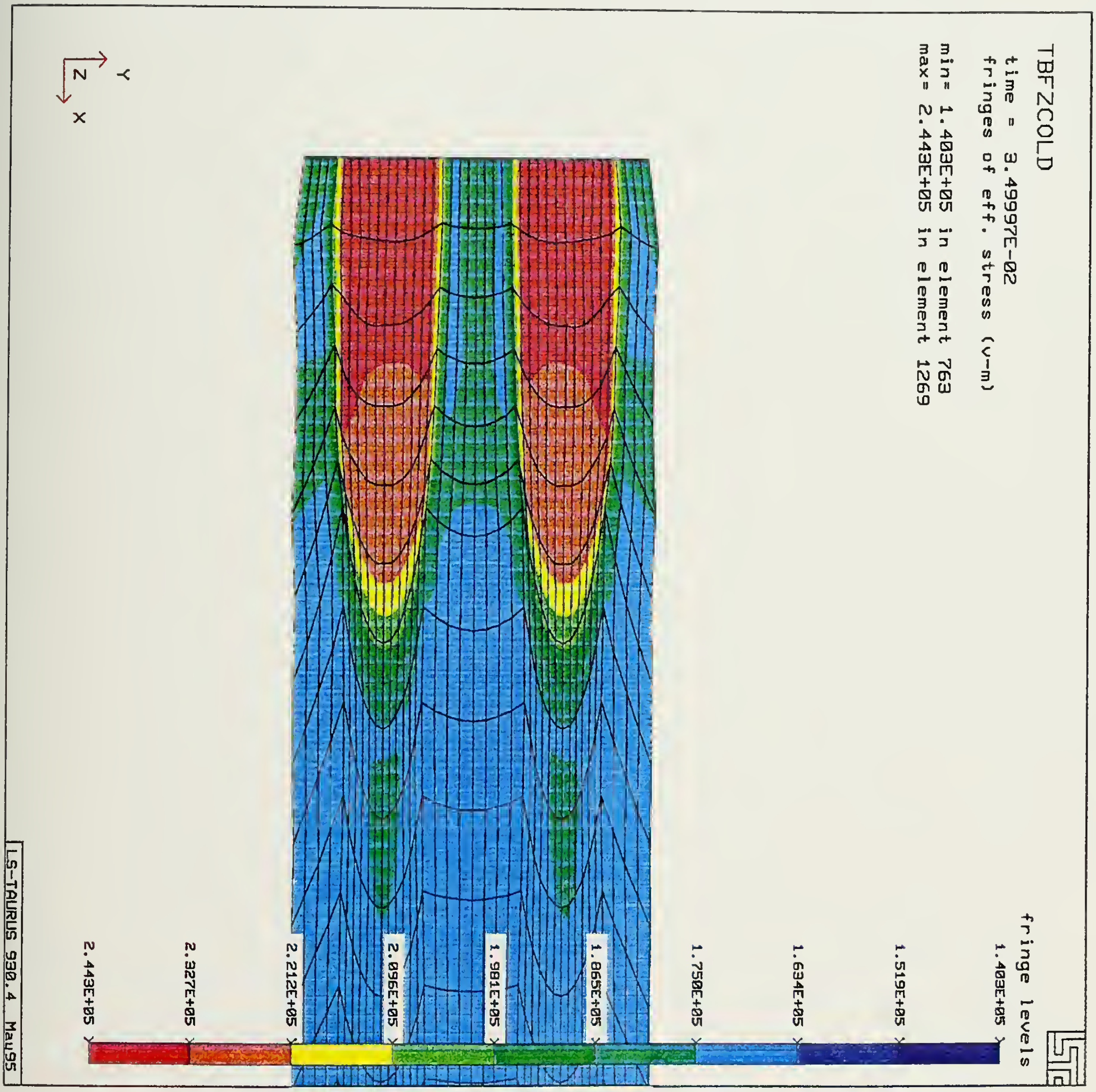

Figure A3: Fringe plot of Effective Von-Mises stress for the two cluster vertical arrangement in the cold worked model at a true strain of 1.20.

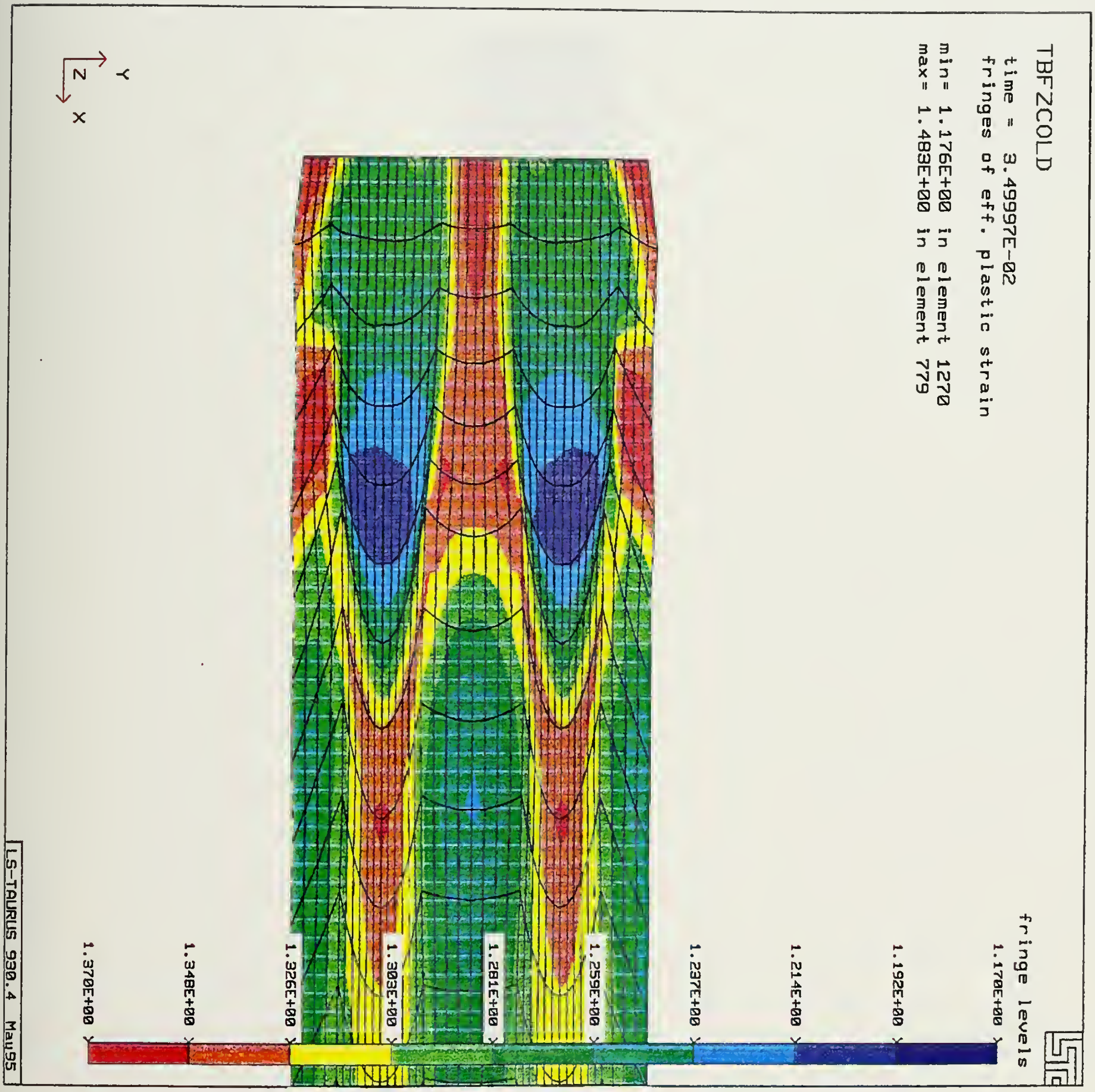

Figure A4: Fringe plot of Effective plastic strain for the two cluster vertical arrangement in the cold worked model at a true strain of 1.20.

20:21:13,12/1/96

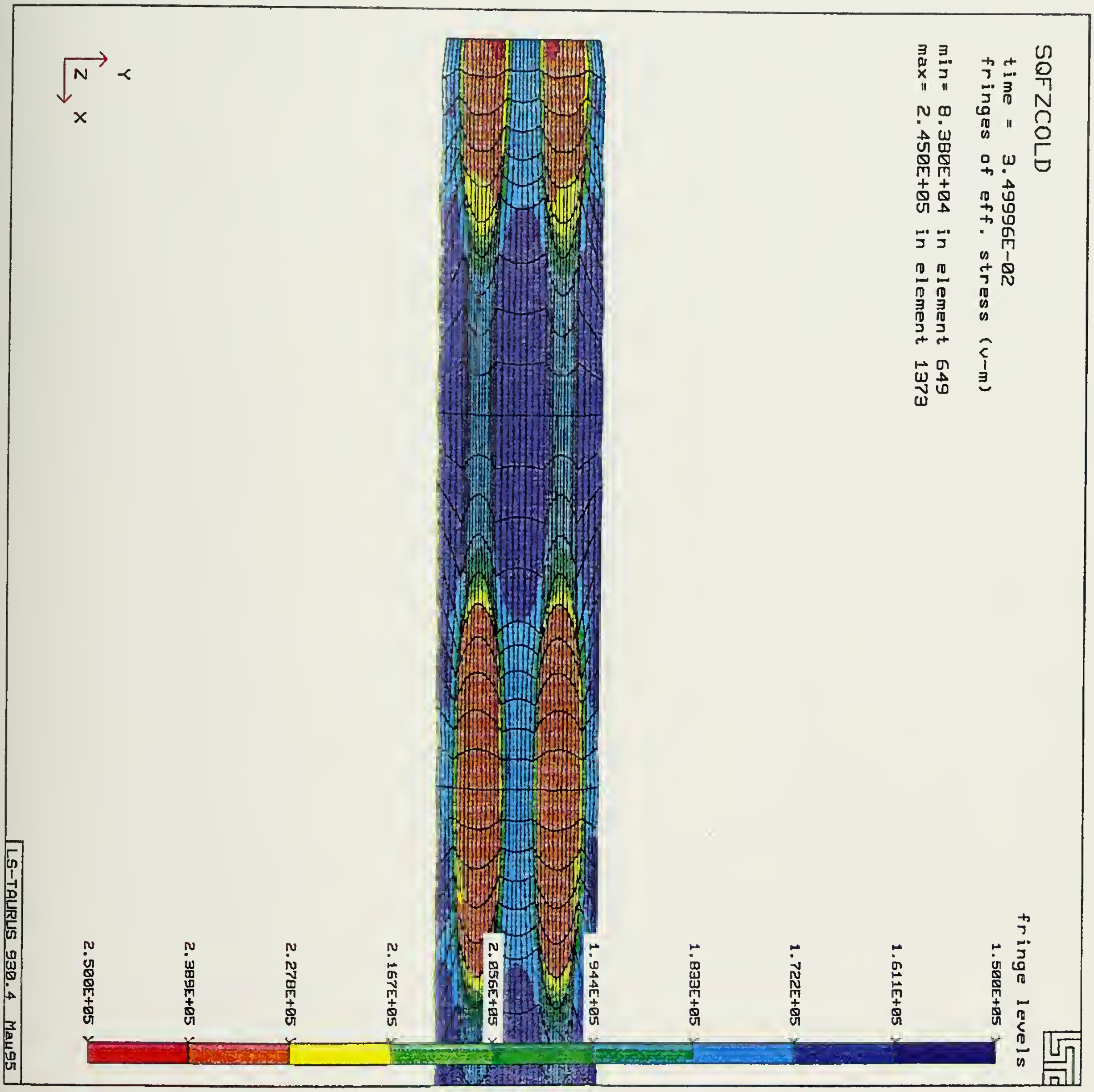

Figure A5: Fringe plot of Effective Von-Mises stress for the square shaped cluster arrangement in the cold worked model at a true strain of 1.20.

8:57:35, 1/13/97

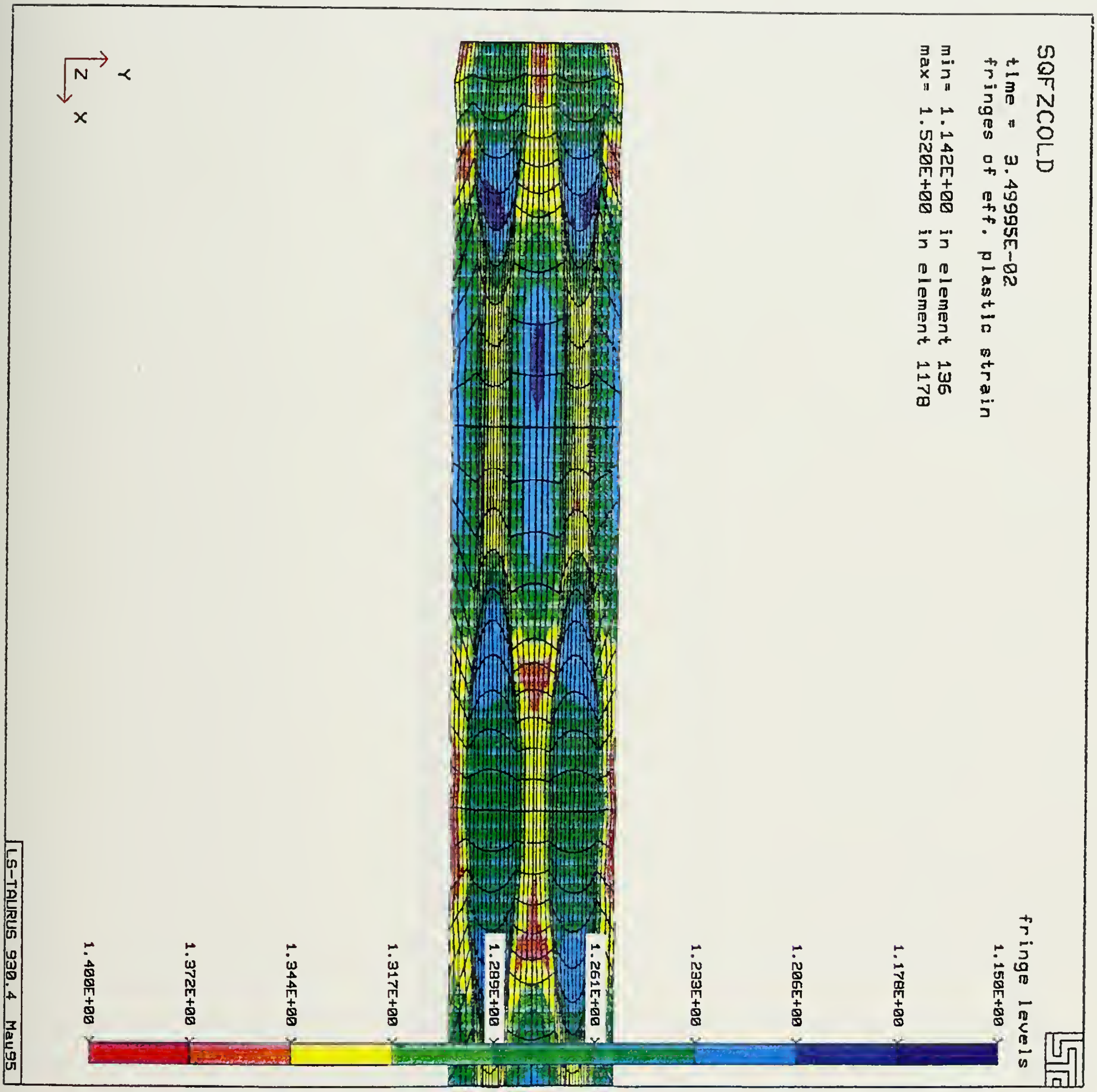

Figure A6: Fringe plot of Effective plastic strain for the square shaped cluster arrangement in the cold worked model at a true strain of 1.20.

13:37:13,12/11/96

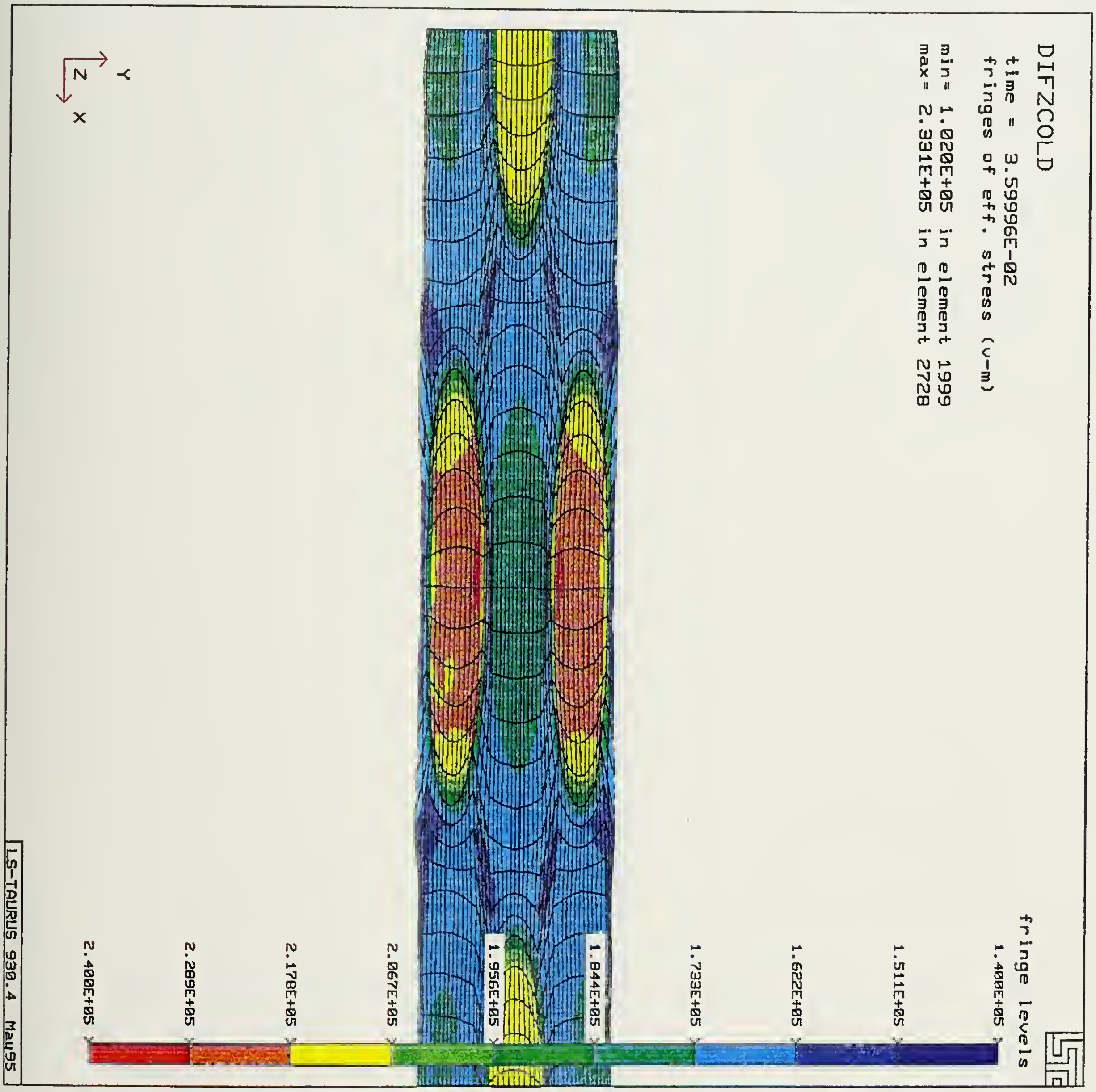

Figure A7: Fringe plot of Effective Von-Mises stress for the diamond shaped cluster arrangement in the cold worked model at a true strain of 1.13.

13:37:32,12/11/96

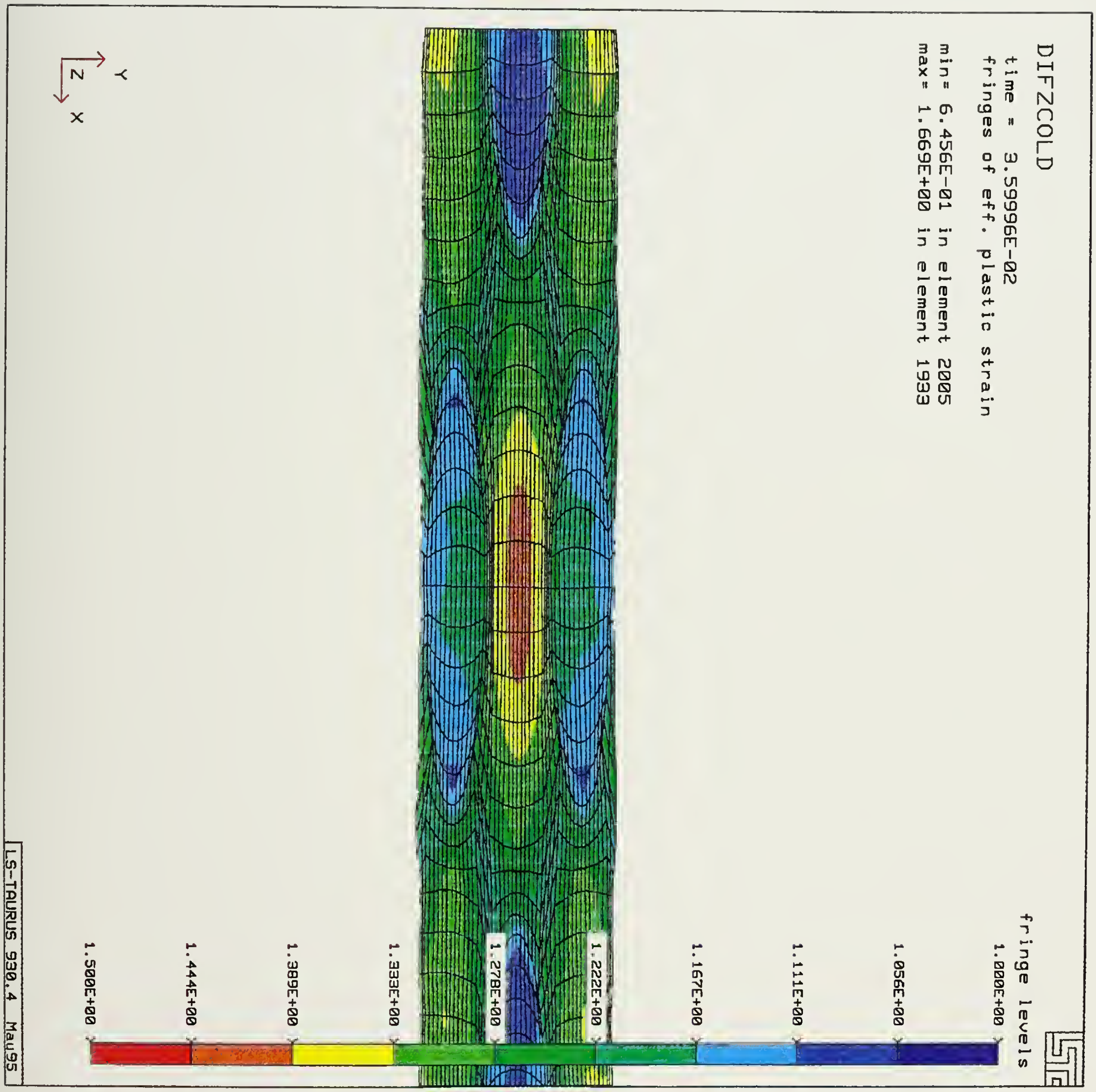

Figure A8: Fringe plot of Effective plastic strain for the diamond shaped cluster arrangement in the cold worked model at a true strain of 1.13

APPENDIX B: FRINGE PLOTS OF EFFECTIVE VON MISES STRESS AND EFFECTIVE PLASTIC STRAIN FOR ALL HOT WORKED SMEARED MODELS.

19:5:9, 1/18/97

©

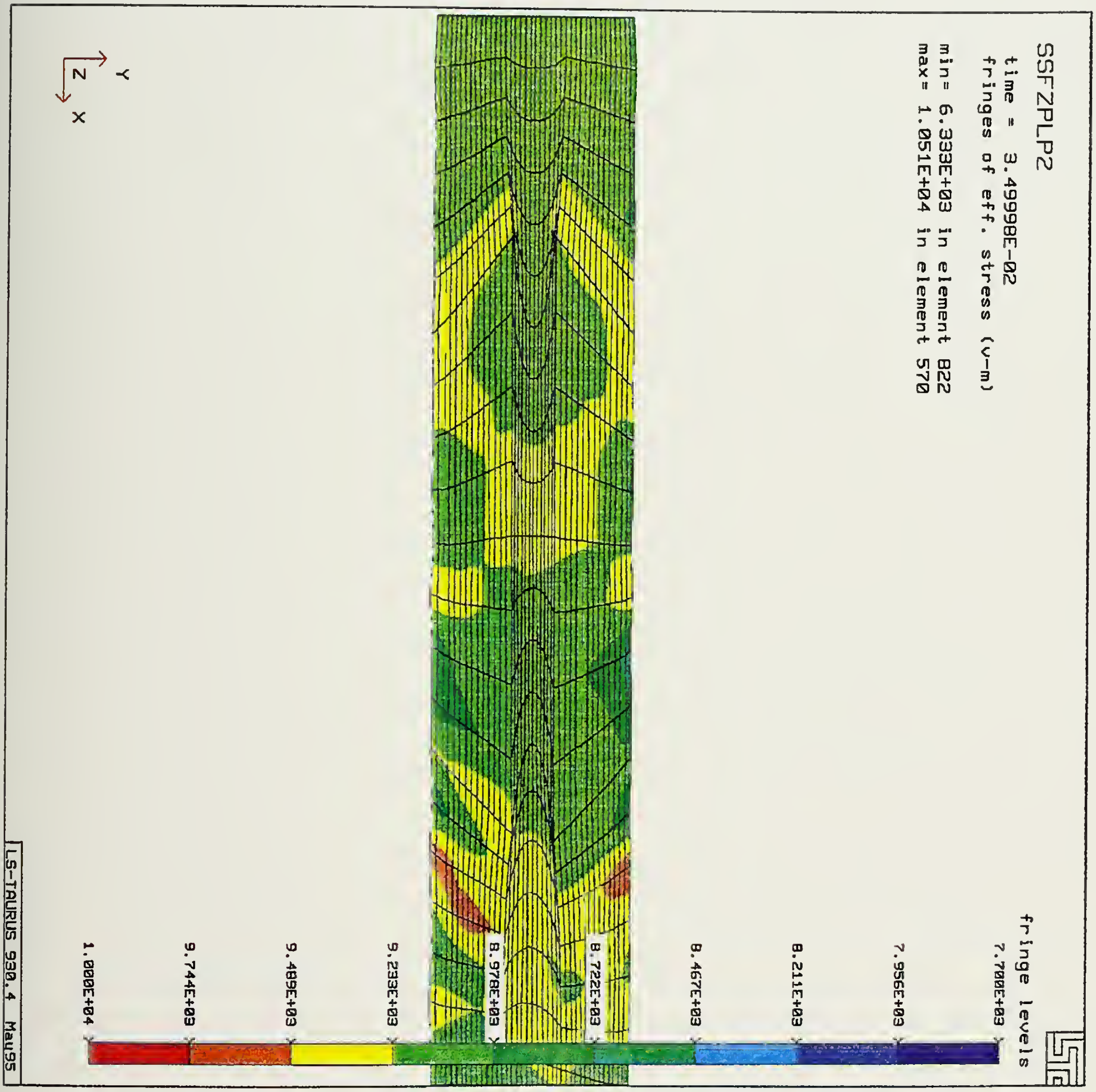

Figure B1: Fringe plot of Effective Von-Mises stress for the two cluster horizontal arrangement in the hot worked high strain rate model at a true strain of 1.20.

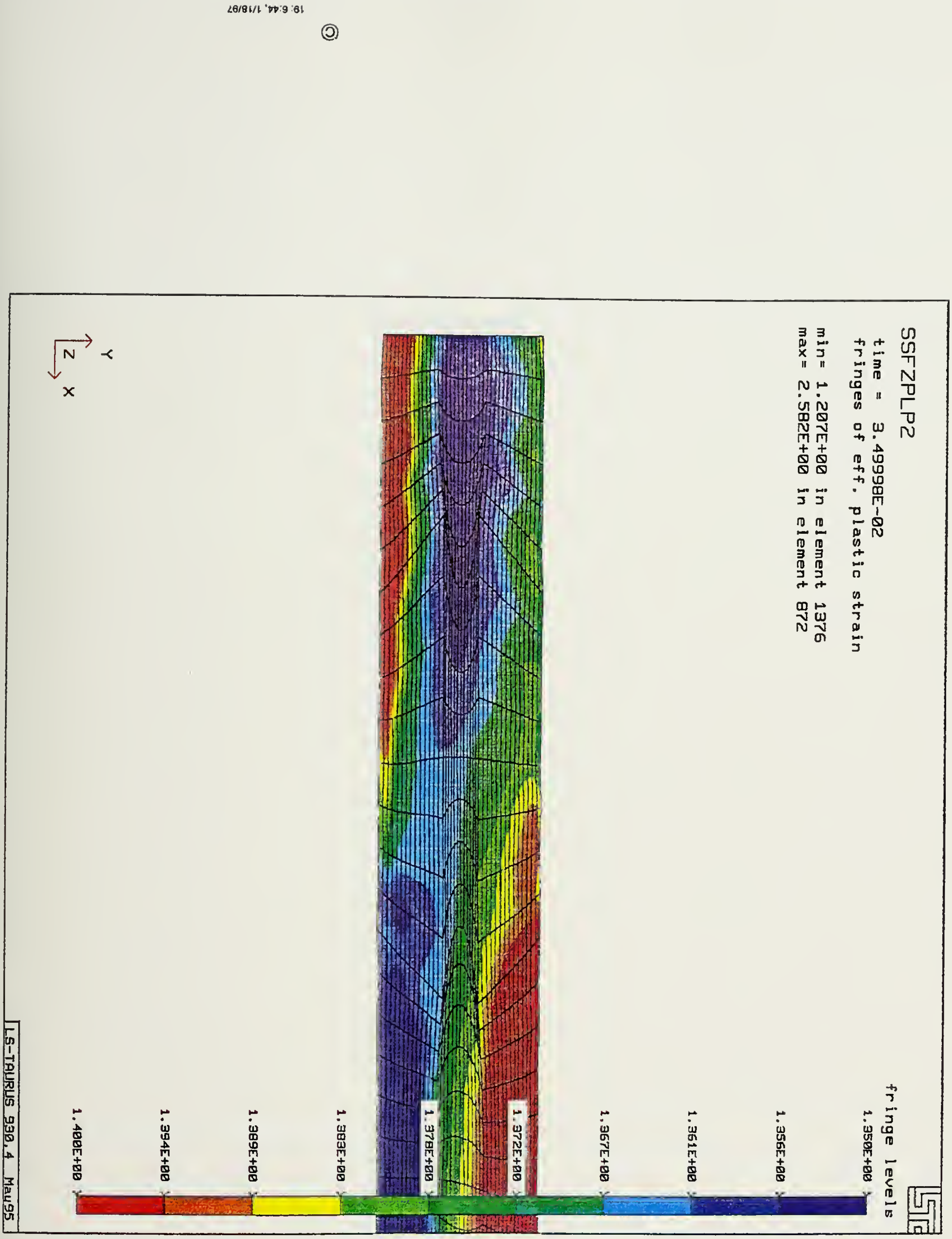

Figure B2: Fringe plot of Effective plastic strain for the two cluster horizontal arrangement in the hot worked high strain rate model at a true strain of 1.20.

13:14:12.12/ 9/96

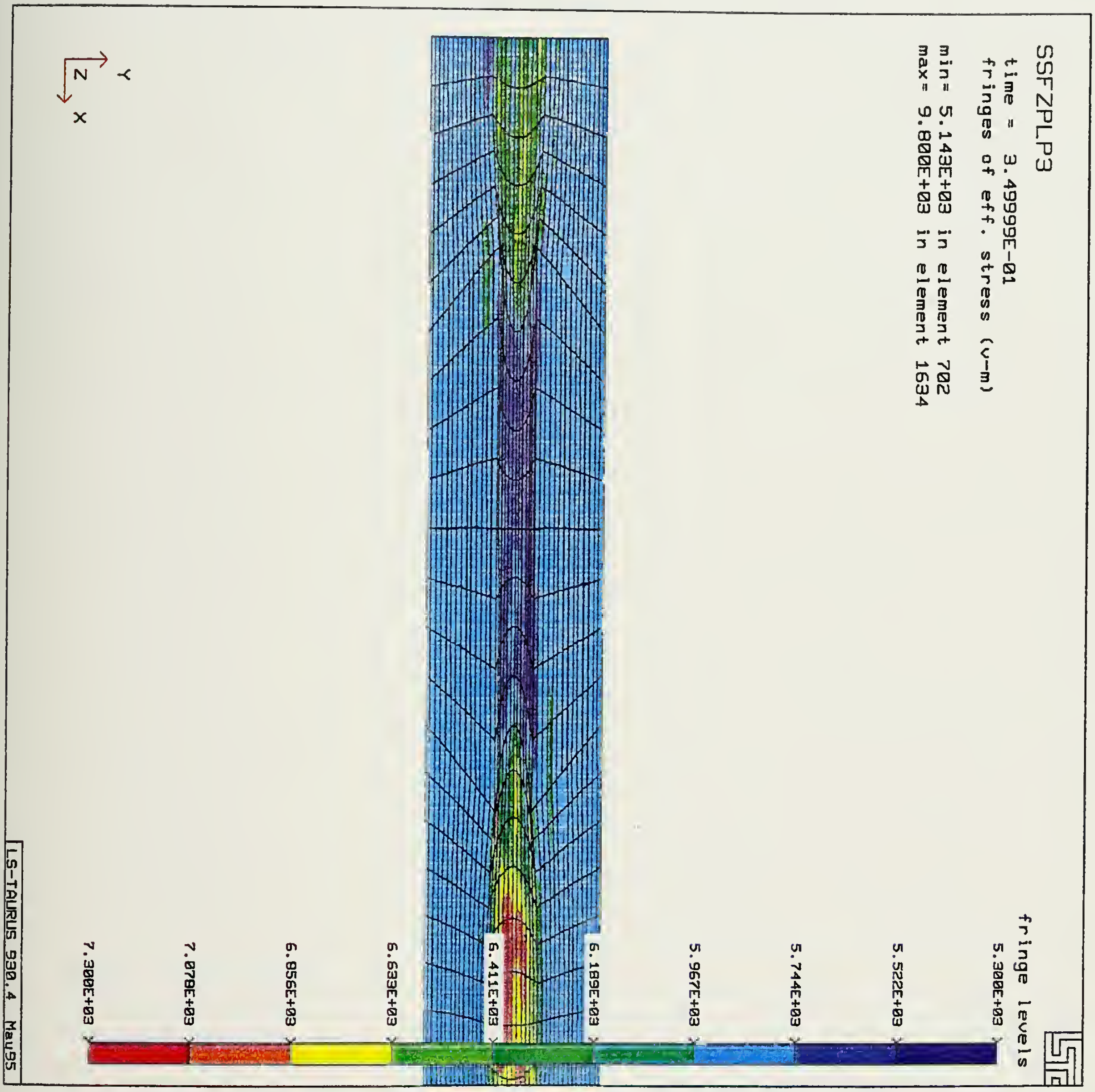

Figure B3: Fringe plot of Effective Von-Mises stress for the two cluster horizontal arrangement in the hot worked intermediate strain rate model at a true strain of 1.20.

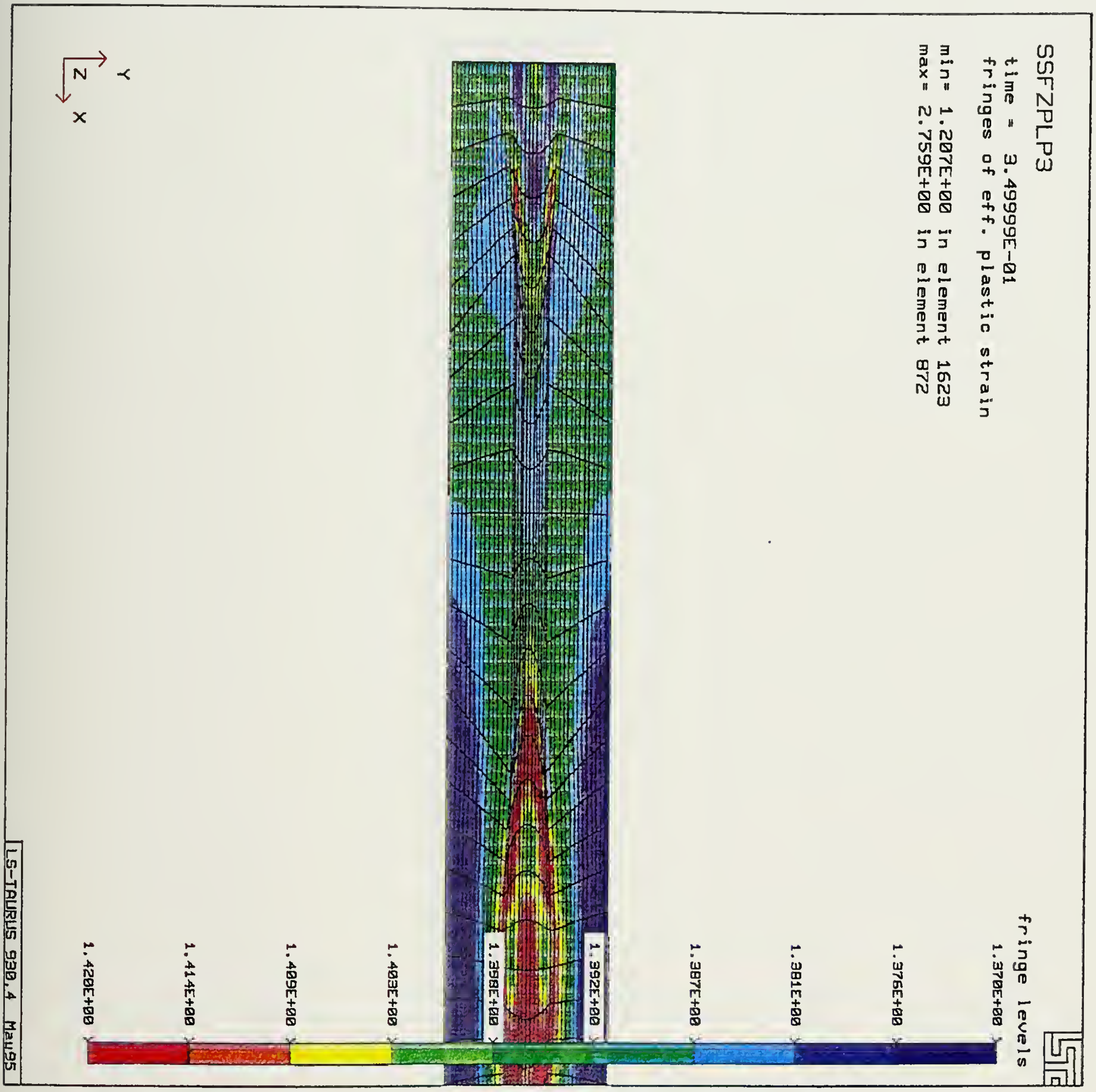

Figure B4: Fringe plot of Effective plastic strain for the two cluster horizontal arrangement in the hot worked intermediate strain rate model at a true strain of 1.20.

13:19:58,12/ 9/96

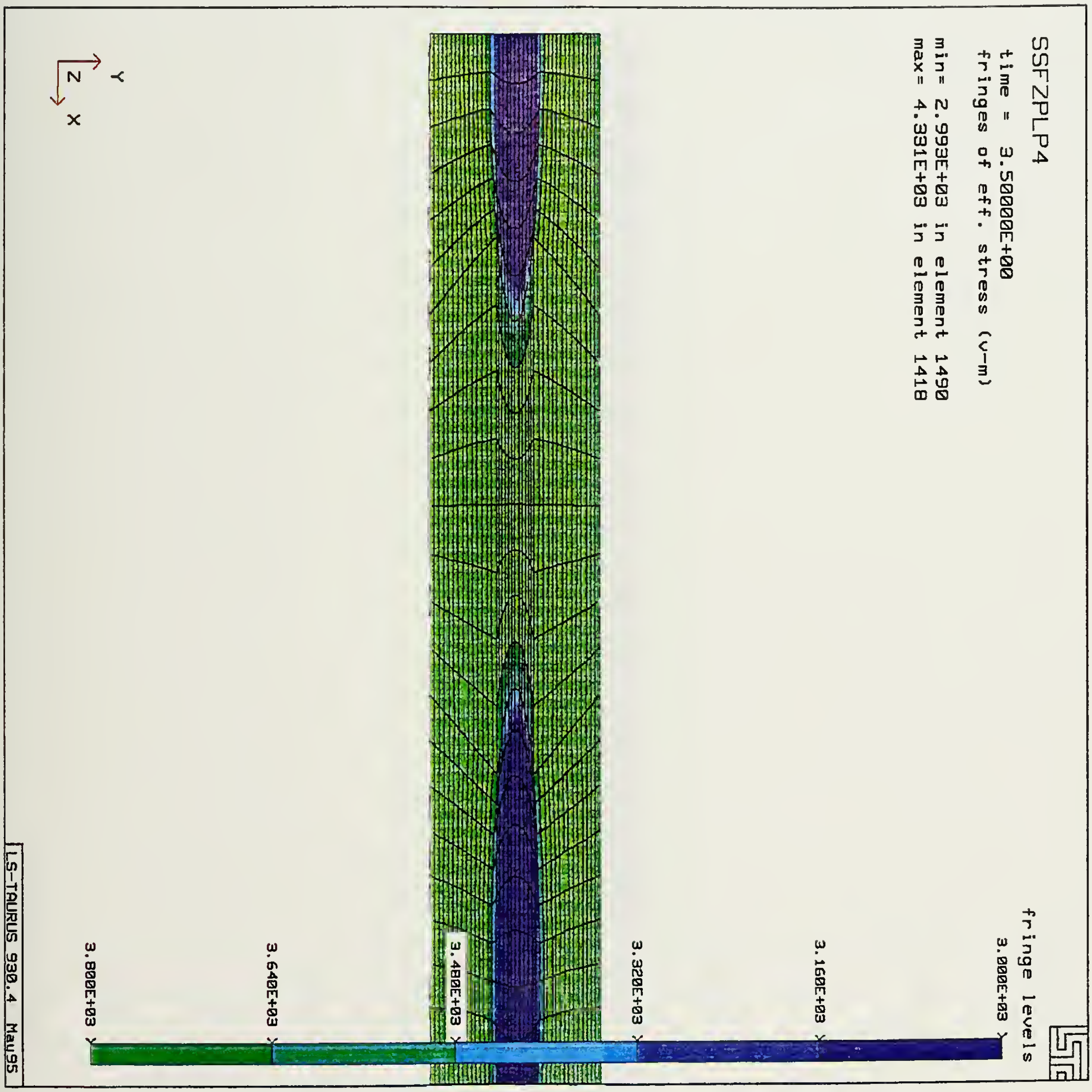

Figure B5: Fringe plot of Effective Von-Mises stress for the two cluster horizontal arrangement in the hot worked low strain rate model at a true strain of 1.20.

22:32:34, 1/9/97

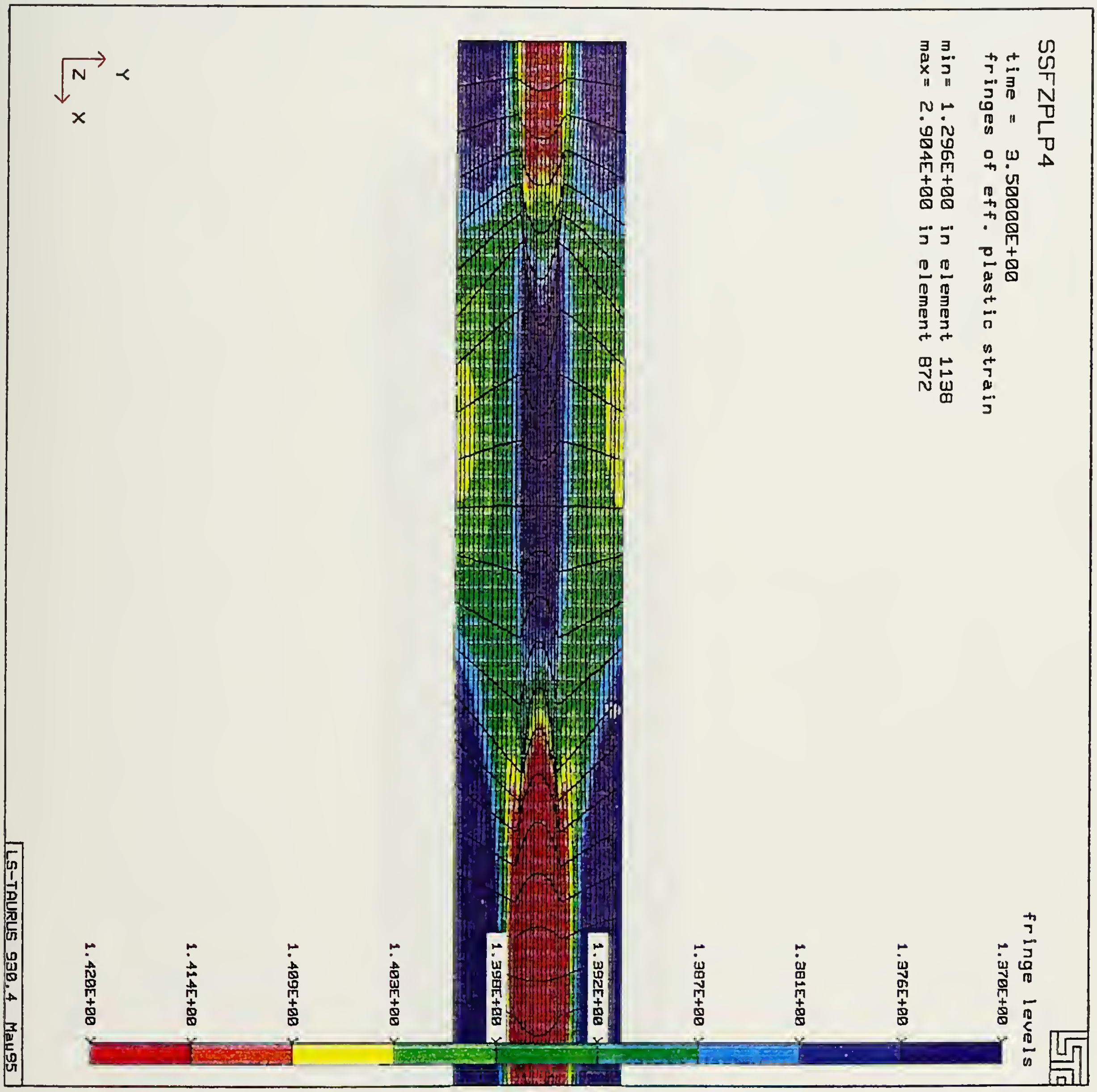

Figure B6: Fringe plot of Effective plastic strain for the two cluster horizontal arrangement in the hot worked low strain rate model at a true strain of 1.20.

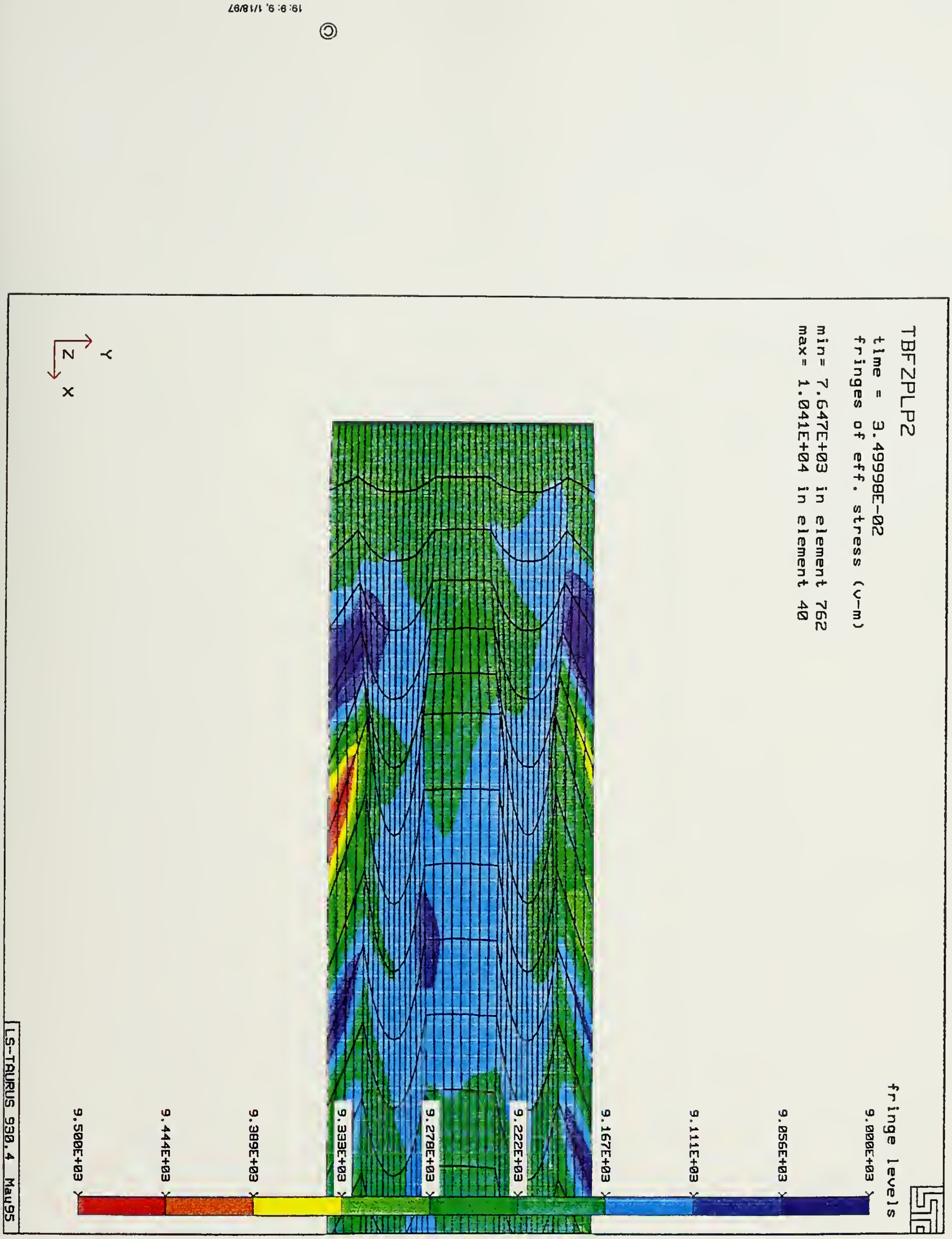

Figure B7: Fringe plot of Effective Von-Mises stress for the two cluster vertical arrangement in the hot worked high strain rate model at a true strain of 1.20.

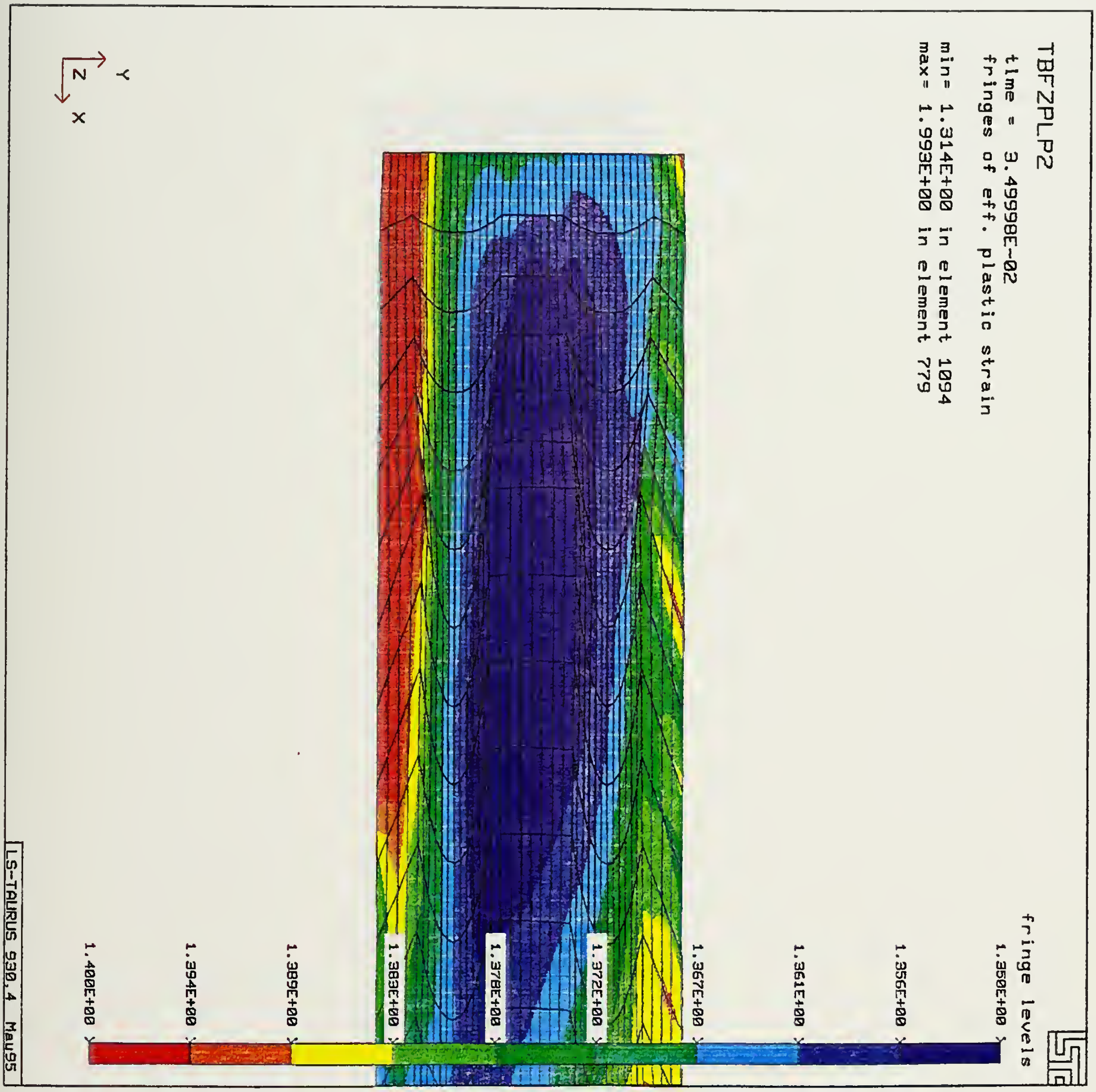

Figure B8: Fringe plot of Effective plastic strain for the two cluster vertical arrangement in the hot worked high strain rate model at a true strain of 1.20.

13:40:7.12/9/96

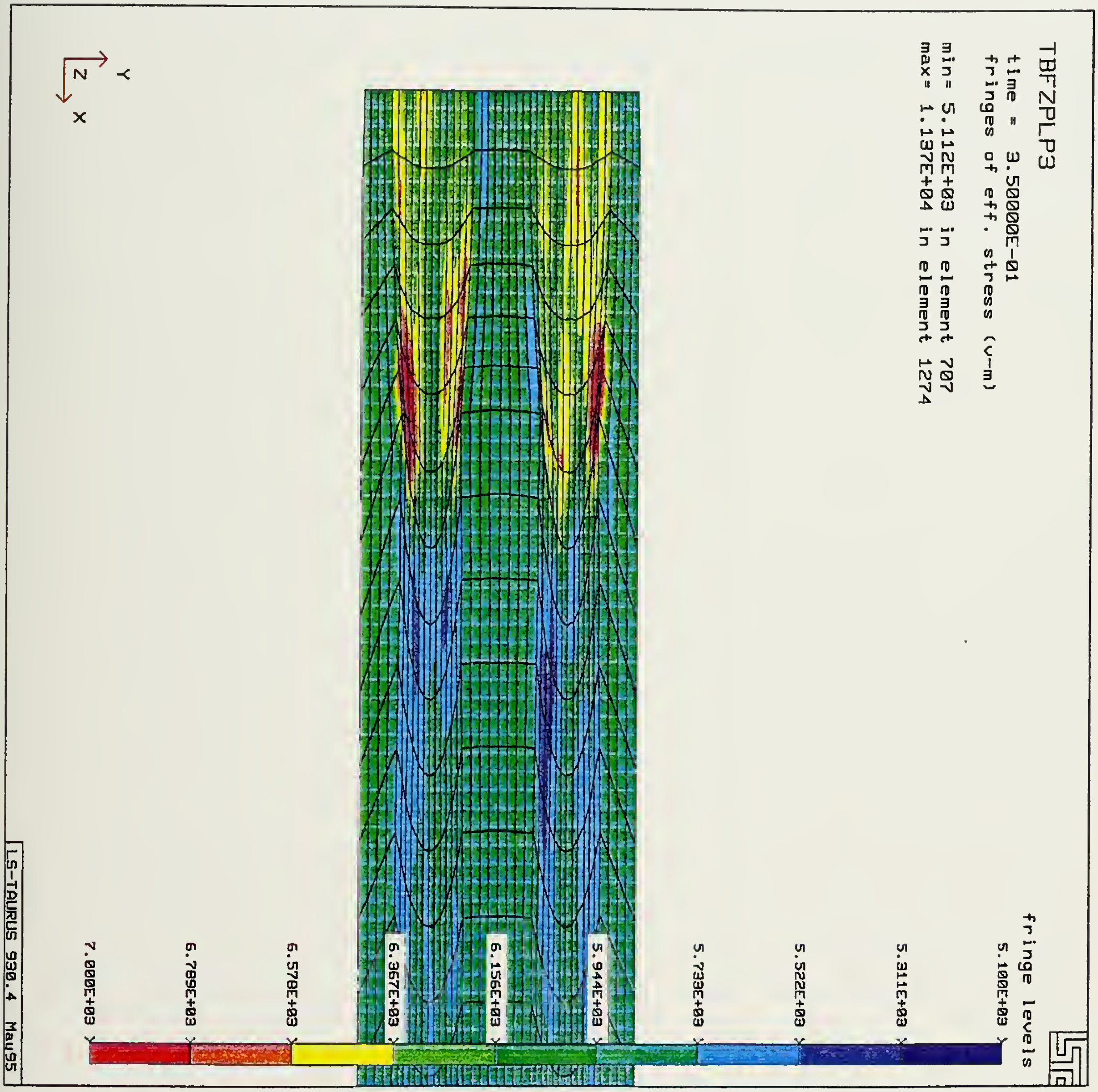

Figure B9: Fringe plot of Effective Von-Mises stress for the two cluster vertical arrangement in the hot worked intermediate strain rate model at a true strain of 1.20.

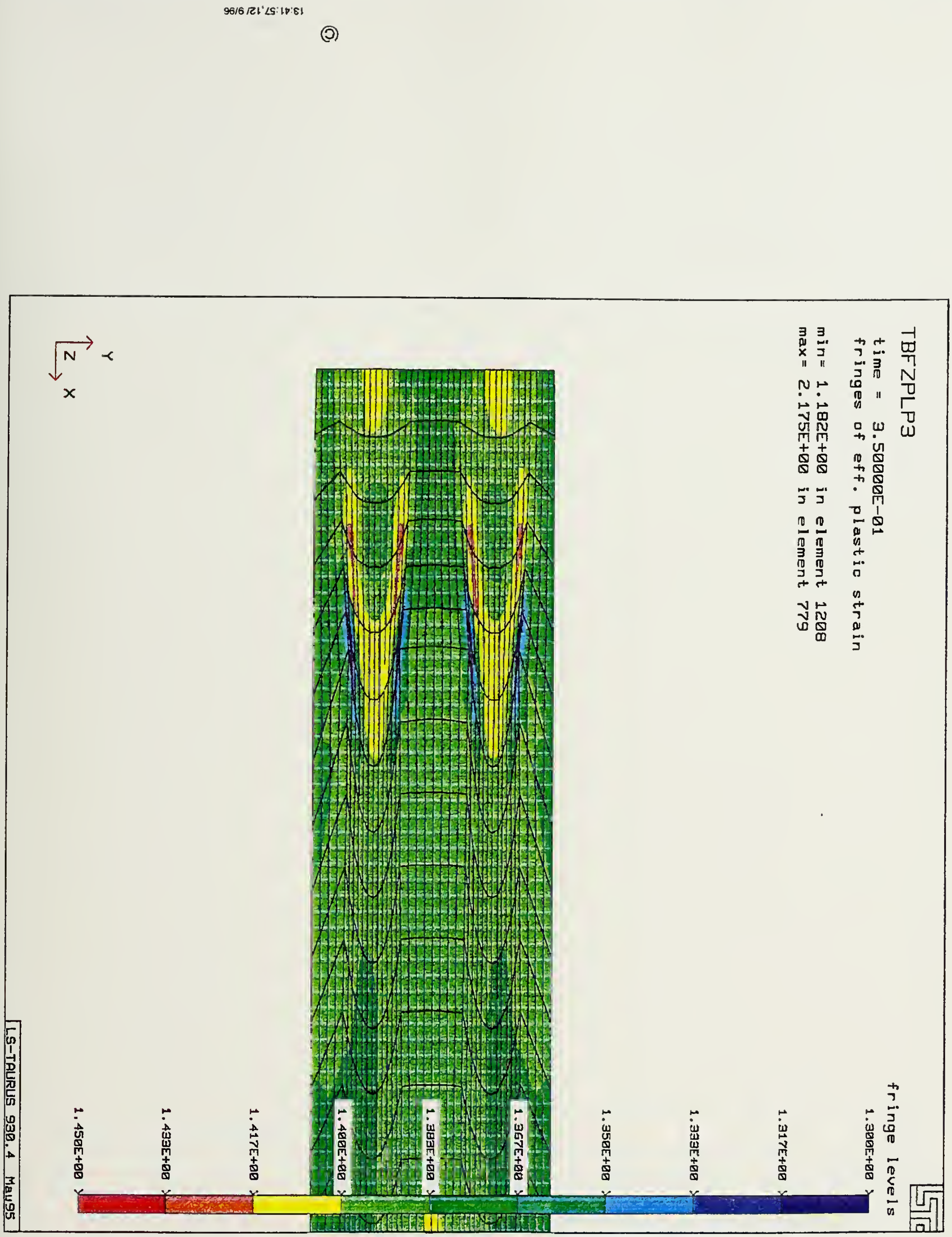

Figure B10: Fringe plot of Effective plastic strain for the two cluster vertical arrangement in the hot worked intermediate strain rate model at a true strain of 1.20.

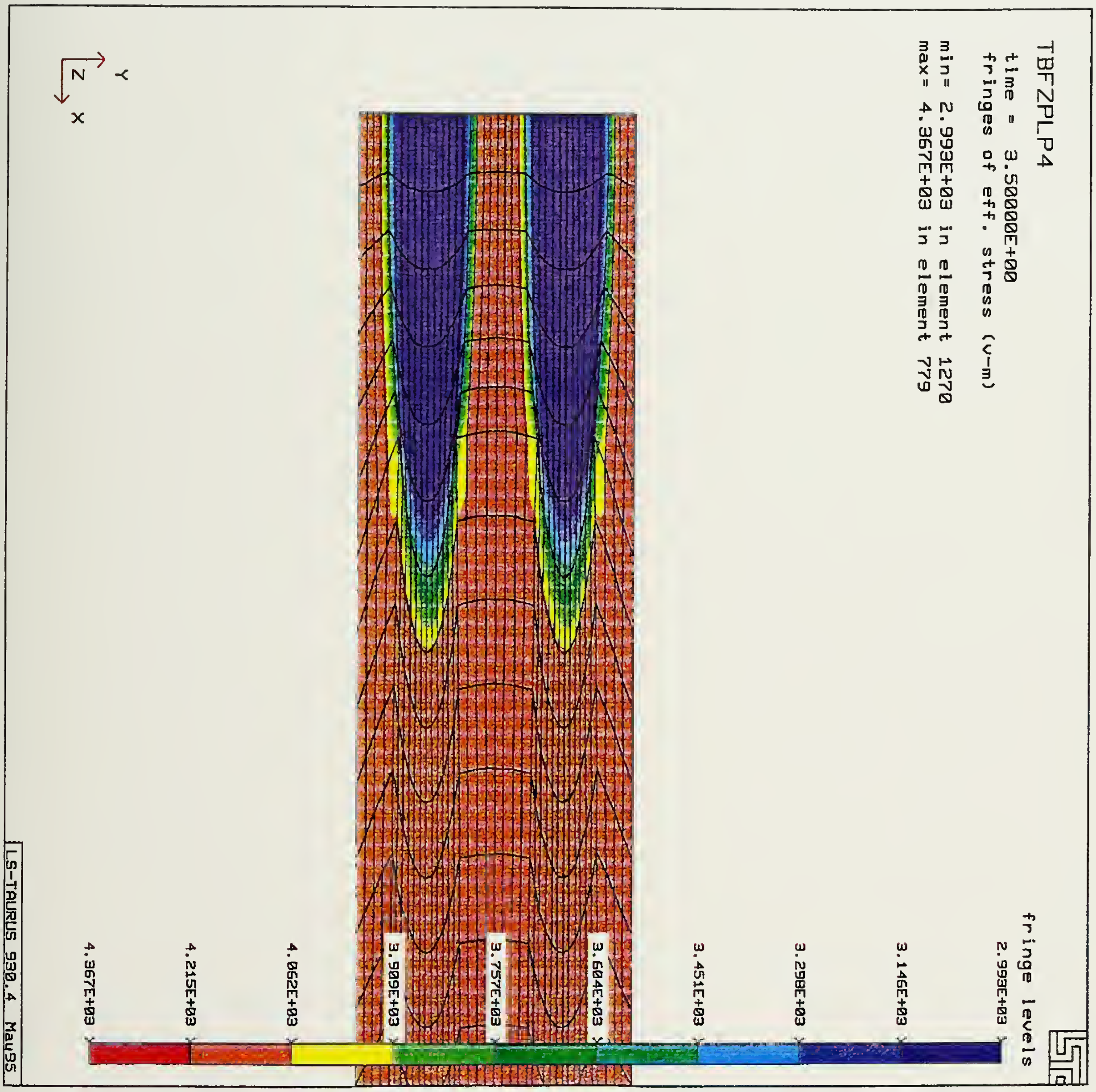

Figure B11: Fringe plot of Effective Von-Mises stress for the two cluster vertical arrangement in the hot worked low strain rate model at a true strain of 1.20.

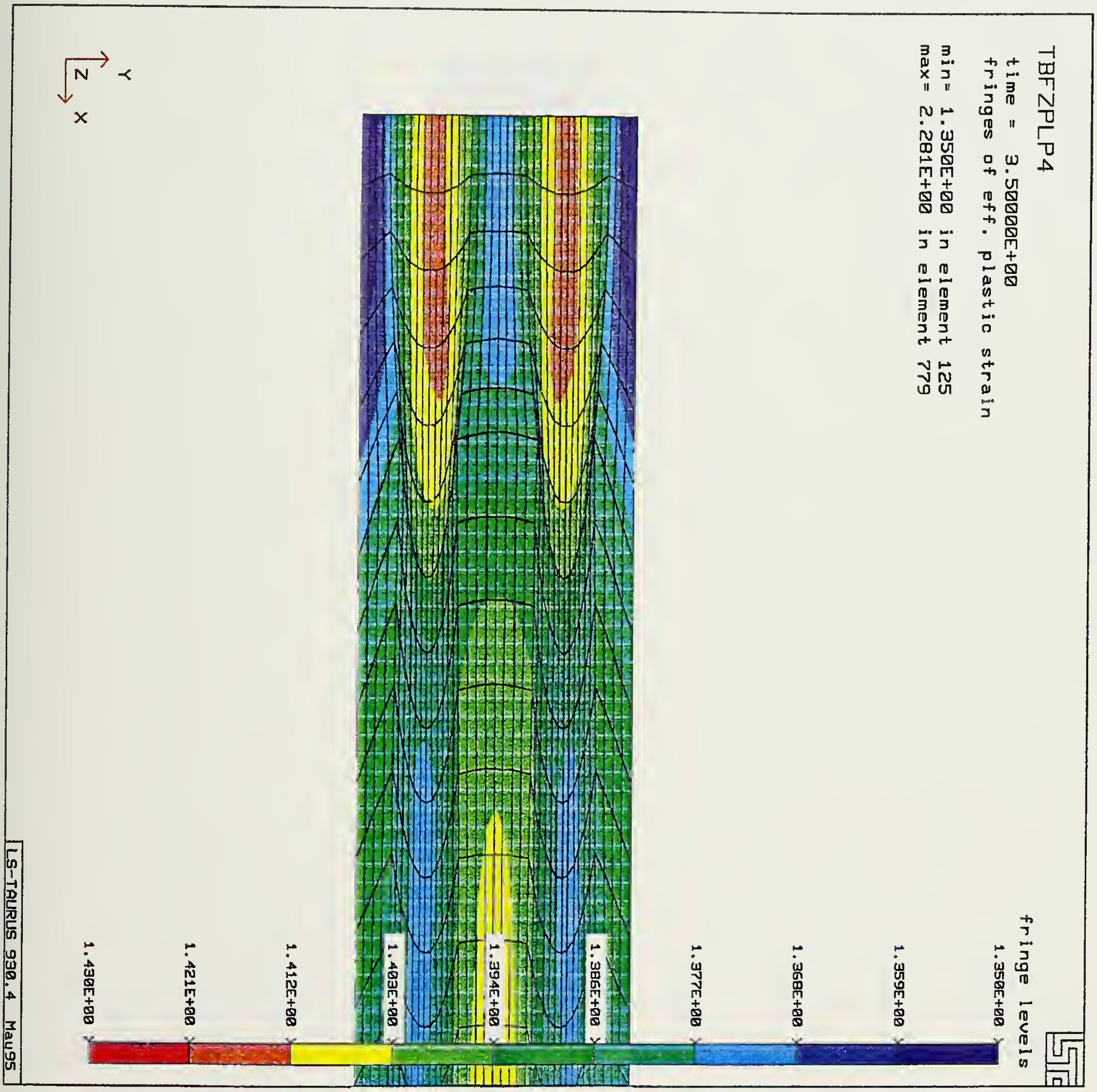

Figure B12: Fringe plot of Effective plastic strain for the two cluster vertical arrangement in the hot worked low strain rate model at a true strain of 1.20.

Figure B13: Fringe plot of Effective Von-Mises stress for the square cluster arrangement in the hot worked high strain rate model at a true strain of 1.20.

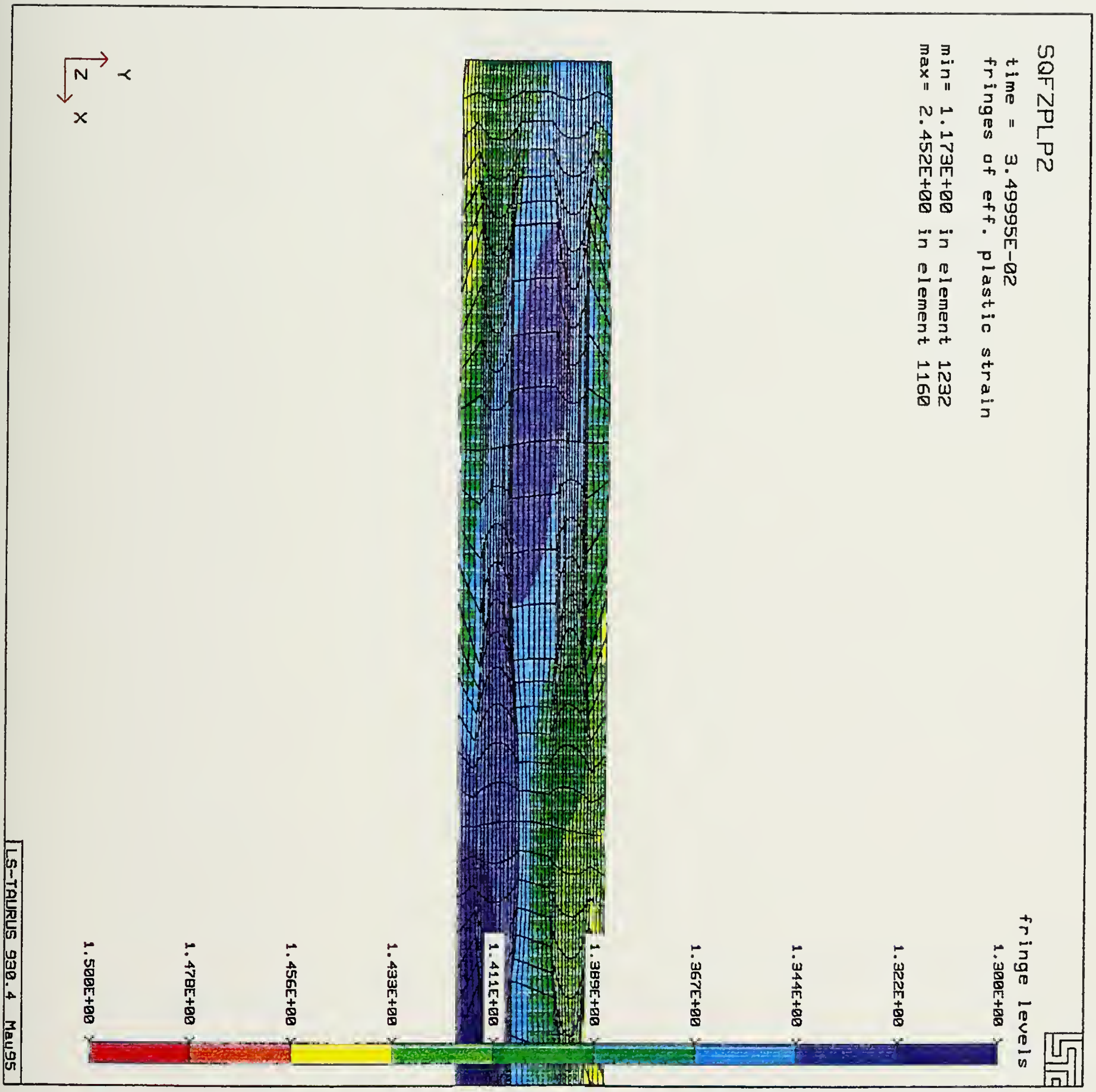

Figure B14: Fringe plot of Effective plastic strain for the square cluster arrangement in the hot worked high strain rate model at a true strain of 1.20.

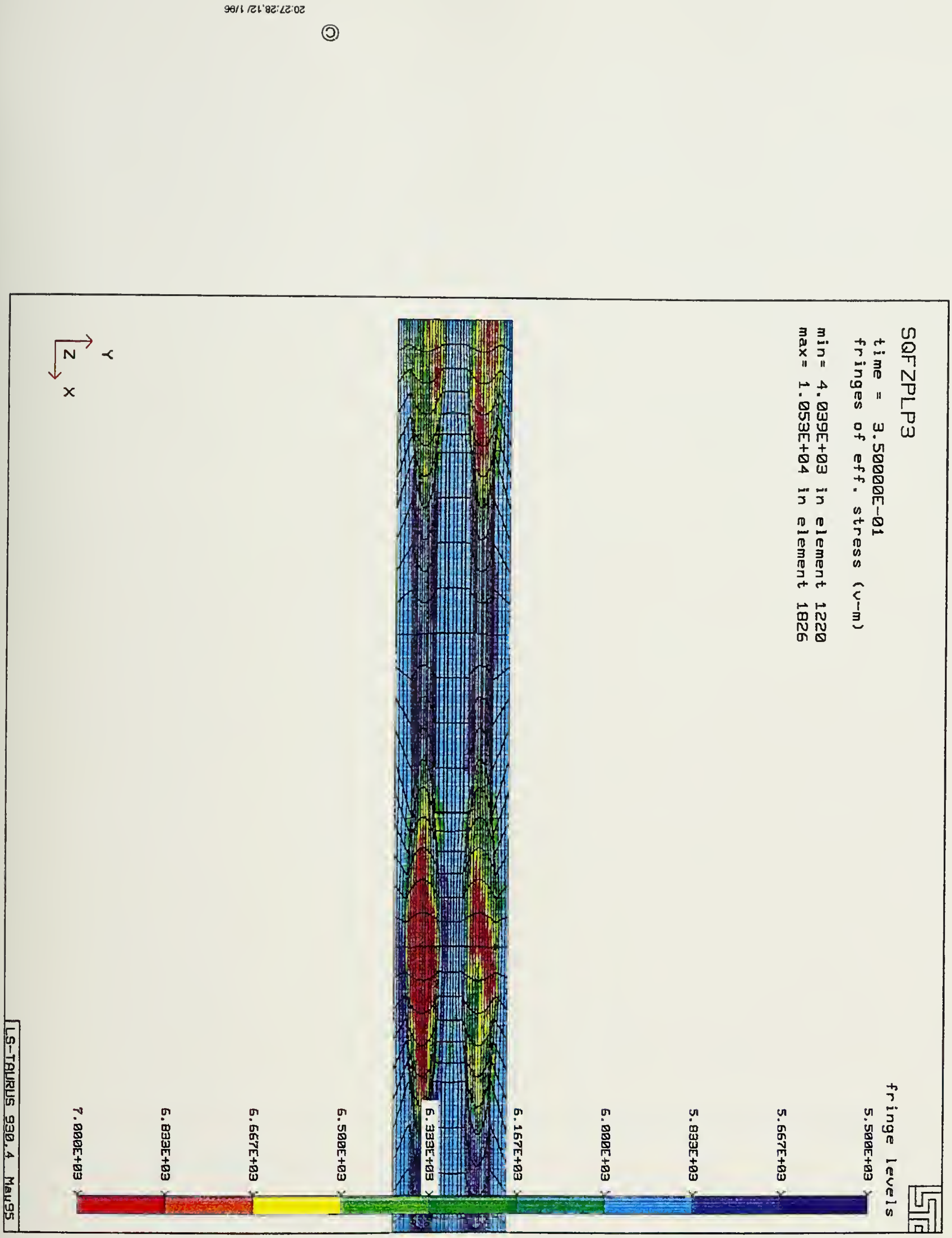

Figure B15: Fringe plot of Effective Von-Mises stress for the square cluster arrangement in the hot worked intermediate strain rate model at a true strain of 1.20.

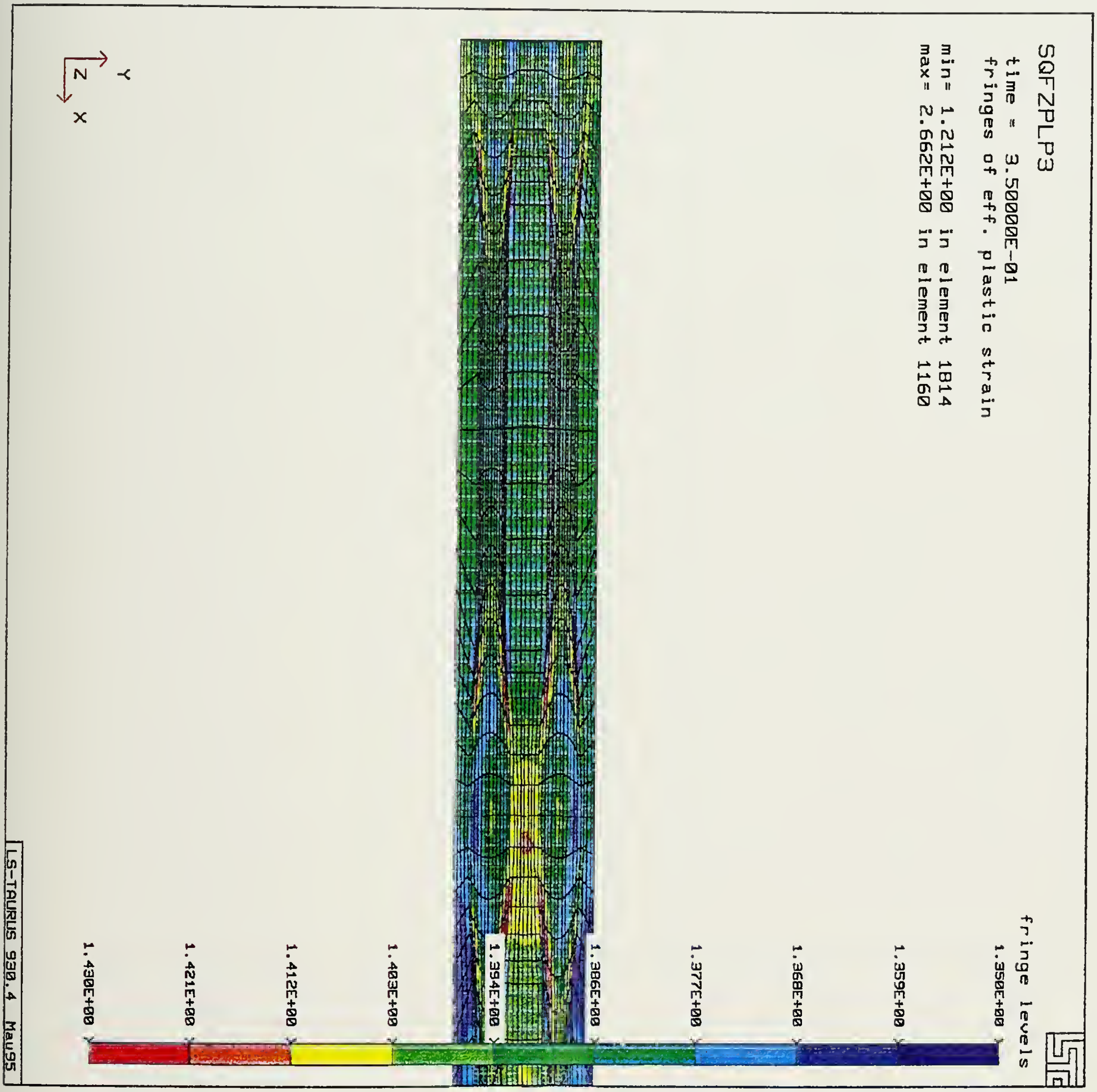

Figure B16: Fringe plot of Effective plastic strain for the square cluster arrangement in the hot worked intermediate strain rate model at a true strain of 1.20.

20:28:33.12/1/96

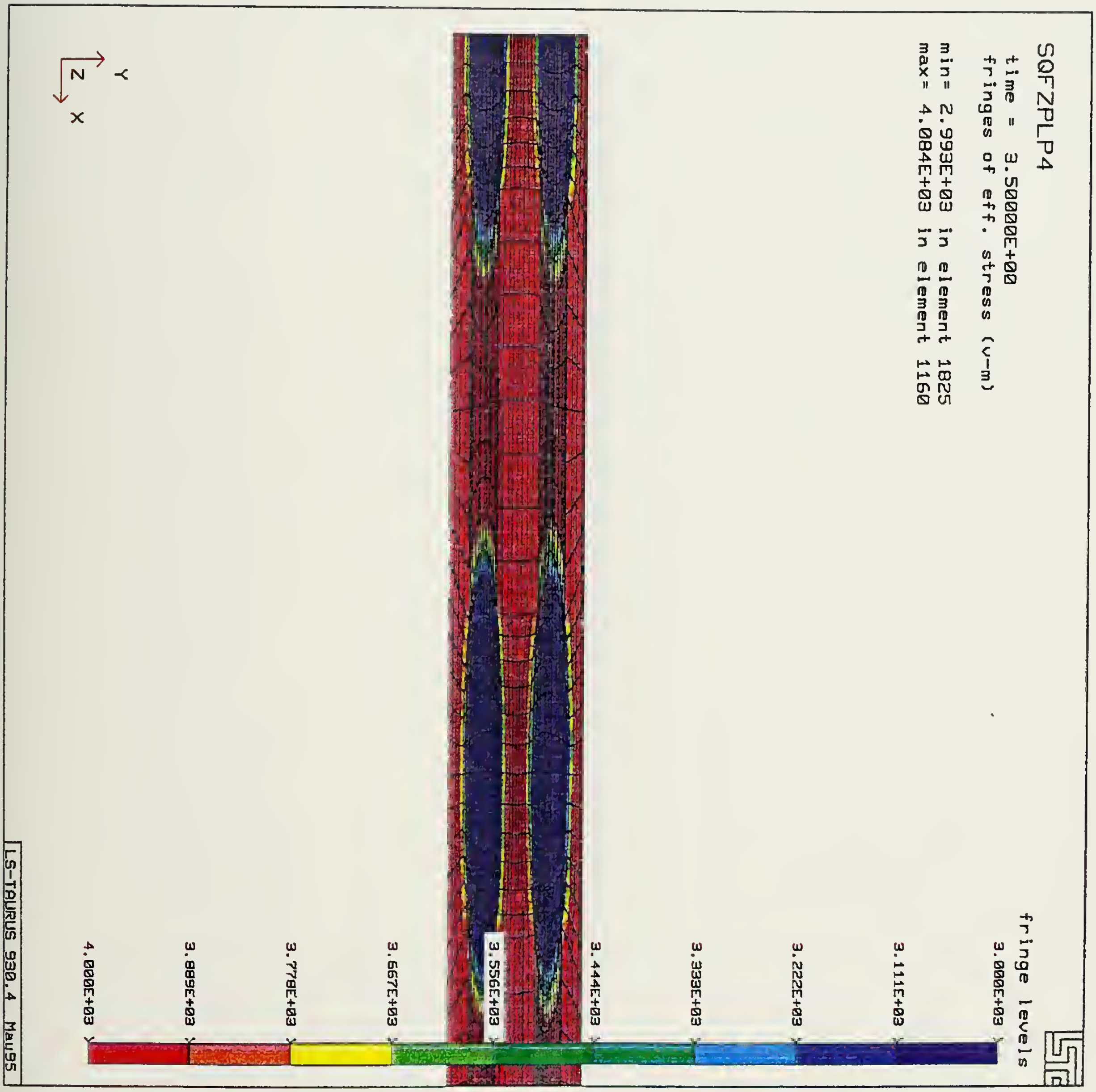

Figure B17: Fringe plot of Effective Von-Mises stress for the square cluster arrangement in the hot worked low strain rate model at a true strain of 1.20.

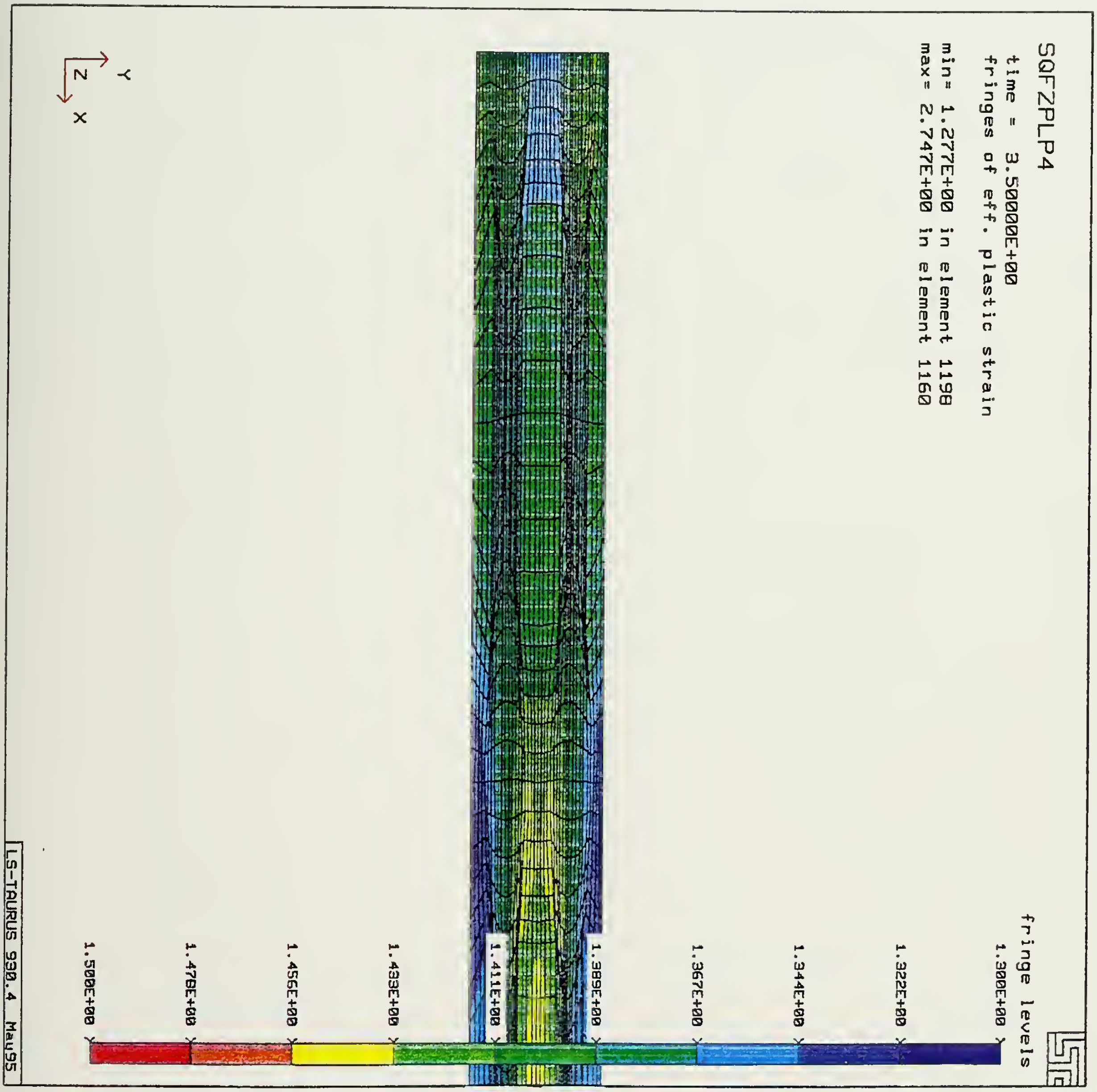

Figure B18: Fringe plot of Effective plastic strain for the square cluster arrangement in the hot worked low strain rate model at a true strain of 1.20.

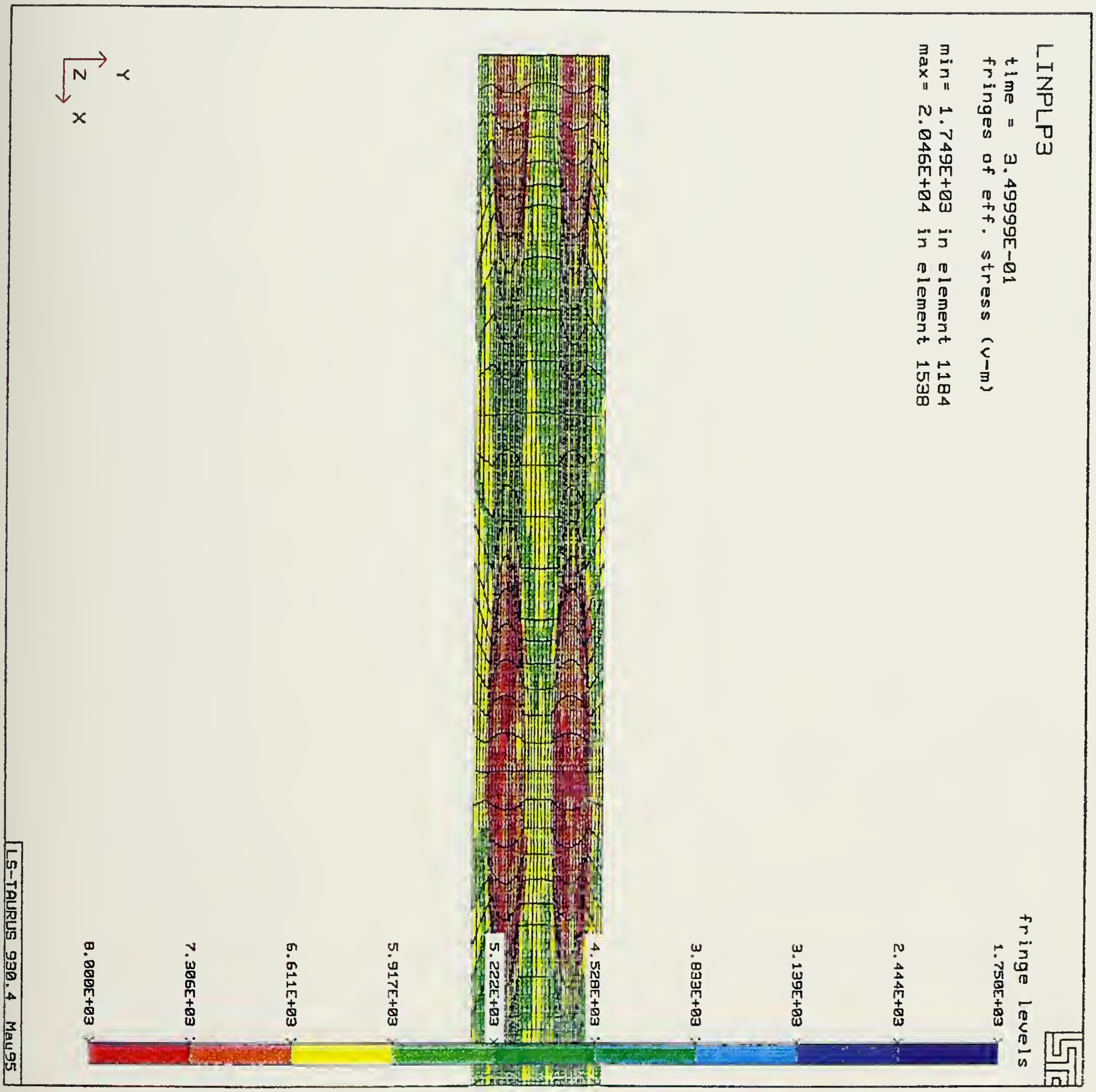

Figure B19: Fringe plot of Effective Von-Mises stress for the square cluster arrangement in the hot worked intermediate strain rate model using the linear law at a true strain of 1.20.

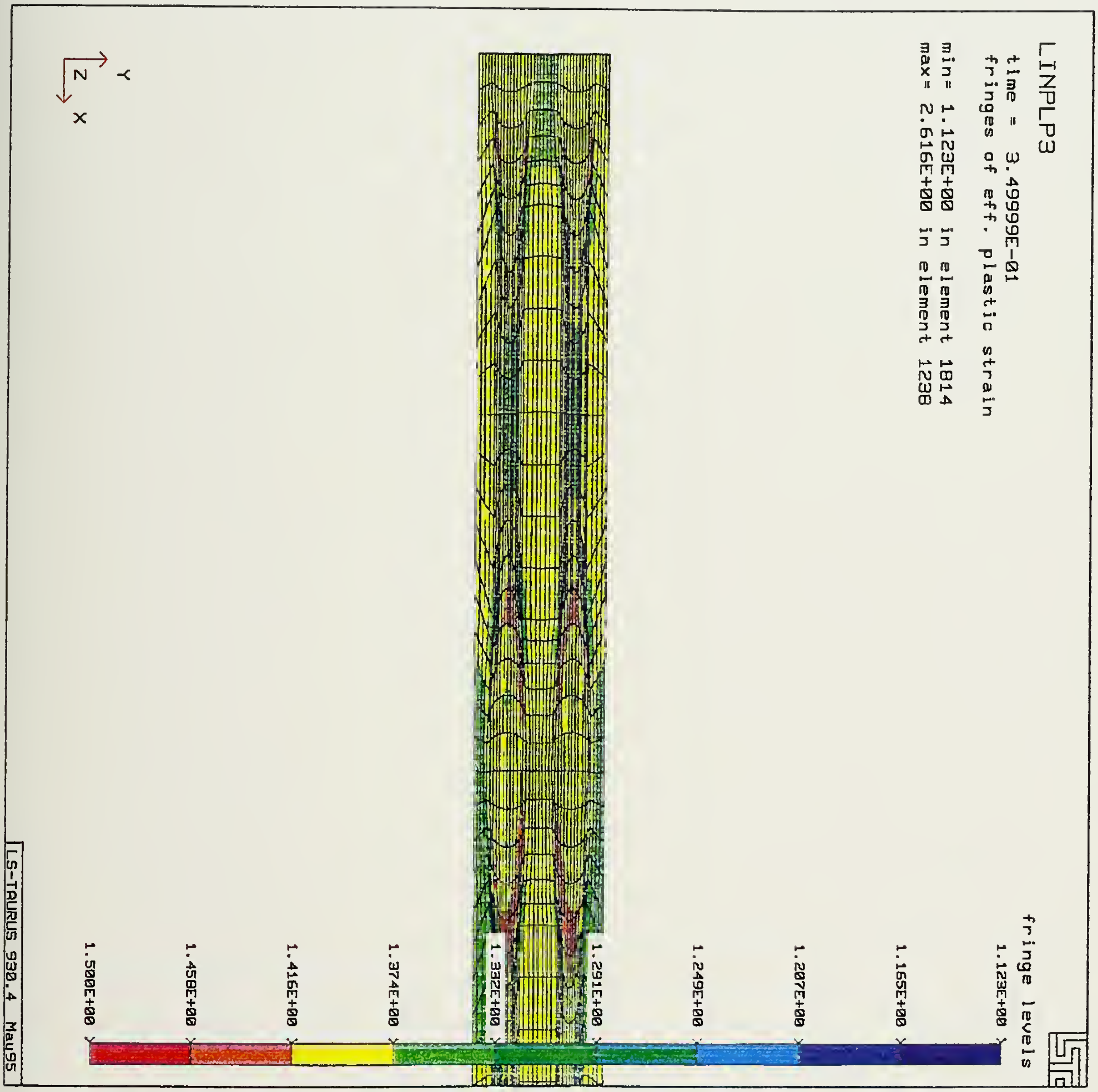

Figure B20: Fringe plot of Effective plastic strain for the square cluster arrangement in the hot worked intermediate strain rate model using the linear law at a true strain of 1.20.

2:37:11, 1/9/97

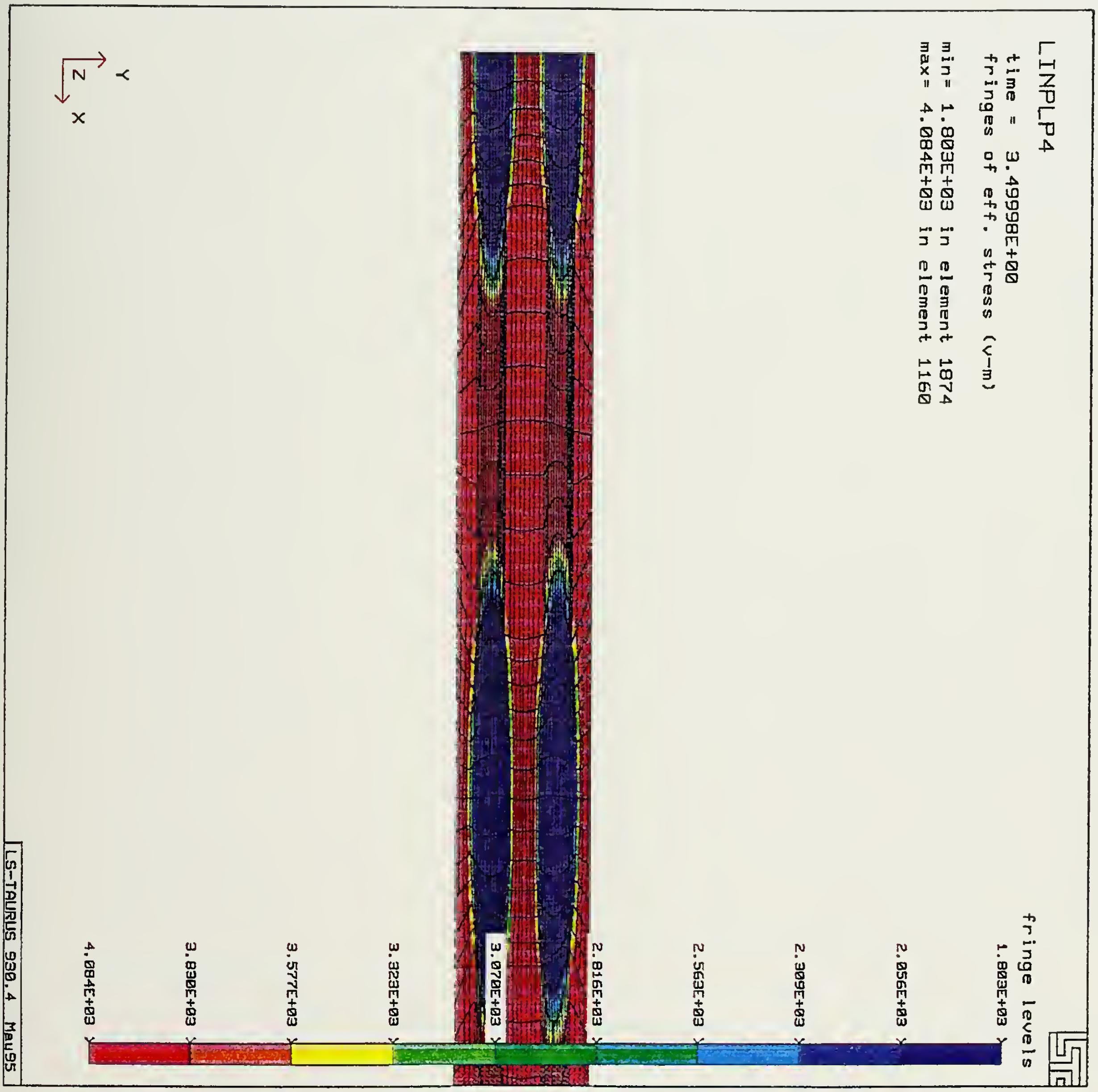

Figure B21: Fringe plot of Effective Von-Mises stress for the square cluster arrangement in the hot worked low strain rate model using the linear law at a true strain of 1.20.

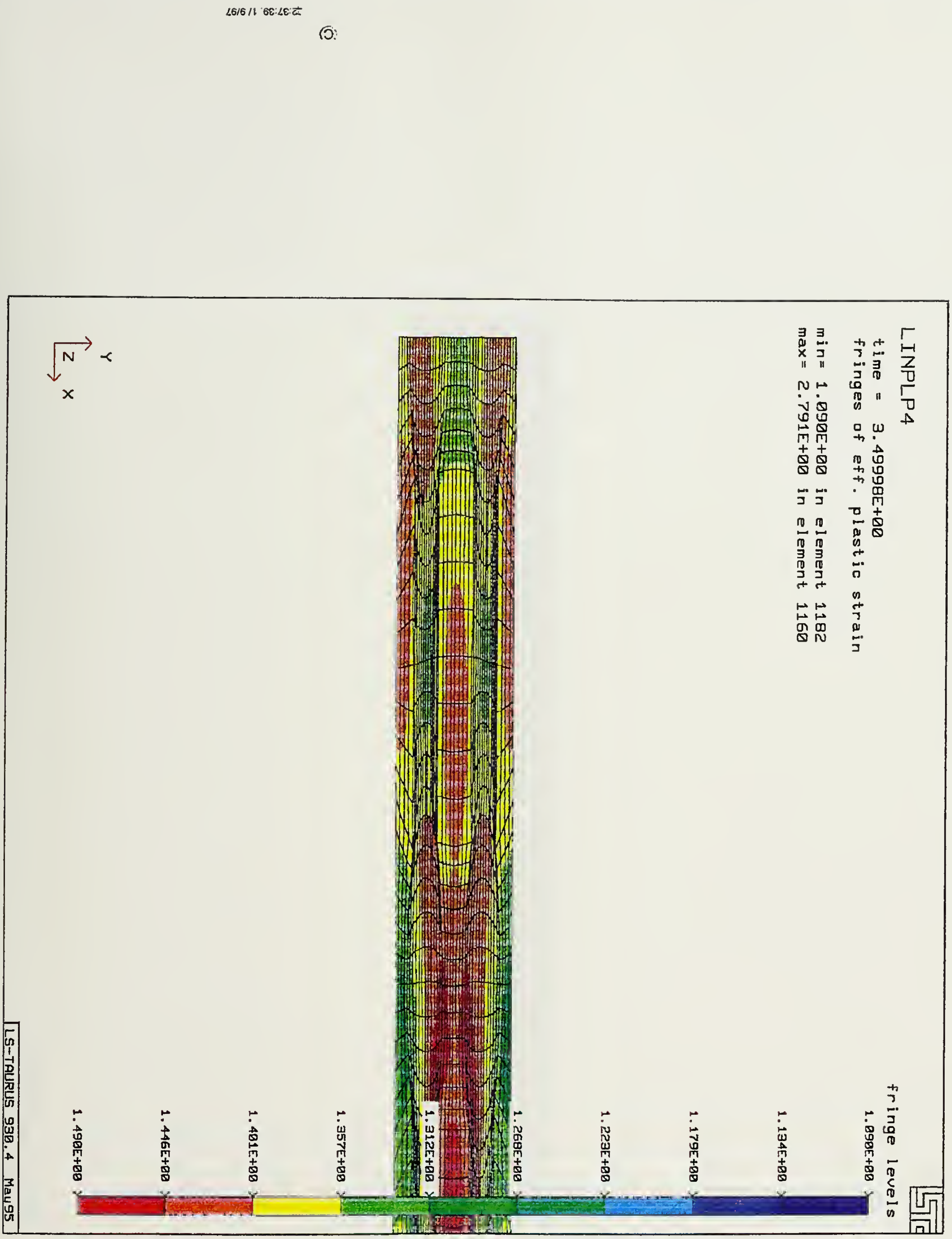

Figure B22: Fringe plot of Effective plastic strain for the square cluster arrangement in the hot worked low strain rate model using the linear law at a true strain of 1.20.

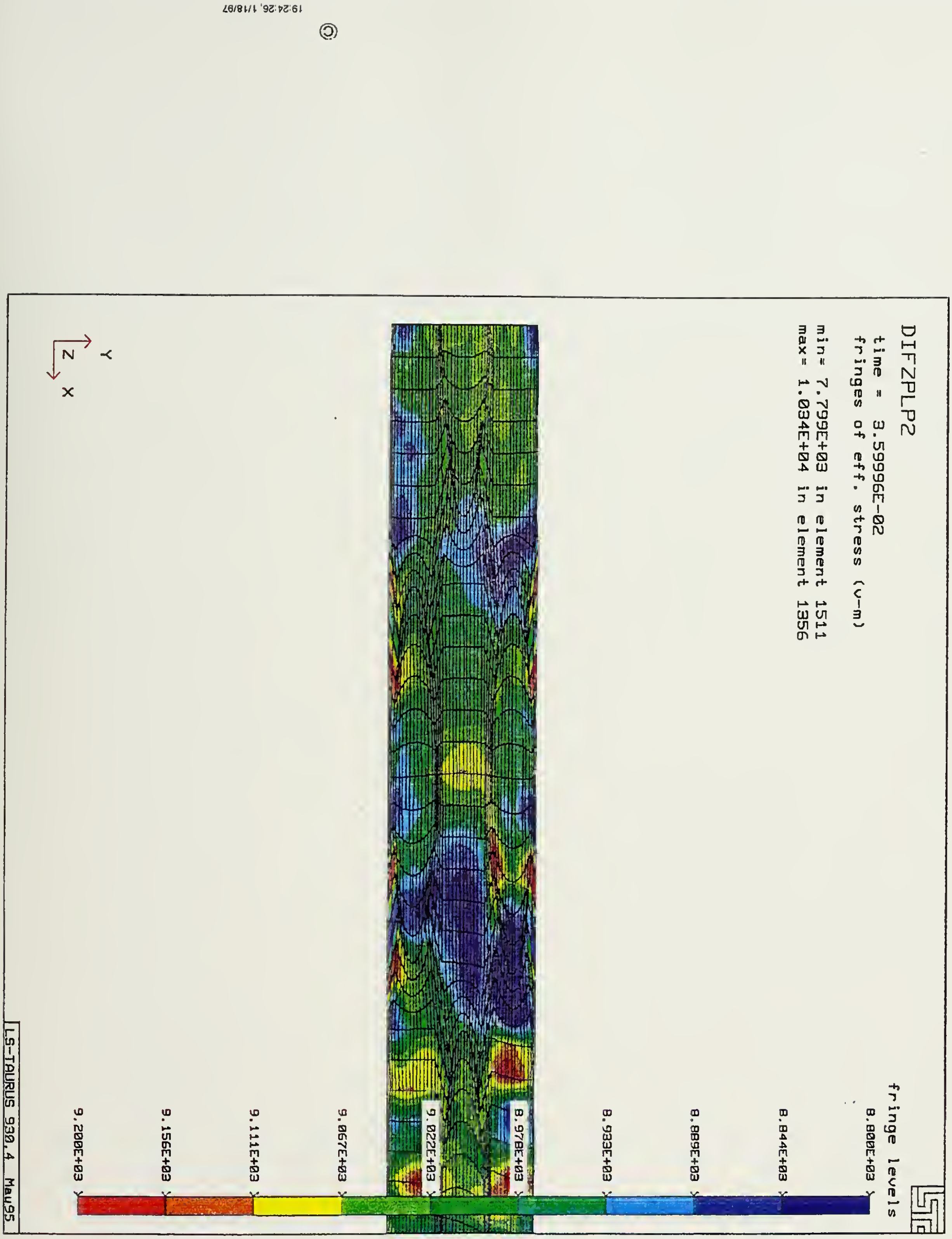

Figure B23: Fringe plot of Effective Von-Mises stress for the diamond cluster arrangement in the hot worked high strain rate model at a true strain of 1.13.

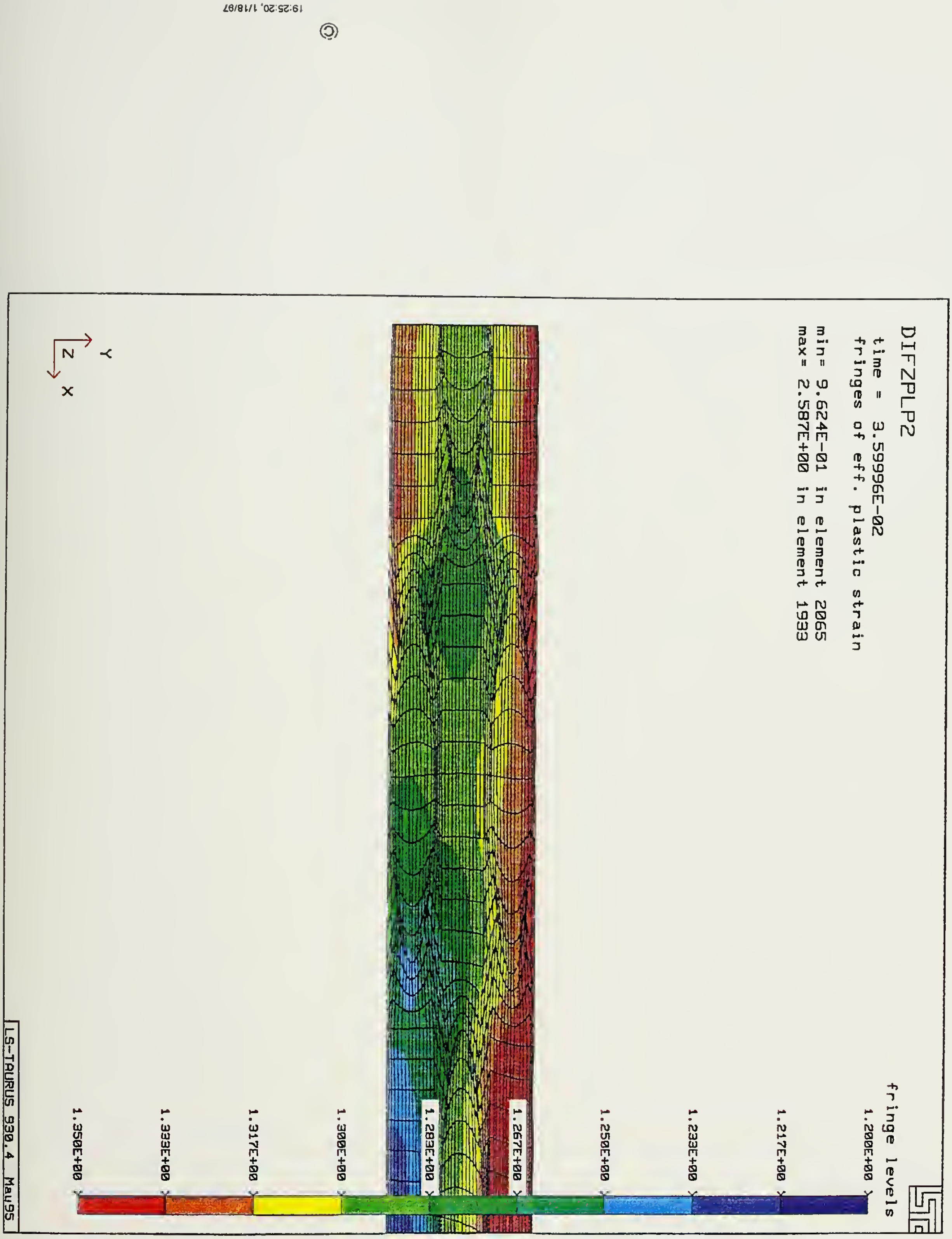

Figure B24: Fringe plot of Effective plastic strain for the diamond cluster arrangement in the hot worked high strain rate model at a true strain of 1.13.

20:43:22,12/1/96

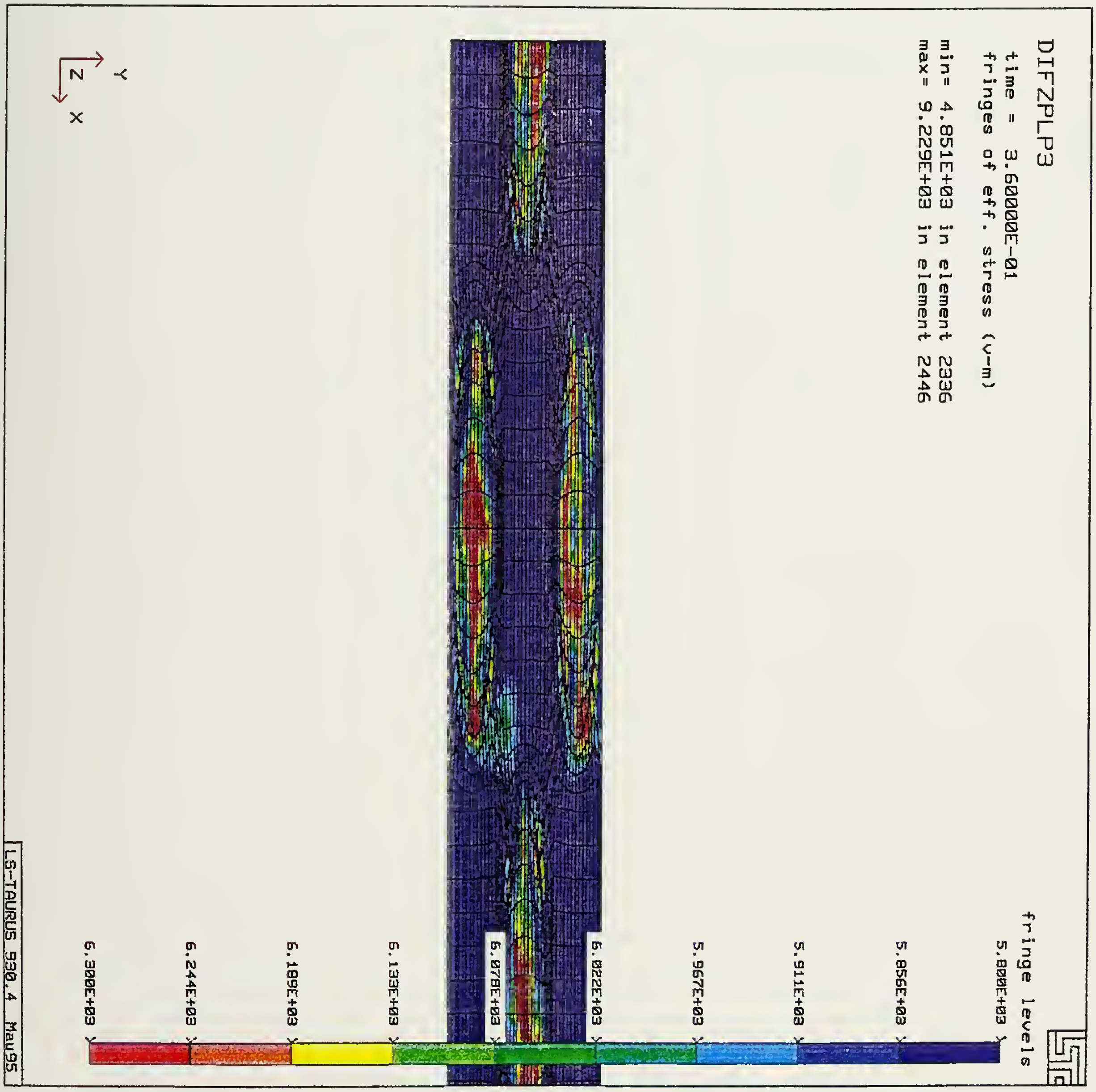

Figure B25: Fringe plot of Effective Von-Mises stress for the diamond cluster arrangement in the hot worked intermediate strain rate model at a true strain of 1.13.

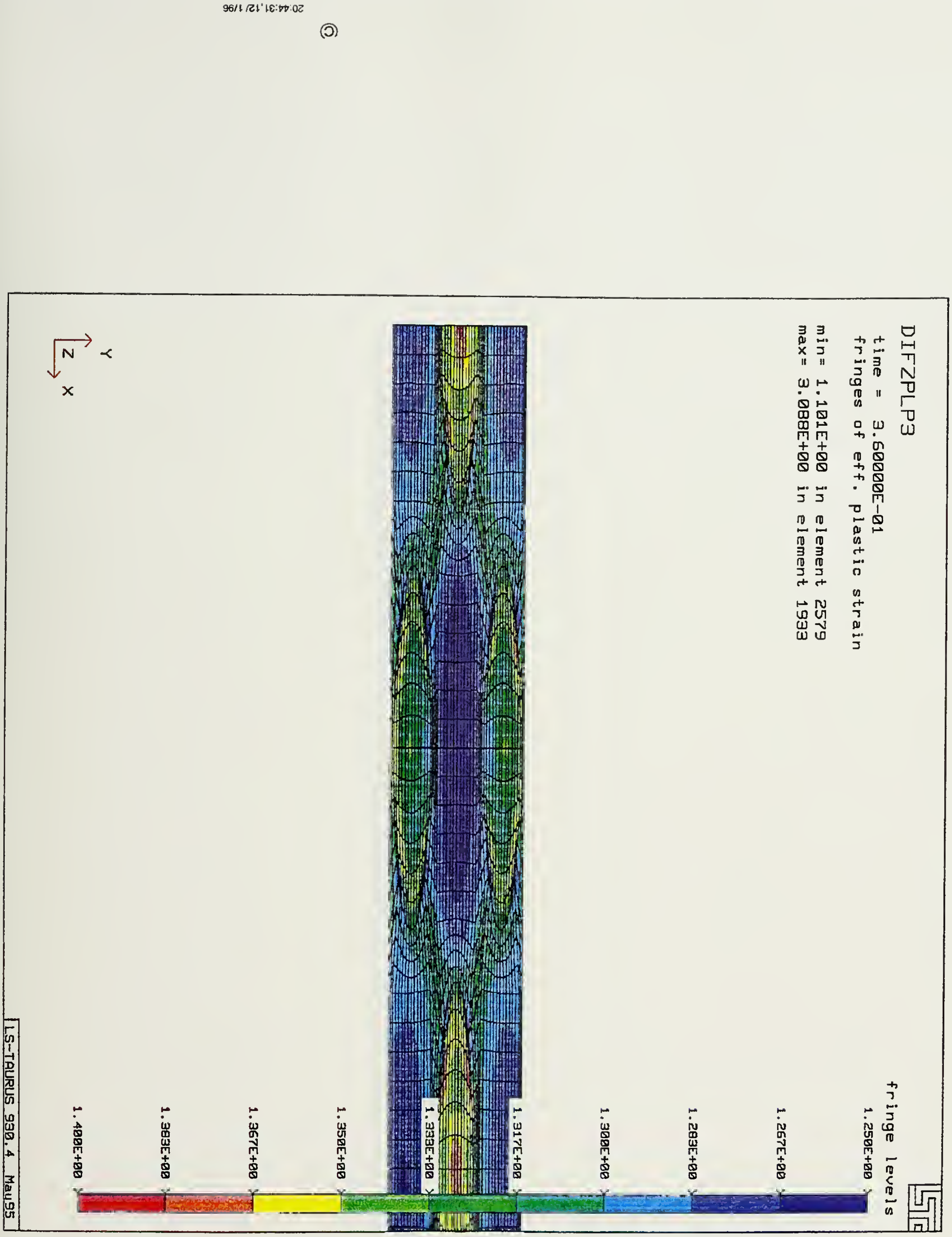

Figure B26: Fringe plot of Effective plastic strain for the diamond cluster arrangement in the hot worked intermediate strain rate model at a true strain of 1.13.

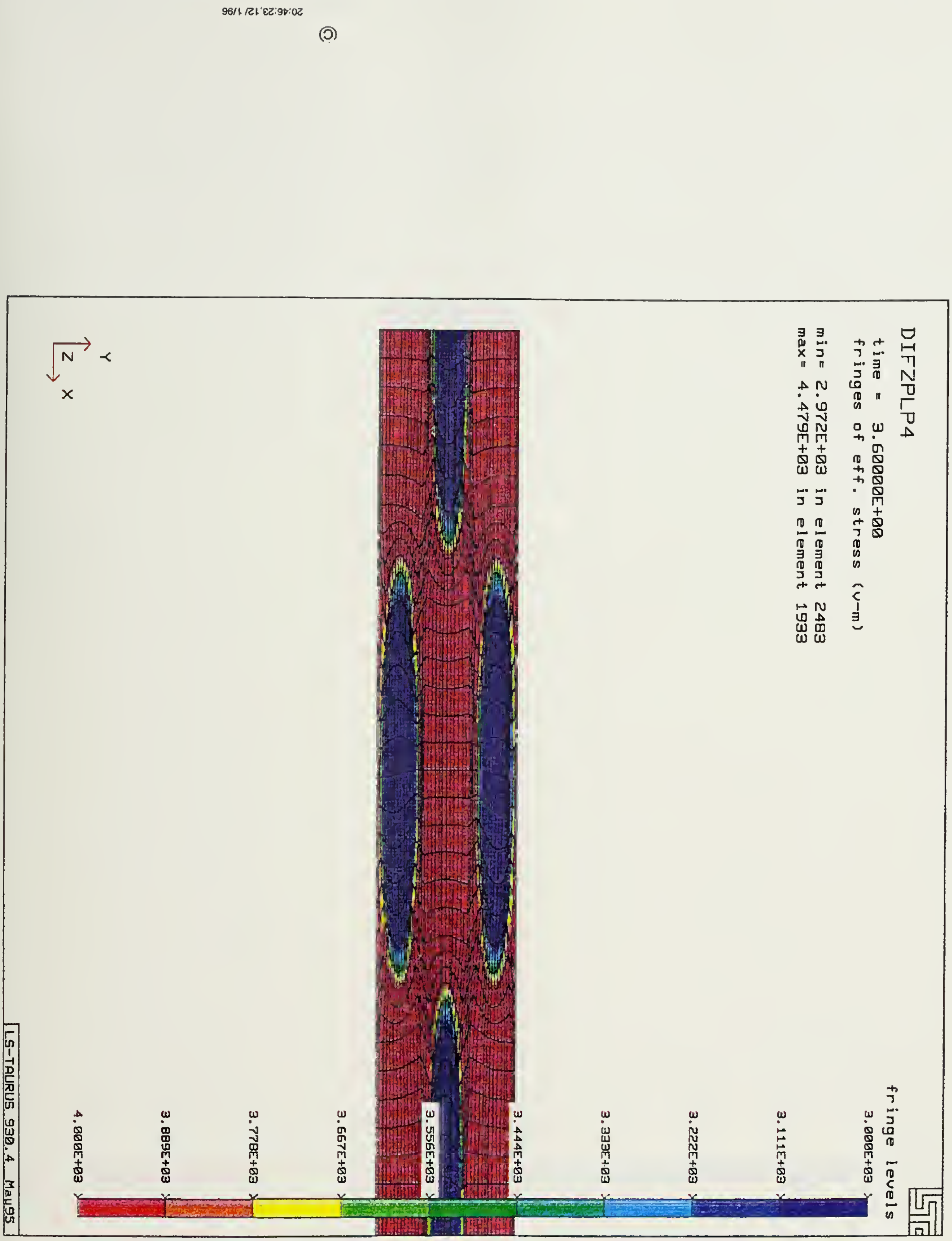

Figure B27: Fringe plot of Effective Von-Mises stress for the diamond cluster arrangement in the hot worked low strain rate model at a true strain of 1.13.

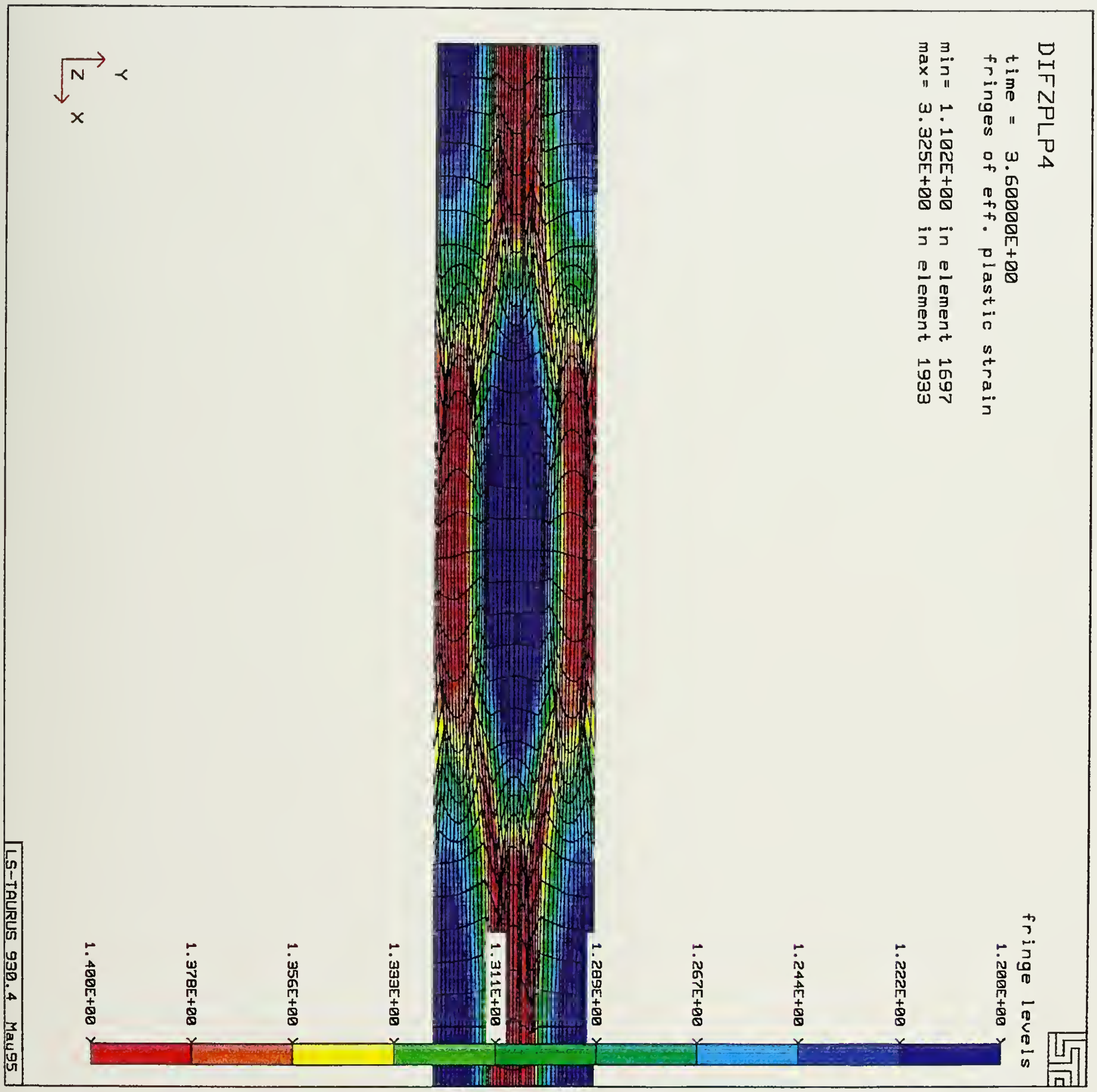

Figure B28: Fringe plot of Effective plastic strain for the diamond cluster arrangement in the hot worked low strain rate model at a true strain of 1.13.

APPENDIX C: FRINGE PLOTS OF EFFECTIVE VON MISES STRESS AND EFFECTIVE PLASTIC STRAIN FOR ALL DISCRETE MODELS

22:16:41, 1/9/97

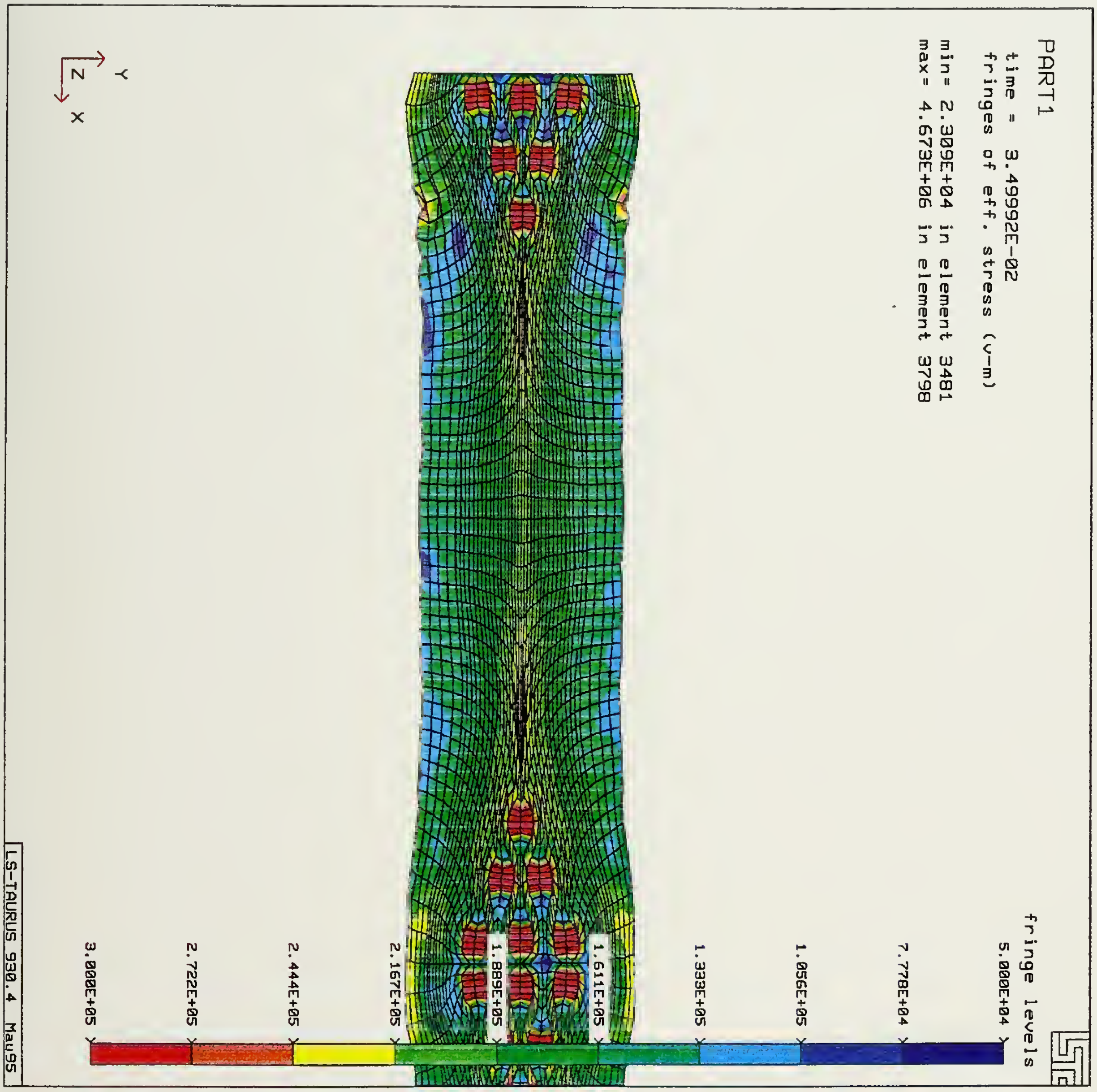

Figure C1: Fringe plot of Effective Von-Mises stress for the discrete cold worked model, with a local volume fraction of 25%, at a true strain of 1.20.

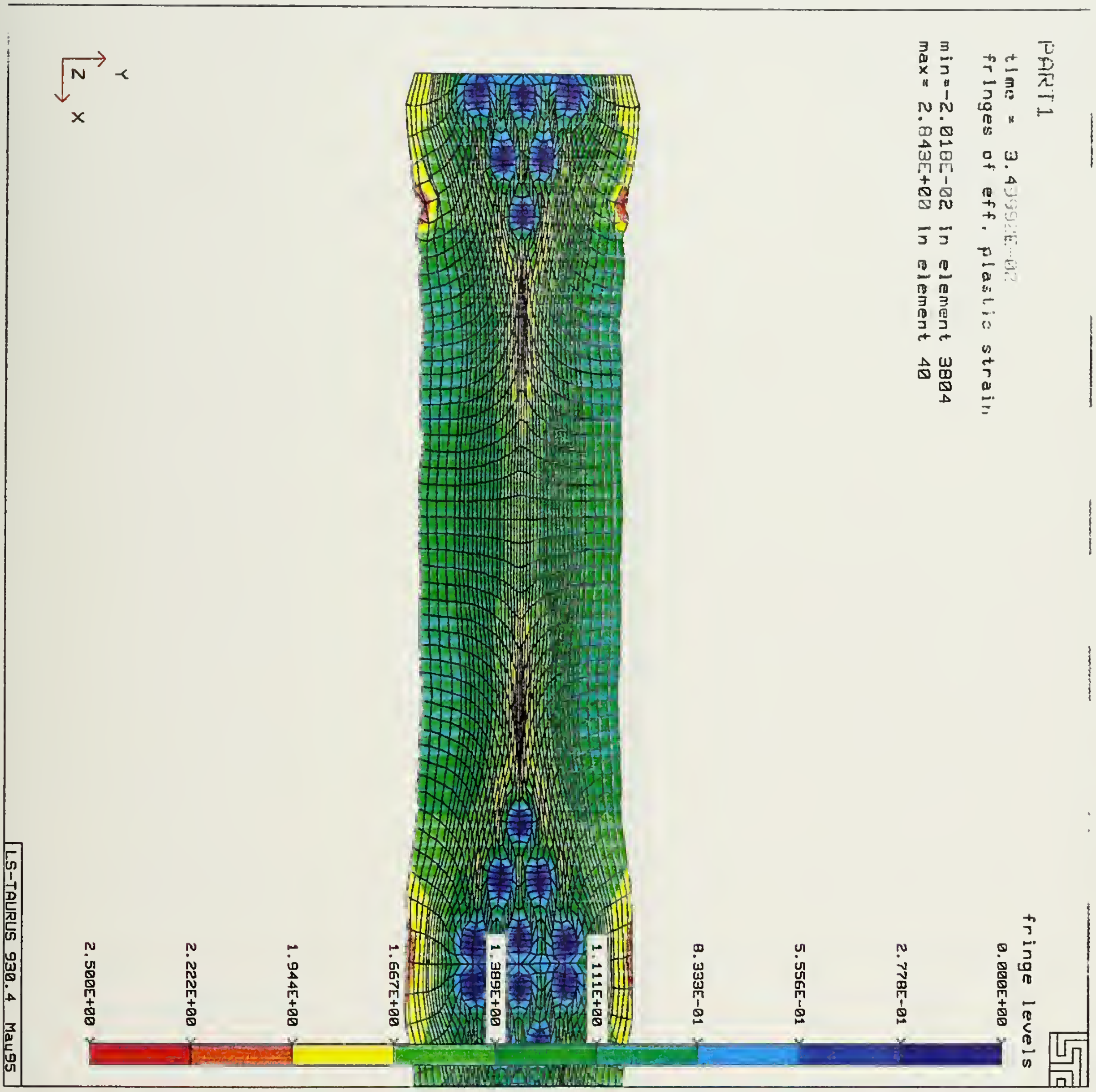

Figure C2: Fringe plot of Effective plastic strain for the discrete cold worked model, with a local volume fraction of 25%, at a true strain of 1.20.

12:17:56 1/9/97

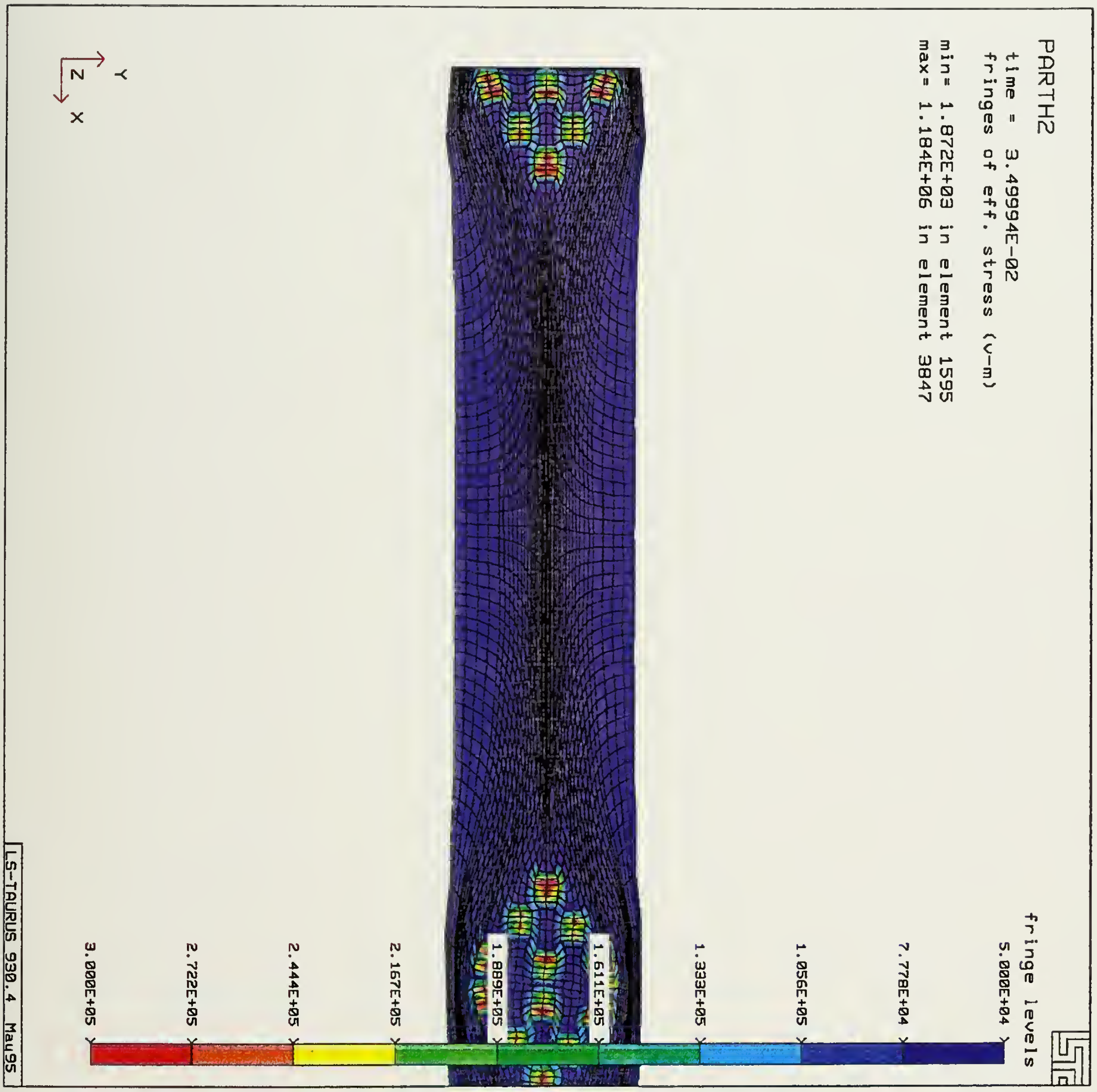

Figure C3: Fringe plot of Effective Von-Mises stress for the discrete hot worked high strain rate model, with a local volume fraction of 25%, at a true strain of 1.20.

12:18:18, 1/9/97

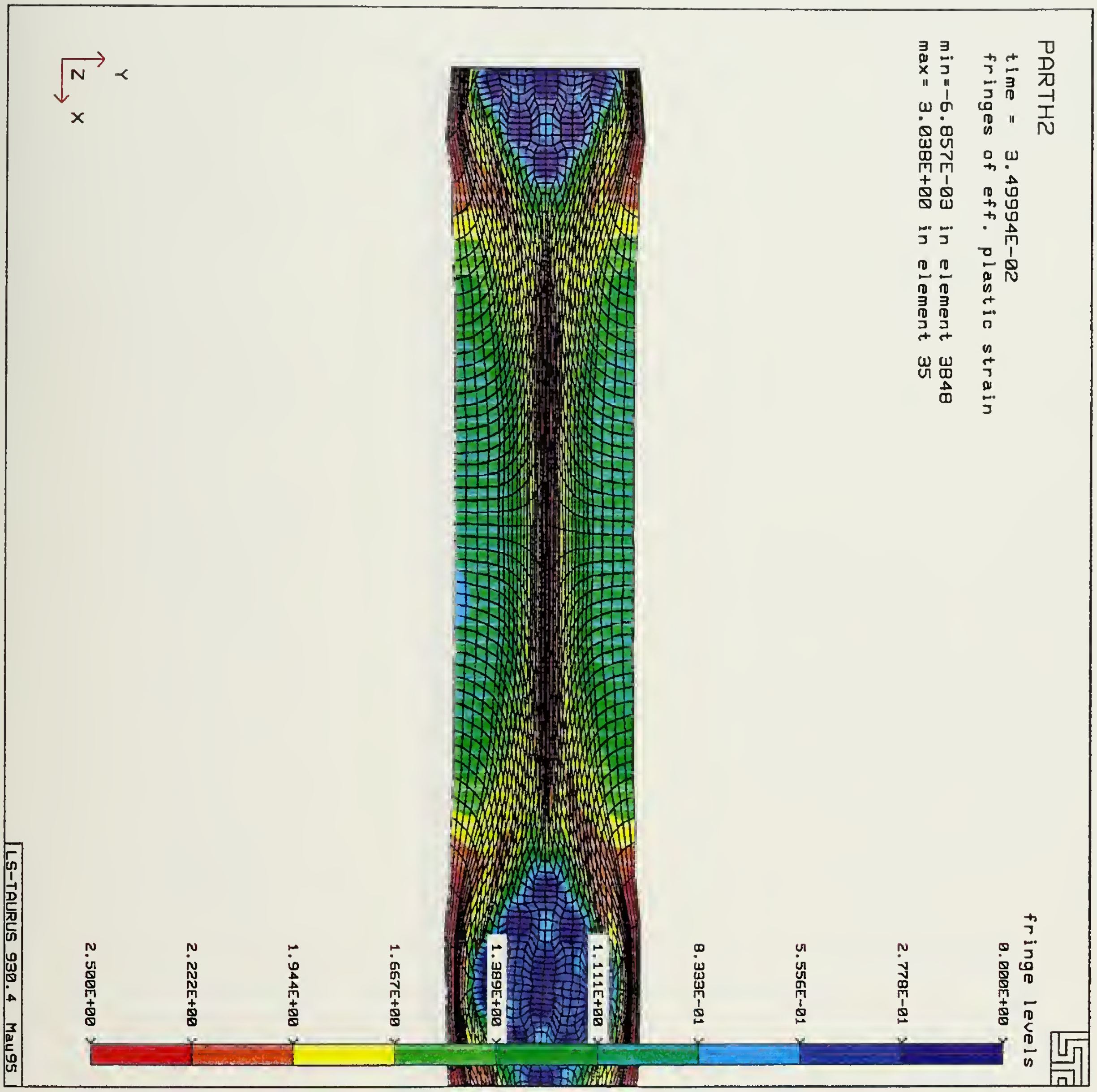

Figure C4: Fringe plot of Effective plastic strain for the discrete hot worked high strain rate model, with a local volume fraction of 25%, at a true strain of 1.20.

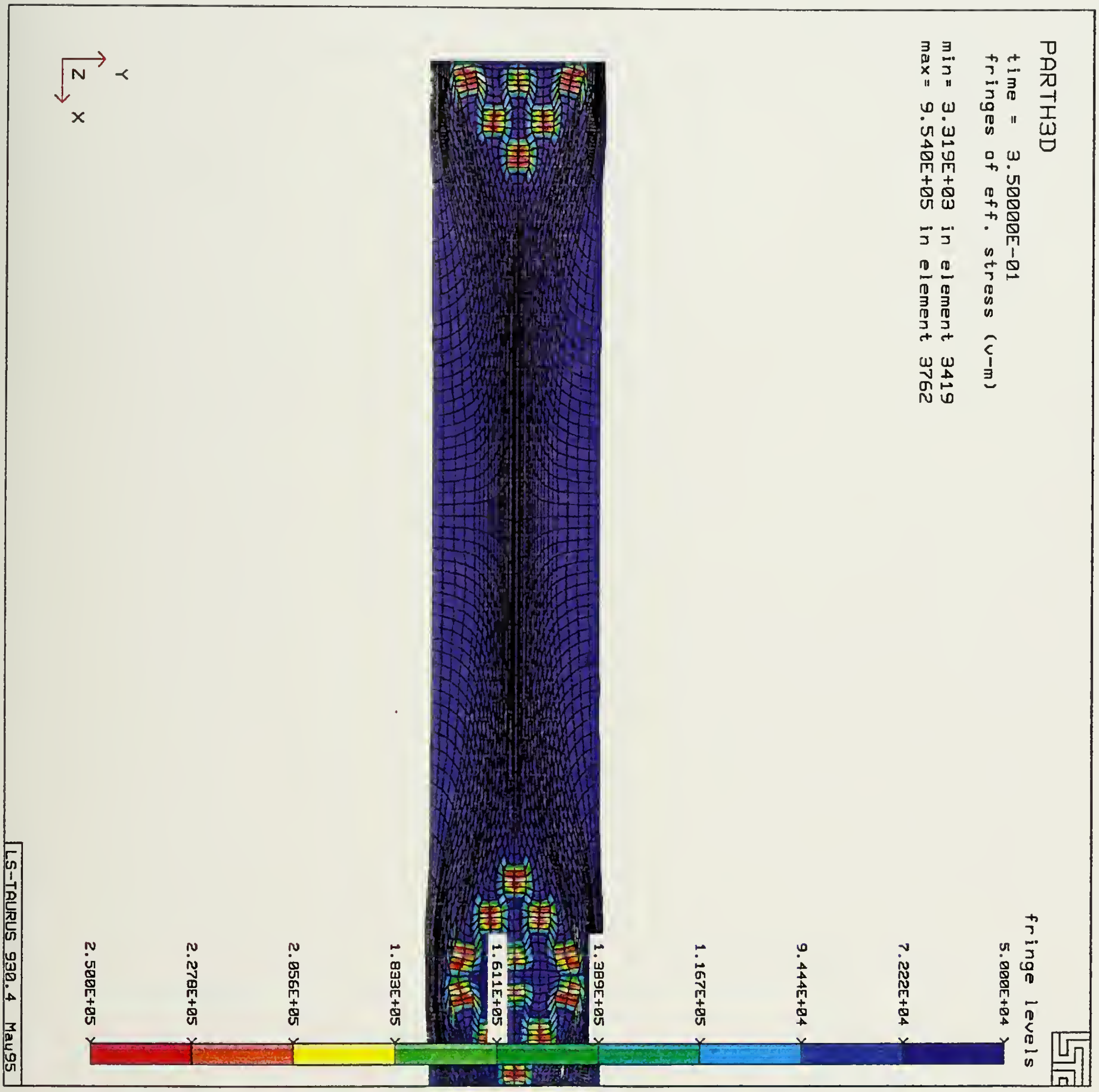

Figure C5: Fringe plot of Effective Von-Mises stress for the discrete hot worked intermediate strain rate model, with a local volume fraction of 25%, at a true strain of 1.20.

12:19:31 1/9/97

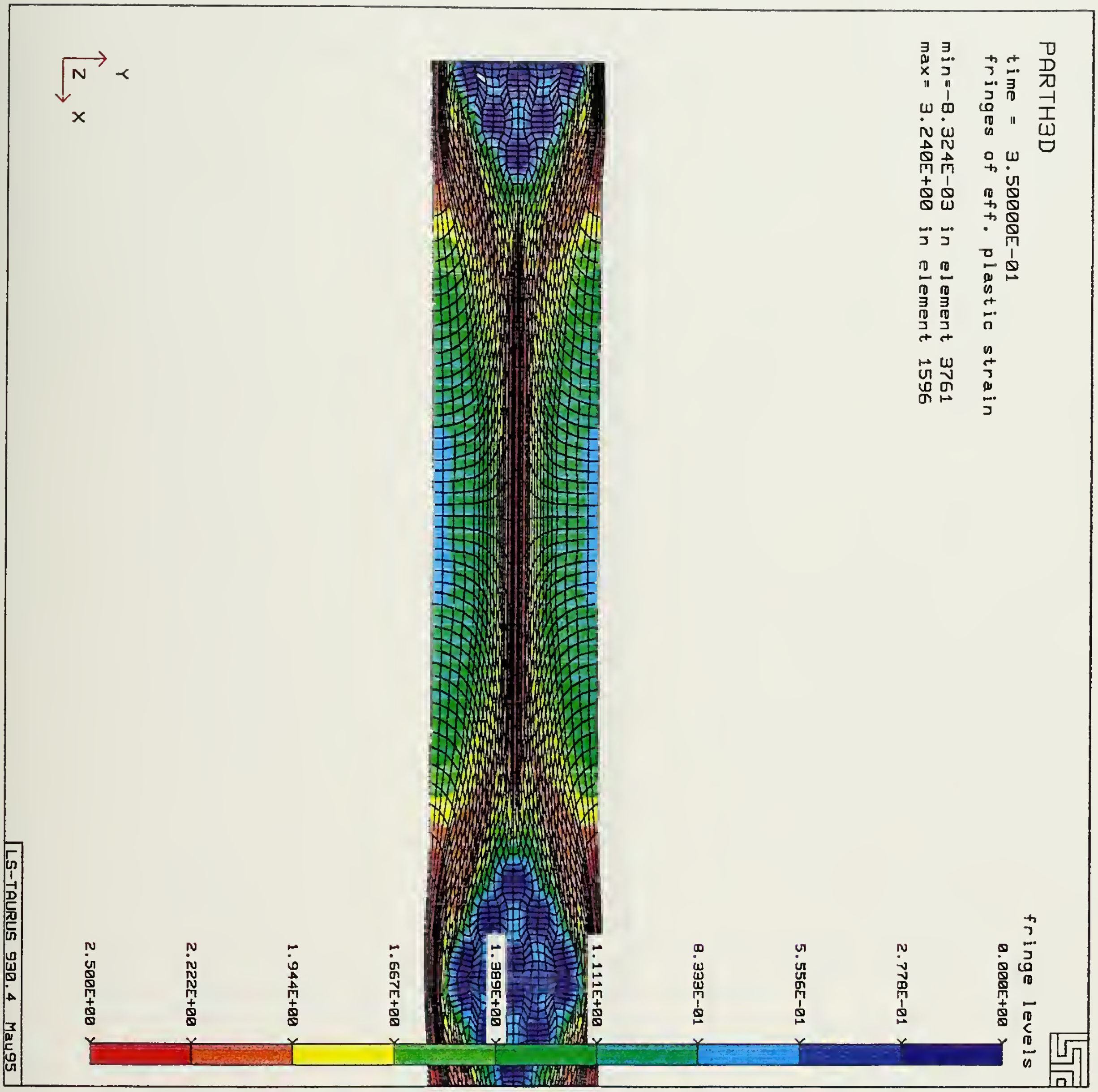

Figure C6: Fringe plot of Effective plastic strain for the discrete hot worked intermediate strain rate model, with a local volume fraction of 25%, at a true strain of 1.20.

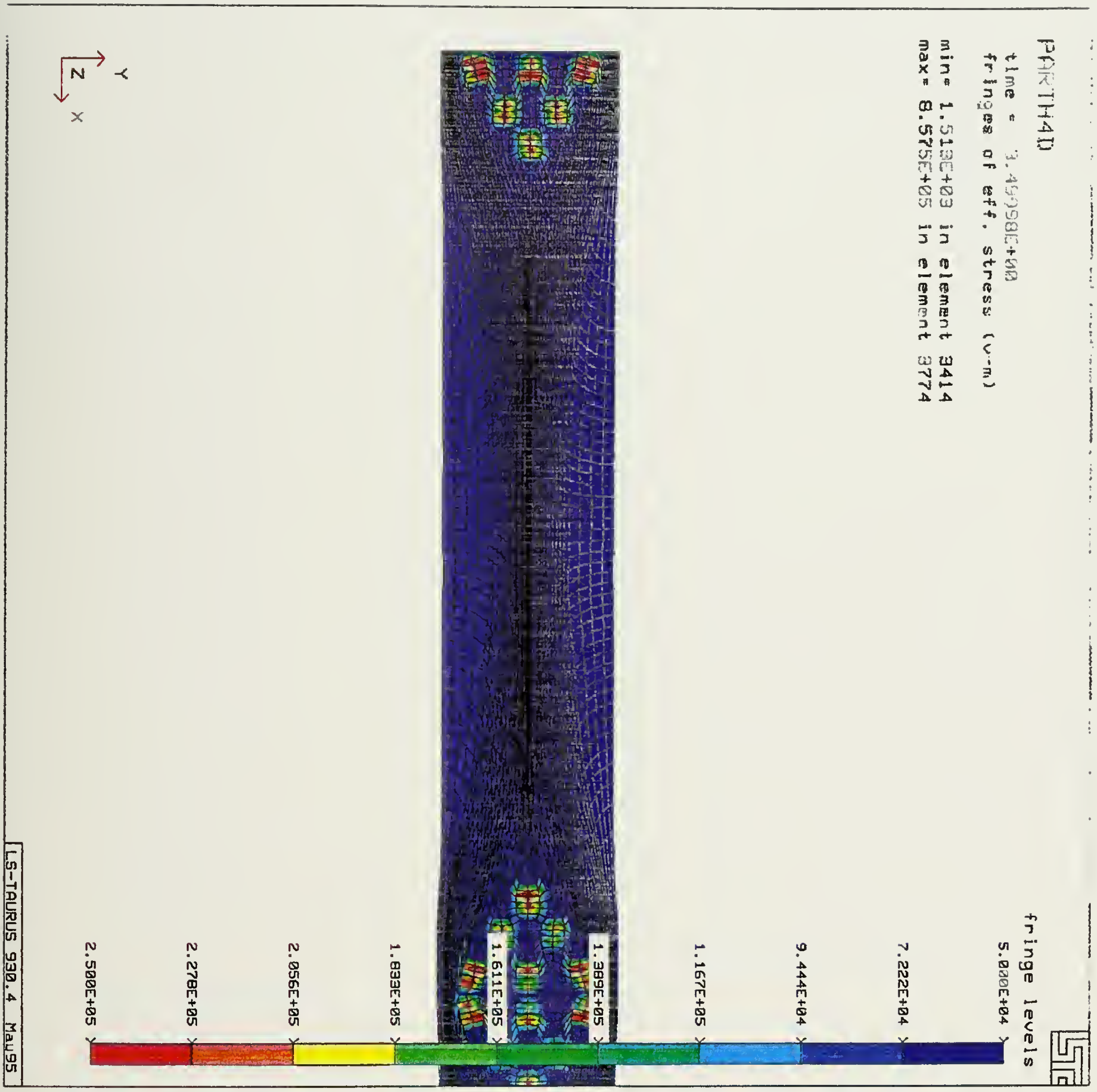

Figure C7: Fringe plot of Effective Von-Mises stress for the discrete hot worked low strain rate model, with a local volume fraction of 25%, at a true strain of 1.20.

22:22:37, 1/9/97

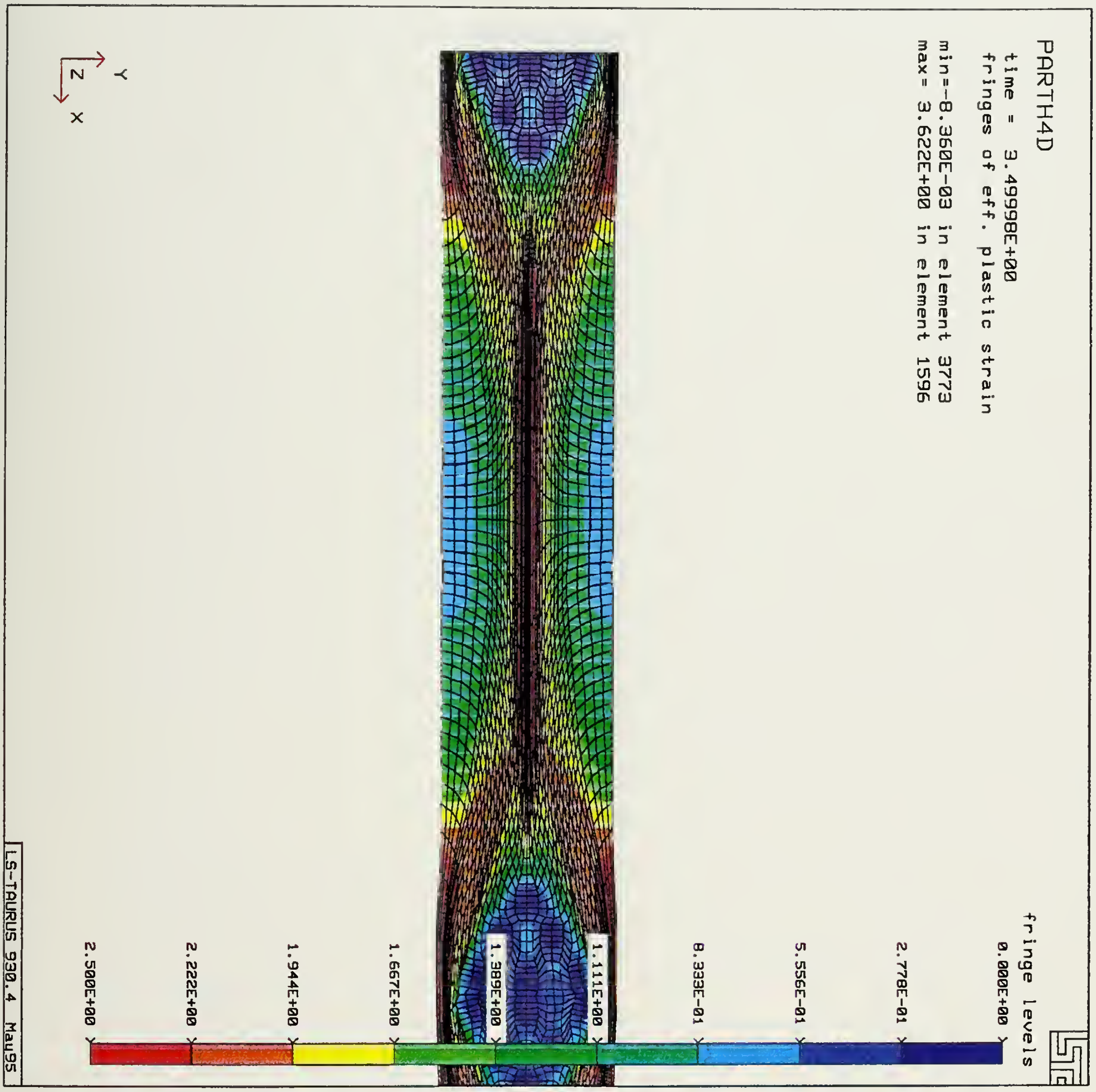

Figure C8: Fringe plot of Effective plastic strain for the discrete hot worked low strain rate model, with a local volume fraction of 25%, at a true strain of 1.20.

Figure C9: Fringe plot of Effective Von-Mises stress for the discrete hot worked intermediate strain rate model, with a local volume fraction of 4%, at a true strain of 1.20.

19:34:23, 1/18/97

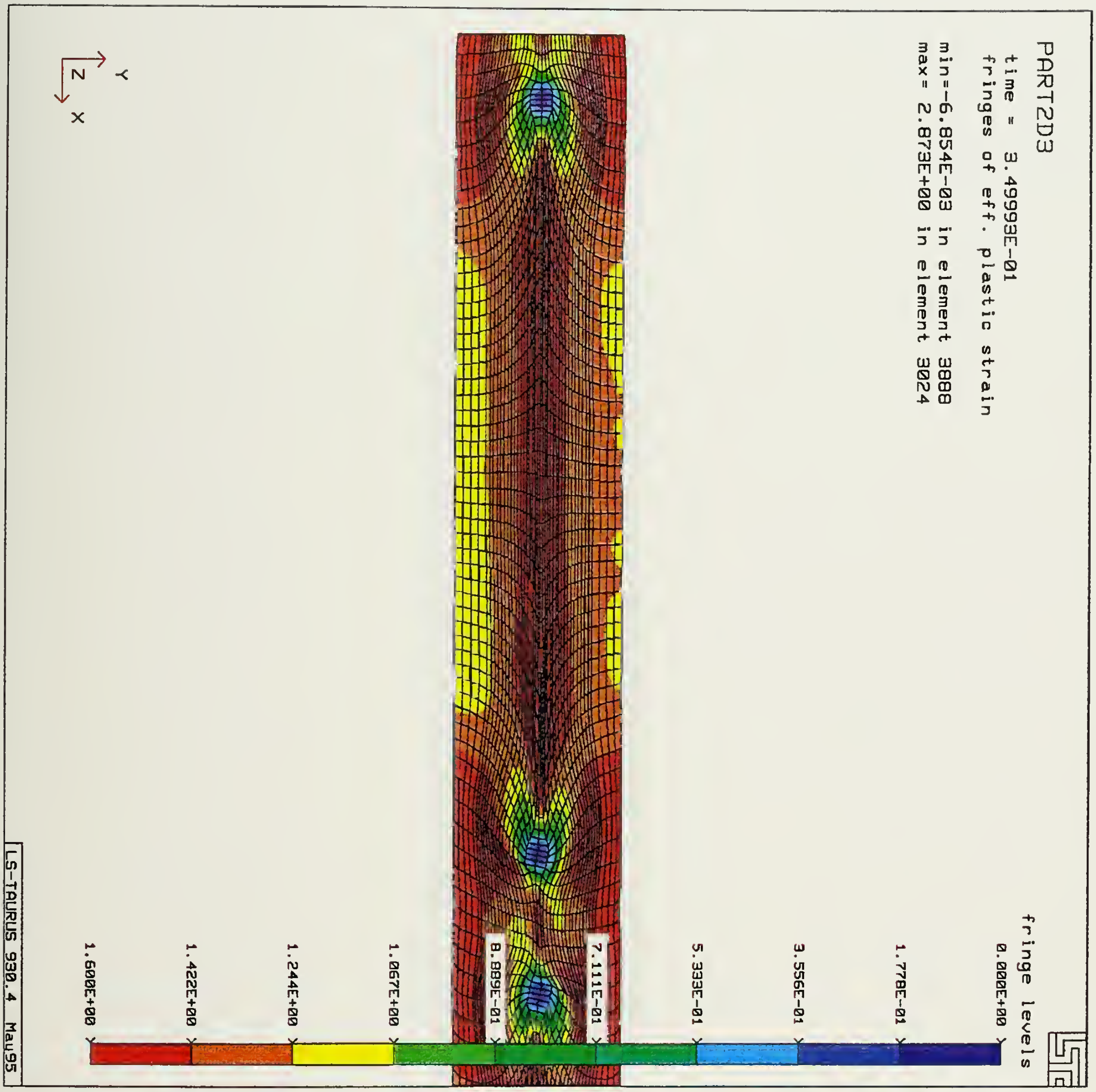

Figure C10: Fringe plot of Effective plastic strain for the discrete hot worked intermediate strain rate model, with a local volume fraction of 4%, at a true strain of 1.20.

15:55:11, 1/19/97

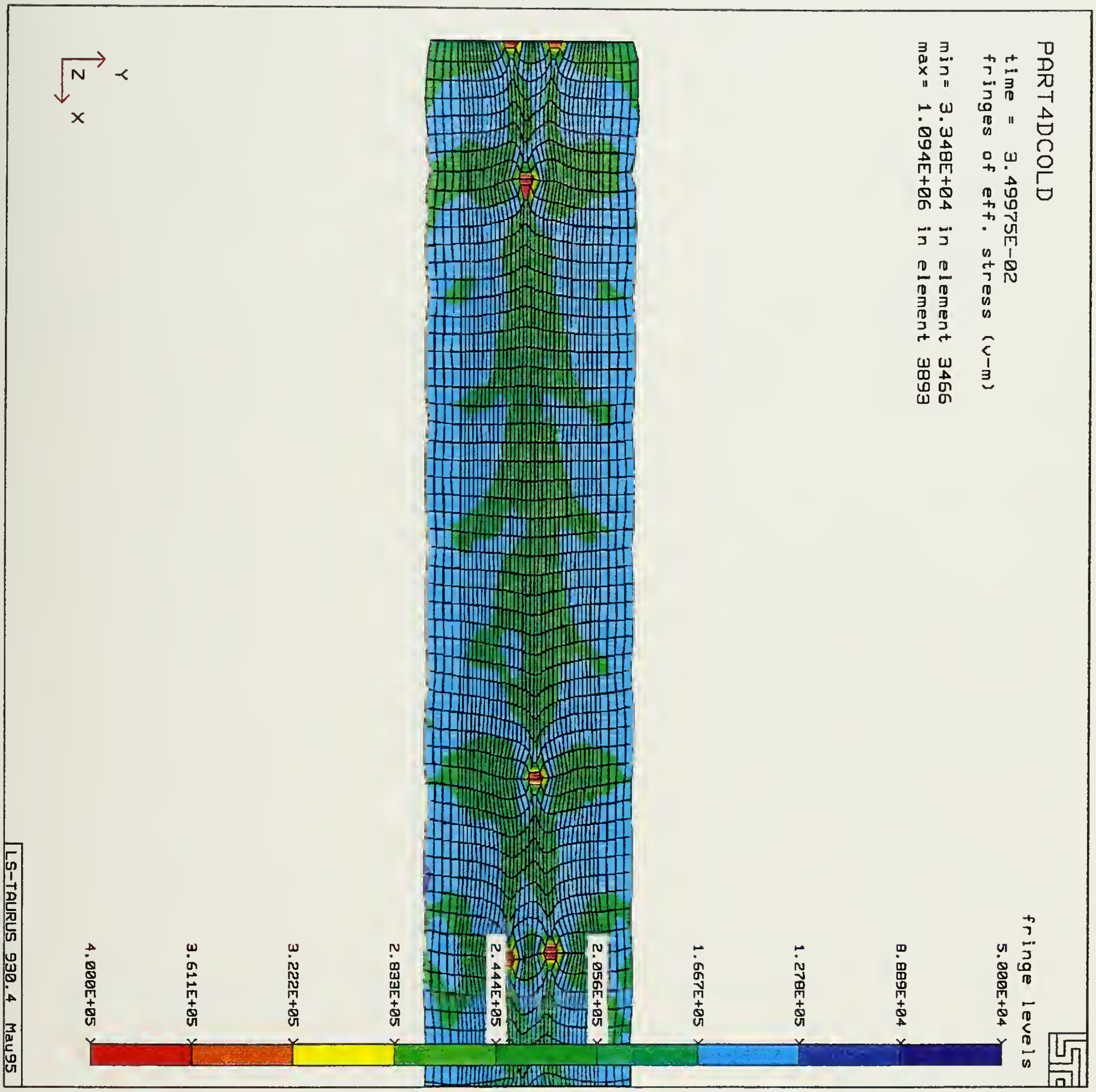

Figure C11: Fringe plot of Effective Von-Mises stress for the discrete cold worked model, with a local volume fraction of 2%, at a true strain of 1.20.

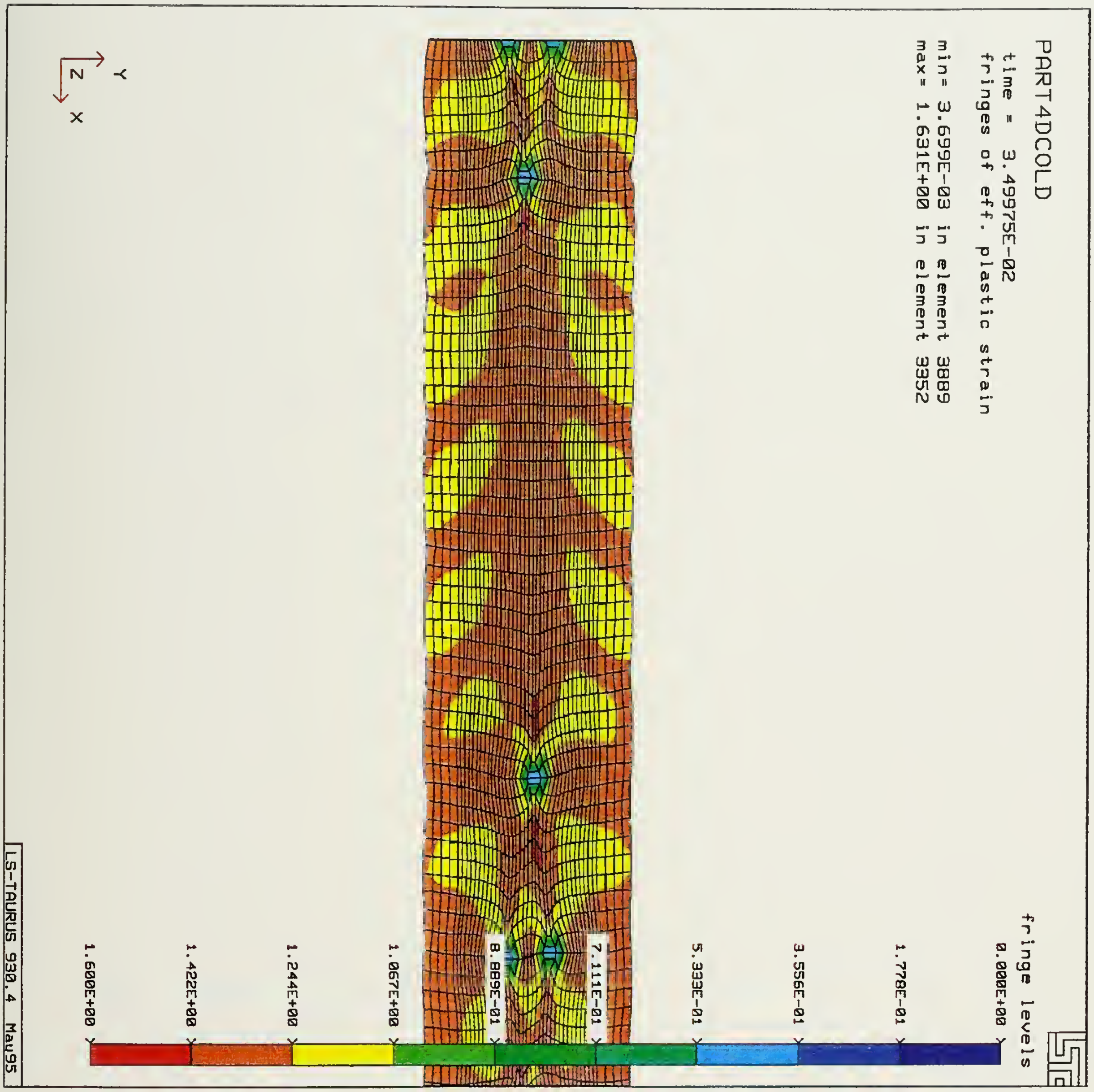

Figure C12: Fringe plot of Effective plastic strain for the discrete cold worked model, with a local volume fraction of 2%, at a true strain of 1.20.

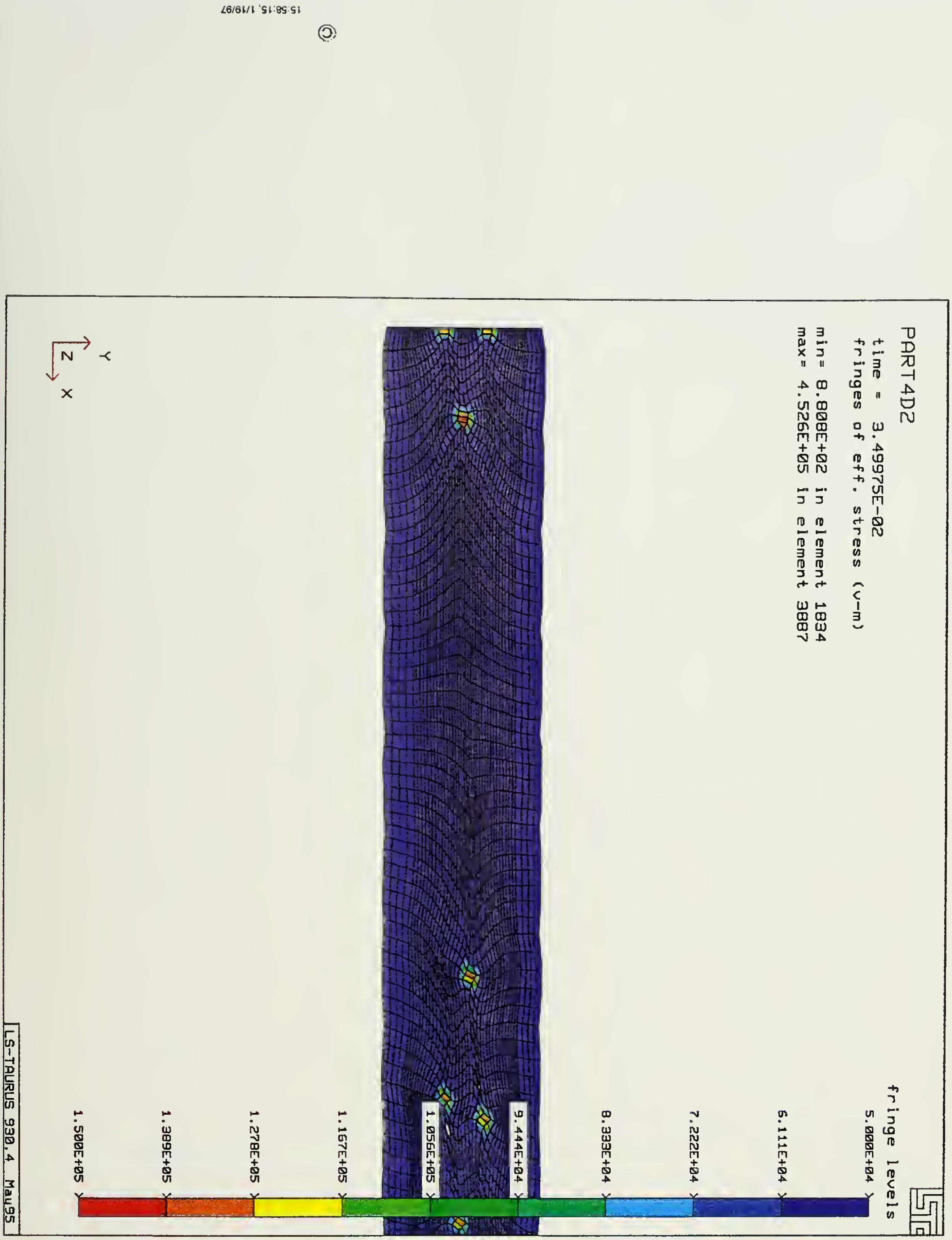

Figure C13: Fringe plot of Effective Von-Mises stress for the discrete hot worked high strain rate model, with a local volume fraction of 2%, at a true strain of 1.20.

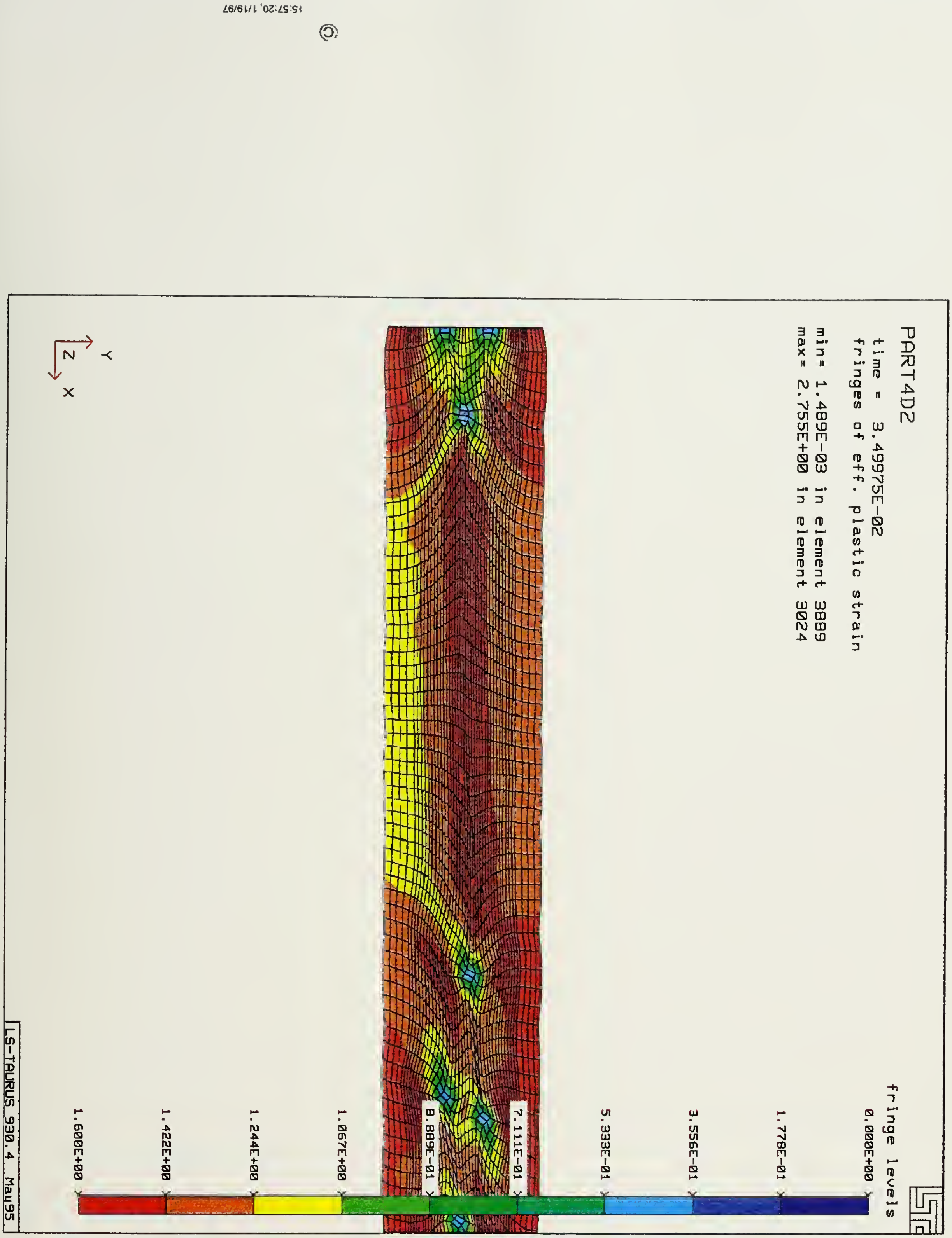

Figure C14: Fringe plot of Effective plastic strain for the discrete hot worked high strain rate model, with a local volume fraction of 2%, at a true strain of 1.20.

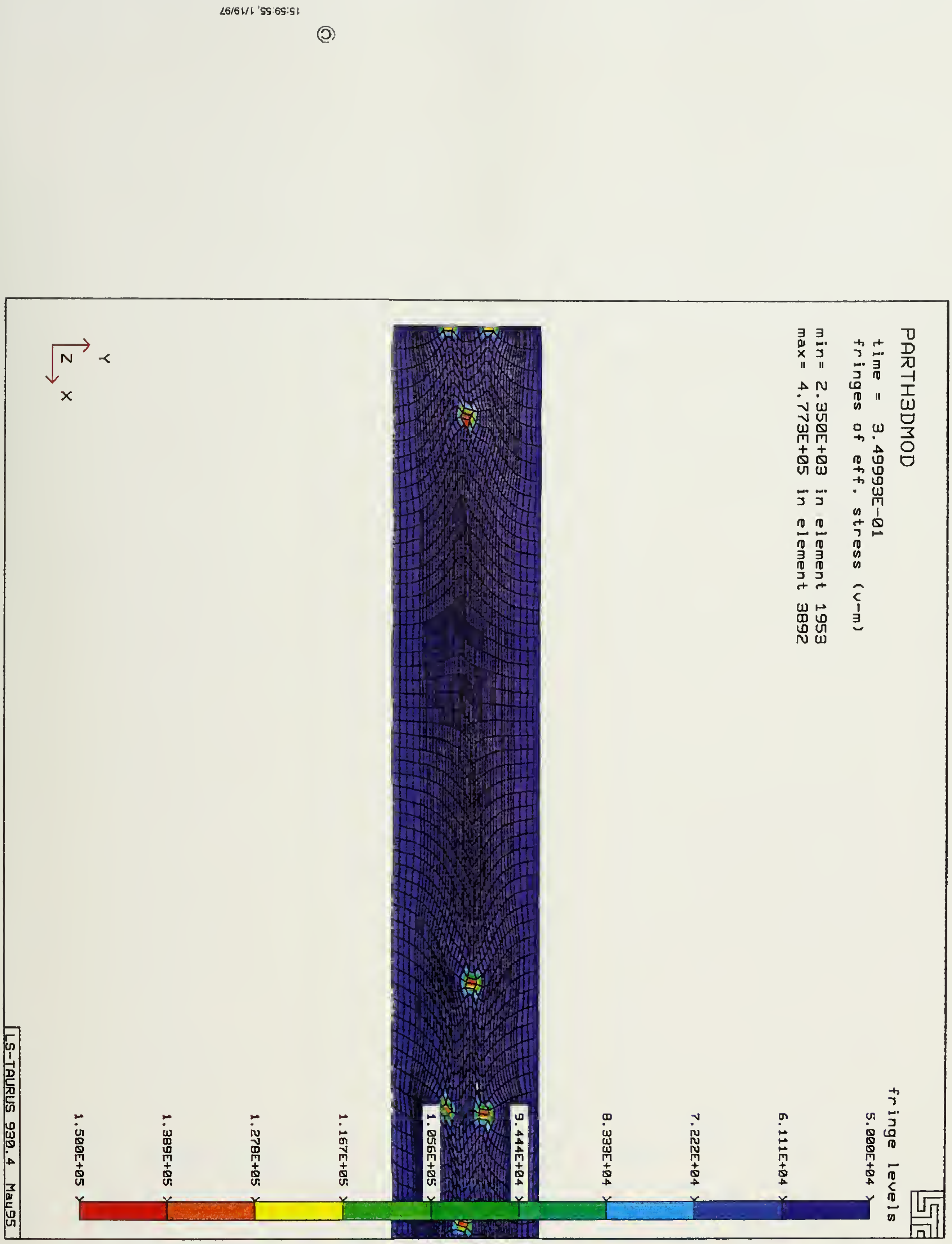

Figure C15: Fringe plot of Effective Von-Mises stress for the discrete hot worked intermediate strain rate model, with a local volume fraction of 2%, at a true strain of 1.20.

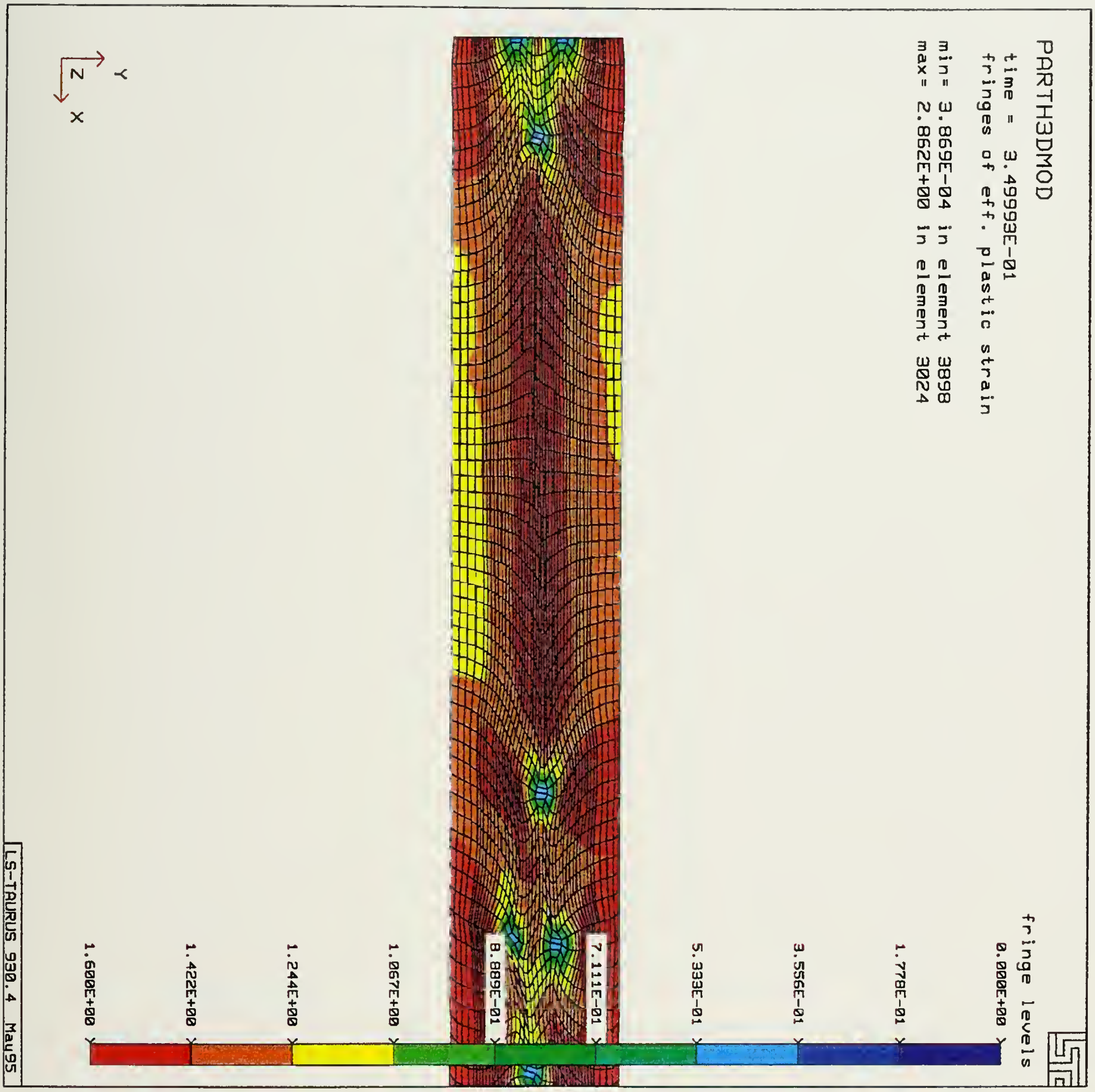

Figure C16: Fringe plot of Effective plastic strain for the discrete hot worked intermediate strain rate model, with a local volume fraction of 2%, at a true strain of 1.20.

16:2:13, 1/19/97

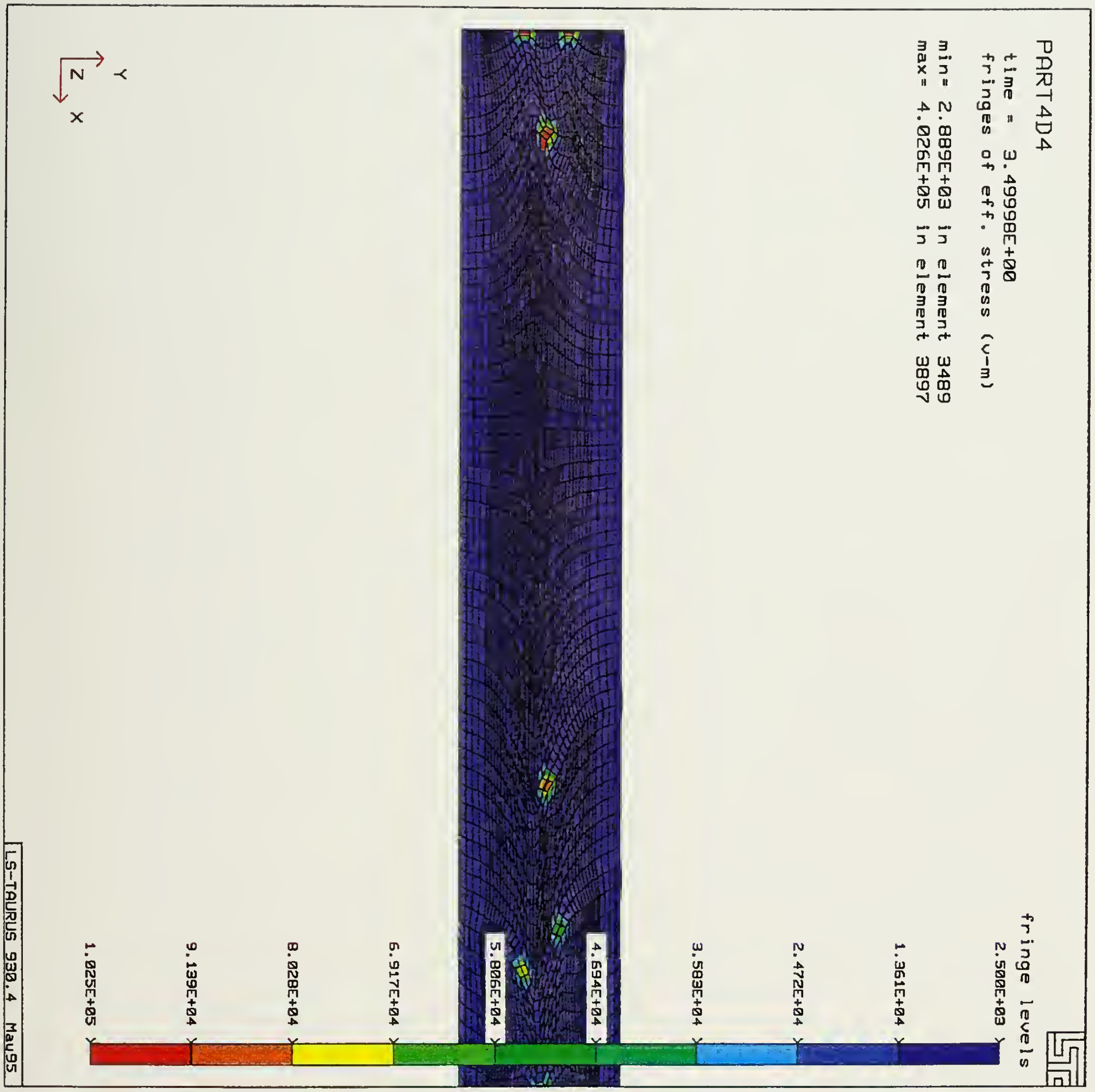

Figure C17: Fringe plot of Effective Von-Mises stress for the discrete hot worked low strain rate model, with a local volume fraction of 2%, at a true strain of 1.20.

Figure C18: Fringe plot of Effective plastic strain for the discrete hot worked low strain rate model, with a local volume fraction of 2%, at a true strain of 1.20.

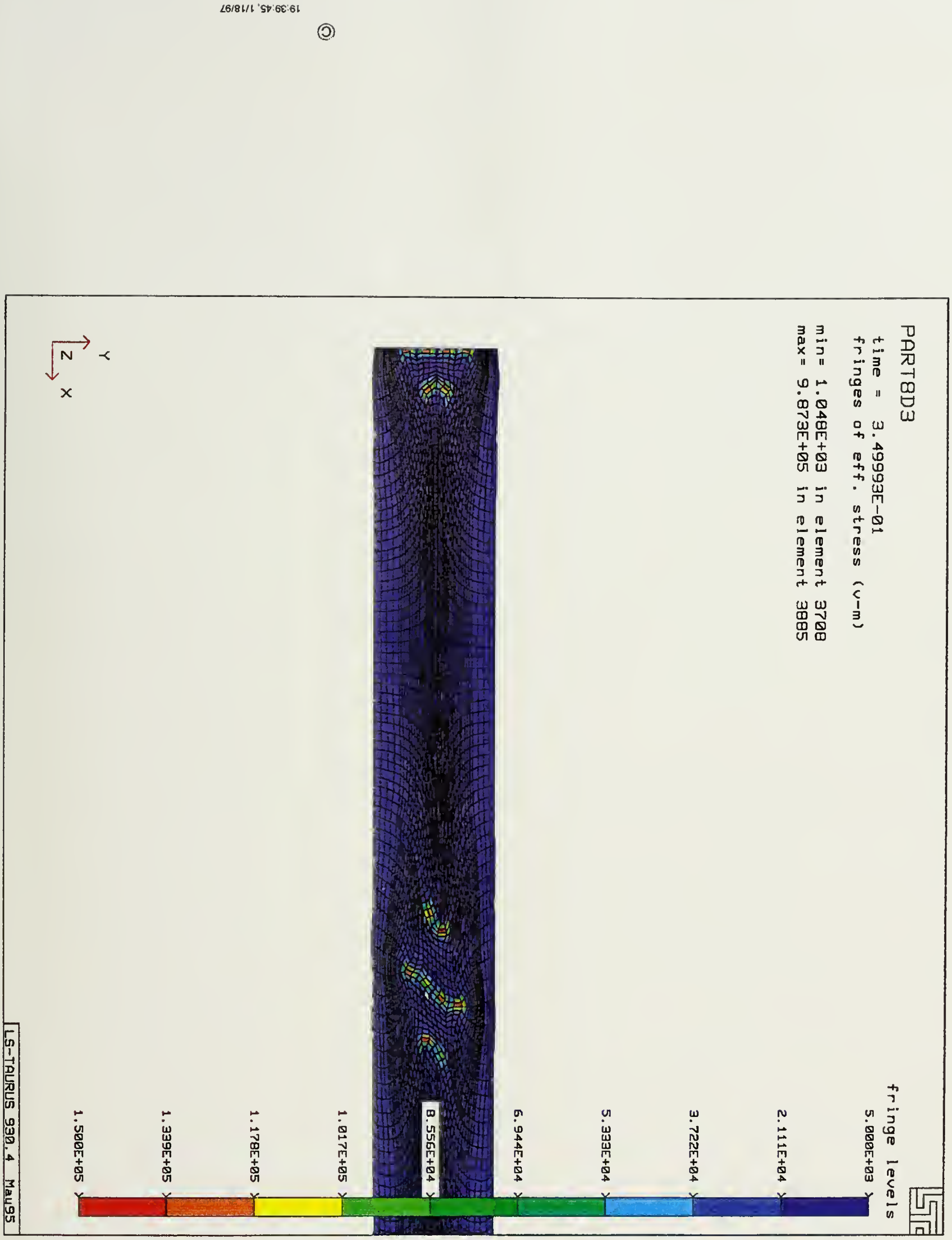

Figure C19: Fringe plot of Effective Von-Mises stress for the discrete hot worked intermediate strain rate model, with a local volume fraction of 4%, at a true strain of 1.20.

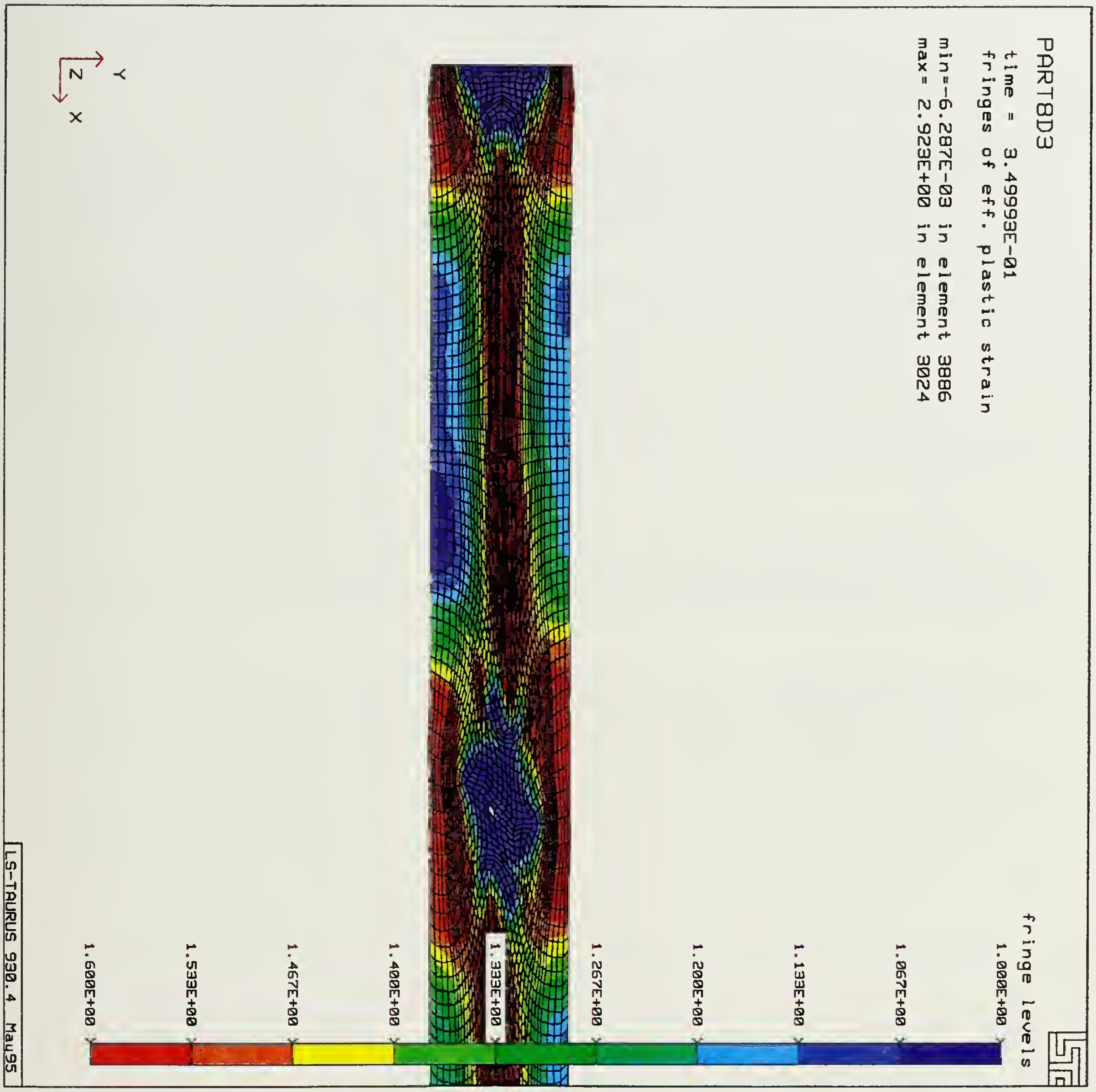

Figure C20: Fringe plot of Effective plastic strain for the discrete hot worked intermediate strain rate model, with a local volume fraction of 4%, at a true strain of 1.20.

LIST OF REFERENCES

Caddell, R. M., *Deformation and Fracture of solids*, Prentice-Hall inc. (1980)

Chawla, K. K., *Composite Materials, Science and Engineering*, Springer-Verlag. (1987)

Halliquist, J. O., *LS-DYNA3D Theoretical Manual,* Livermore Software Technology Corporation. (1991)

Hill, R., *The Material Theory of Plasticity*, Oxford University Press. (1956)

McNelly, T. R. and Ballou, M. A., *The Effect of Thermomechanical Processing on the Tensile Properties and Microstructures of a 6061 AL-AL_2O_3 Metal Matrix Composite*, Master's Thesis, Naval Postgraduate School, Monterey, California. (1995)

Parton, V. Z. and Kudryautsev, B. A., *Engineering Mechanics of Composite Structures*, CRC Press inc. (1993)

Schwartz, M. M., *Composite Materials Handbook*, 2nd Edition, McGraw-Hill inc. (1992)

Sherby, O. D. and Burke, P. M., *Mechanical Behavior of Crystalline Solids at Elevated Temperature*, Pergamon Press. (1968)

Sherby, O. D. and Wadsworth, J., *Development and Characterization of Fine-Grain Superplastic Material*, Papers presented at the 1982 ASM Materials Science Seminar. (1982)

Strong, A. B., *Fundamentals of Composite Manufacturing: Materials, Methods, and Applications*, Society of Manufacturing Engineers, Dearborn, Michigan. (1989)

Taya, M. and Arsenault, R. J., *Metal Matrix Composites, Thermomechanical Behavior*, Pergamon Press. (1989)

INITIAL DISTRIBUTION LIST

1. Defense Technical Information Center 2
   8725 John J. Kingman Road., Ste 0944
   Ft. Belvoir, Va 22060-6218

2. Dudley Knox Library 2
   Naval Postgraduate School
   411 Dyer Rd.
   Monterey, CA 93943-5101

3. Naval Engineering Curricular Office (Code 34) 1
   Naval Postgraduate School
   Monterey, Ca 93943-5002

4. Department Chairman, Code ME 1
   Department of Mechanical Engineering
   Naval Postgraduate School
   Monterey, Ca 93943-5002

5. Professor Young W. Kwon, Code ME/Kw 1
   Department of Mechanical Engineering
   Naval Postgraduate School
   Monterey, Ca 93943-5002

6. Dr. T. McNelley, Code ME/Mc 1
   Department of Mechanical Engineering
   Naval Postgraduate School
   Monterey, Ca 93943-5002

7. Professor Y. S. Shin, Code ME/Sg...1
   Department of Mechanical Engineering
   Naval Postgraduate School
   Monterey, Ca 93943-5002

8. Dr. Ernest S.C. Chin 1
   Weapons & Materials Res. Dir.
   U.S. Army Reasearch Laboratory
   Materials Division
   APG, MD 21005-5066

9. Lt Kendall Gennick 2
   11222 Rt. 166
   Marion, Il 62959

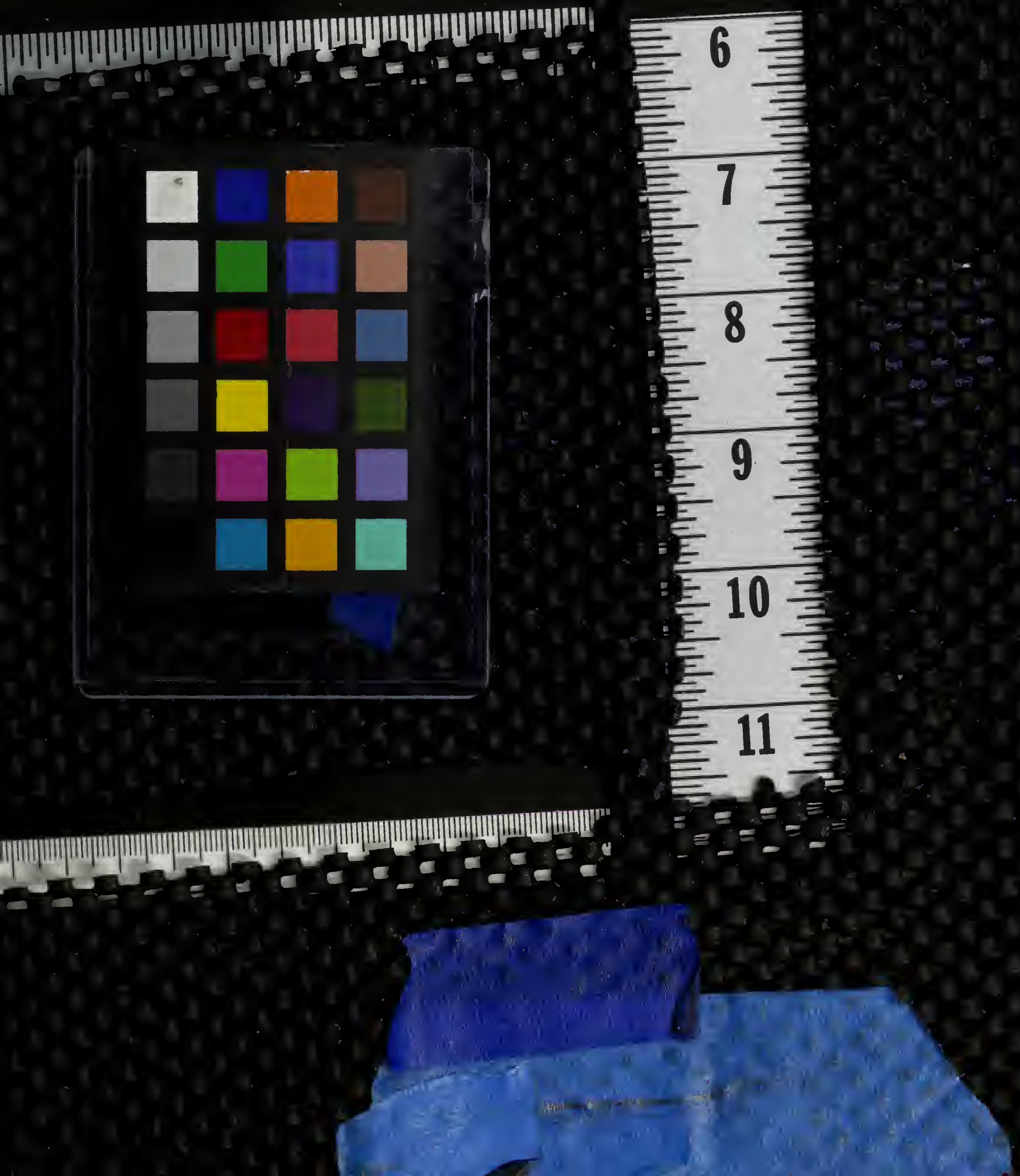
6
7
8
9
10
11